NTNU

Norwegian University of
Science and Technology

Application of Modular Multilevel Inverter for Interfacing Grid-Connected Photovoltaic Conversion Plants

Atousa Elahidoost

Master of Science in Electric Power Engineering
Submission date: June 2016
Supervisor: Lars Einar Norum, ELKRAFT
Co-supervisor: Hamed Nademi, ABB Oslo

Norwegian University of Science and Technology
Department of Electric Power Engineering

Abstract

The main focus of this master thesis is to investigate the application of modular multilevel converter (MMC) based grid-connected photovoltaic (PV) conversion systems, and a MATLAB/Simulink model of a PV system composed of two arrays connected to the grid via a five-level MMC is presented to study its operation under steady state and transients.

In response to global ever-increasing energy demand, and the pivotal significance of 100% clean and sustainable energy future to alleviate the adverse impact of fossil fuels and nuclear energy on global warming; tendency towards renewable sources of energy especially solar photovoltaic systems has incredibly grown in recent years. MMCs, as the PVs' inverters and controllers, among their other competitors show superior characteristics and immense potential. The most significant one as the name implies is its modularity that giving rise to fault-tolerant and fail-safe functionality as well as improved waveform quality and reduced harmonic pollution. Besides, MMCs are capable of transformer-less operation; in other words, small passive filters can be the only elements linking these converters to the grid.

In this study, a model for MMC-based grid-connected PV applications using MATLAB/Simulink software is developed. First, a piecewise linear model of a solar cell for simulating grid-connected PV systems is utilized to evaluate dynamic and transient response. Then, due to intermittent nature of the solar cells under various irradiances and temperatures, two different maximum power point tracking (MPPT) methods are implemented and compared under steady state and transients. The first one is the simple, flexible and robust method of perturb and observe (P&O) where practical techniques for choosing the perturbation frequency and step size based on the selection of the MPPT transient time is introduced. The second strategy is ripple correlation control (RCC) which reduces the steady state error and improves the convergence time. Next, to balance submodule (SM) capacitor voltages and reduce voltage ripples of the MMC, a phase disposition pulse width modulation (PDPWM) technique based on selective virtual loop mapping (SVLM) is simulated that is much faster than the conventional sorting algorithm since it only demands for min and max SM capacitor voltages. Finally, a conventional control method based on modulus optimum technique for tuning of inner current control loop, and symmetrical optimum technique for tuning of outer dc-voltage control loop is presented. Besides, the non-linear method of internal model-based control (IMBC) for controlling the current is presented. In this regard, system dynamic performance under

variations imposed by MPPT algorithms is improved, and the quality of the injected three phase current to the grid is enhanced.

Acknowledgement

I would like to express my sincere gratitude to my master thesis supervisor Prof. Lars Norum of the department of Electric Power Engineering at NTNU for providing me the opportunity to be involved in such an interesting subject, and also for his support throughout the project.

I also wish to thank Dr. Hamed Nademi (my master thesis co-supervisor from ABB) and Anirudh Bundar Acharya (PhD candidate at NTNU) for their encouragement and invaluable advice and guidance.

Finally, I want to thank my beloved husband, Ali, for his endless love, patience and support.

Atousa Elahidoost

10th June 2016

Table of Contents

List of Figures

List of Tables

Abbreviations

DER	Distributed Energy Resources
FACTS	Flexible AC Transmission Systems
FPGA	Field Programmable Gate Arrays
HVDC	High Voltage Direct Current
IMBC	Internal Model-Based Control
MMC	Modular Multilevel Converters
MPC	Model-based Predictive Control
MPPT	Maximum Power Point Tracking
P&O	Perturb and Observe
PDPWM	Phase Disposition Pulse Width Modulation
PSPWM	Phase-Shifted Pulse Width Modulation
PV	PhotoVoltaic
PWL	PieceWise Linear
RCC	Ripple Correlation Control
RSM	Real Sub-Module
SHE	Selective Harmonic Elimination
SM	Sub-Module
STC	Standard Test Conditions
SVLM	Selective Virtual Loop Mapping
THD	Total Harmonic Distortion
VSC	Voltage Source Converter
VSM	Virtual Sub-Module

Chapter 1

1 Introduction

1.1 Background

The global trend towards the improvement and implementation of the distributed energy resources (DER) especially renewables in response to realization of super smart grid policy is considerably growing in recent years. According to REN21, the estimated renewable energy share of the global electricity production by the end of 2013 was approximately 22.1% with hydropower, wind, bio-power, and solar having the highest contribution [1]. Today, the motivation for integration of renewables to global energy network is not only to meet the endlessly increasing energy demand but also to improve the energy availability, reliability, security, and quality, and to compensate the adverse impact of fossil fuels and nuclear energy on global warming [2].

Among various renewables, photovoltaic (PV) systems are one of the most promising ones. The global capacity of the PV systems shows significant increase from 3.7 GW in 2004 to 139 GW in 2013, by having 32% growth just in the year 2013 [1]. Germany, China, Italy, Japan, and United States are the leading countries in solar PV installed capacity [1]; however, there are far more geographical areas in the world (i.e. Africa) that have the required potential to develop and grow PV systems [2].

Since the PV systems are categorized as the intermittent sources of energy, and the yield of the PV systems is in the form of direct current and voltage, implementation of an interface between the grid and PV to regulate frequency and voltage based on the grid codes and standards is inevitable. As a result, state of the art modular multilevel converters (MMC) having unique characteristics and specifications can be considered as one of the most convincing alternatives to fulfill the mentioned objective [2].

1.2 Motivation and Objective of the Work

There is no better motivation in justification of grid-connected solar PV systems as one of the principal energy resources than the significance of having a 100% clean and sustainable energy future. Solar PV systems as modern sources of energy are in need of inverters for conversion and control to pave the way towards transition to global renewable energy network. Modular multilevel converters among other competitors show superior characteristics and immense

potential. The most significant one as the name implies is its modularity that giving rise to fault-tolerant and fail-safe functionality as well as improved waveform quality and reduced harmonic pollution. However, MMC-based grid-connected PV conversion systems have challenges and requirements to satisfactorily operate based on grid codes and to improve their efficiency and performance; it is this thesis's objective to study abovementioned system to propose an effective model that can develop steady state and dynamic performance of the system.

In addition, the following publication has been prepared as a part of this thesis work:

- Hamed Nademi, Atousa Elahidoost and Lars Norum, "Comparative Analysis of Different MPPT Schemes for Photovoltaic Integration of Modular Multilevel Converter," Accepted for presentation at 17th IEEE Workshop on Control and Modeling for Power Electronics (COMPEL) 2016, June 27-30, 2016, Trondheim, Norway.

1.3 Outline of the Work

This thesis is organized into five chapters, and the outline of the work is provided as follows:

- Chapter 2: This chapter is about photovoltaic (PV) system. An efficient PV array model together with a DC/DC converter are simulated. Furthermore, two effective maximum power point tracking algorithms (MPPT), perturb and observe (P&O) and ripple correlation control (RCC), are simulated and their performance are compared through several case studies.
- Chapter 3: This chapter is about modular multilevel converter (MMC). First, MMC topology, characteristics, and mathematical model are introduced. Then, a typical MMC with phase-shifted pulse width modulation (PSPWM) technique is simulated. Next, MMC-based grid-connected photovoltaic conversion plant operation in connection with P&O and RCC MPPT methods are investigated. Finally, MMC is equipped with an efficient sub-module (SM) capacitor voltage balancing strategy.
- Chapter 4: This chapter contains simulation results regarding conventional control method implementation including modulus optimum and symmetrical optimum as well as internal model-based control technique in MMC-based grid-connected photovoltaic power system.
- Chapter 5: "Conclusions," containing discussions and suggestions for future work.

Chapter 2

2 Photovoltaic System: Components and Maximum Power Point Tracking Algorithms

According to the energy policy proposed by European Commission on energy/climate change in 2008, 20% improvement in energy efficiency, 20% reduction in greenhouse gas emissions, and 20% increase in renewable energy consumption in Europe by 2020 is mandated. Furthermore, Europe is looking beyond 2020 and together with many other countries in the world is aiming for 100% renewable energy in future. Solar energy among all renewable resources plays a pivotal role, and is one of the most promising one due its abundance, availability, sustainability, and environmental friendly characteristics [3].

This chapter begins with PV system characteristics and mathematical model introduction. Then a typical PV array together with DC/DC boost converter is simulated. Next, two functional maximum power point tracking (MPPT) methods, perturb and observe (P&O) and ripple correlation control (RCC), are simulated and finally their performance are compared.

2.1 Photovoltaic Array Characteristics and Mathematical Model

Mathematical model of the PV array can be obtained by first modeling the PV cell. In fact, PV array is composed of PV cells that are connected in series and in parallel to meet the current and voltage requirement and to improve the produced power [2]. Figure 2.1 depicts the electrical equivalent circuit of a PV cell.

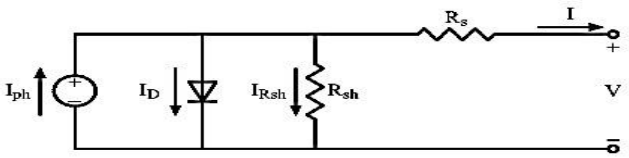

Figure 2.1: Electrical equivalent circuit of a PV cell [4].

Accordingly, the fundamental PV cell equations can be presented as [4]-[5]:

$$I = I_{ph} - I_0\left(e^{\left(\frac{q(V+IR_s)}{AKT}\right)} - 1\right) - \frac{V+IR_s}{R_{sh}} \tag{2.1}$$

$$I_{ph} = \left(I_{sc} + K_i\left(T - T_n\right)\right)\frac{G}{G_n} \tag{2.2}$$

$$I_0 = I_{0,n}\left(\frac{T_n}{T}\right)^3 e^{\left(\frac{qE_g}{AK}\right)\left(\frac{1}{T_n}-\frac{1}{T}\right)} \tag{2.3}$$

where equation parameters are given in Table 2.1. To solve the above equations the main five solar cell parameters that are I_{ph}, I_0, R_s, R_{sh}, and A, should be extracted from manufacturer's datasheet. These parameters are measured under standard test conditions (STC) that is equal to irradiance of 1000 W/m², solar spectrum of AM 1.5, and module temperature of 25 °C [2].

Table 2.1: Fundamental PV cell equations' parameters.

I and V	Cell output current and voltage
I_{ph}	Light generated current
I_0	Cell reverse saturation current
q	Electronic charge
R_s	Series resistance
A	Ideality factor between 1.0 to 1.5
K	Boltzmann's constant
T	Cell temperature in Celsius
R_{sh}	Shunt resistance
K_i	Short circuit current/temperature coefficient
T_n	Nominal temperature in Celsius
G	Solar radiation in W/m^2
G_n	Nominal solar radiation in W/m^2
$I_{0,n}$	Nominal saturation current
E_g	Energy gap

Therefore, considering equation (2.1) I-V curve and subsequently P-V curve of the PV cell are demonstrated in Figure 2.2.

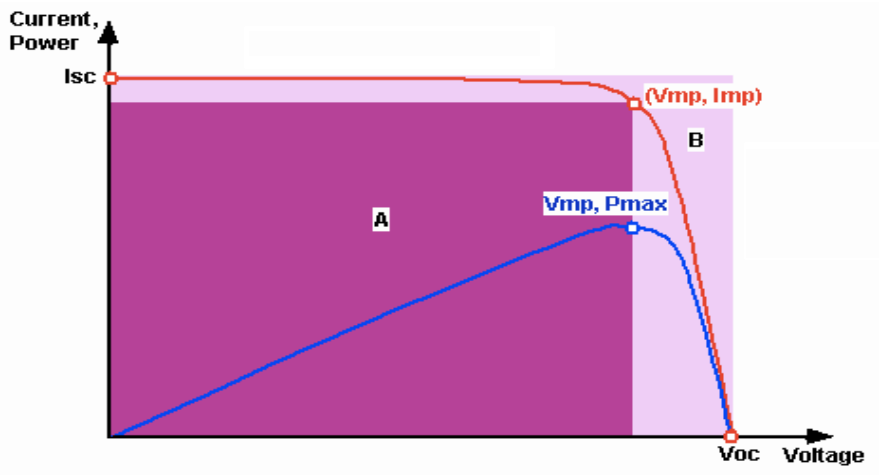

Figure 2.2: PV cell I-V (red curve) and P-V (blue curve) Characteristics [6].

However, PV cells are not always operating under standard test conditions. In fact, solar cells are exposed to irradiances and temperatures other than STC that highly affect PV cell performance. For instance, high irradiance increases PV cell short circuit current, whereas high temperature decreases solar cell open circuit voltage. Moreover, geographical location, installation configuration, shading and soiling, and weather condition have dramatic impact on photovoltaic efficiency. As a result, when investigating PV cell performance, these factors should be taken into account [2], [4], [6]-[7].

2.2 Photovoltaic Array Simulation

The first step in photovoltaic array simulation is to model the solar cell. The solar cell model chosen is based on [8], and parameters extracted from [9]-[10] are presented in Table 2.2.

Table 2.2: Canadian Solar CS6P-240P parameters at AM1.5, irradiance of 1000 W/m^2, and temperature of 25 °C.

Nominal Maximum Power (P_{max})	240 W
Optimum Operating Voltage (V_{mp})	29.9 V
Optimum Operating Current (I_{mp})	8.03 A
Open Circuit Voltage (V_{OC})	37 V
Short Circuit Current (I_{SC})	8.59 A
Module Efficiency	14.92 %

The proposed PV model that can be seen in Figure 2.3 is mainly designed to be applicable for simulating grid-connected PV systems comprising several inverters. Indeed, it is suitable for dynamic and transient studies in power systems. Not only it is flexible and robust but also it can simply be implemented in software programs like MATLAB/Simulink [8].

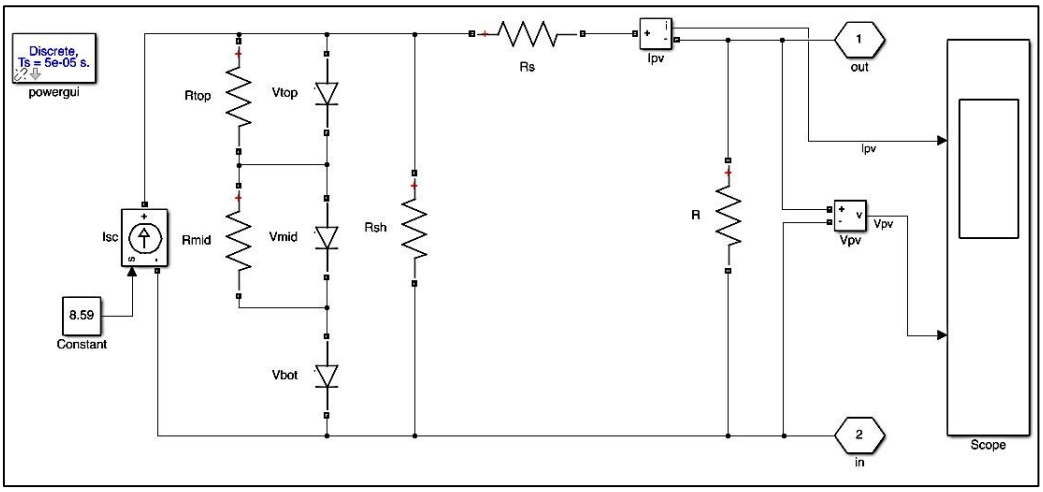

Figure 2.3: Solar cell model circuit diagram.

This model is in fact a piecewise linear (PWL) model that initiates from the single-diode model of the solar cell. However, instead of one diode three series diodes and two bypass resistors are used to simulate the PV characteristics within four linear segments. The solar cell CS6P-240P parameters according to [10] are given in Table 2.3.

Table 2.3: Solar cell model parameters.

V_{TOP}	V_{MID}	V_{BOT}	R_{TOP}	R_{MID}	R_{SH}	R_S
1.49 V	10.81 V	24.7 V	0.41 Ω	21.1 Ω	616.67 Ω	0.72 Ω

The IV and PV curves of the suggested model simulated in MATLAB/Simulink are shown in Figure 2.4 and Figure 2.5. Results indicate adequate compatibility with electrical data given in the datasheet, and assure the validity of the model.

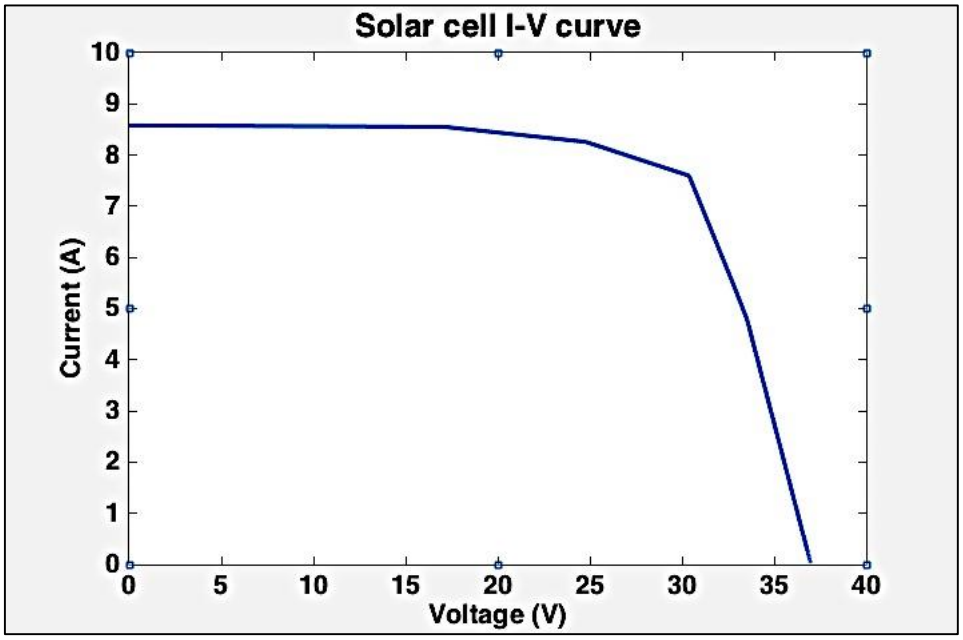

Figure 2.4: Solar cell IV curve.

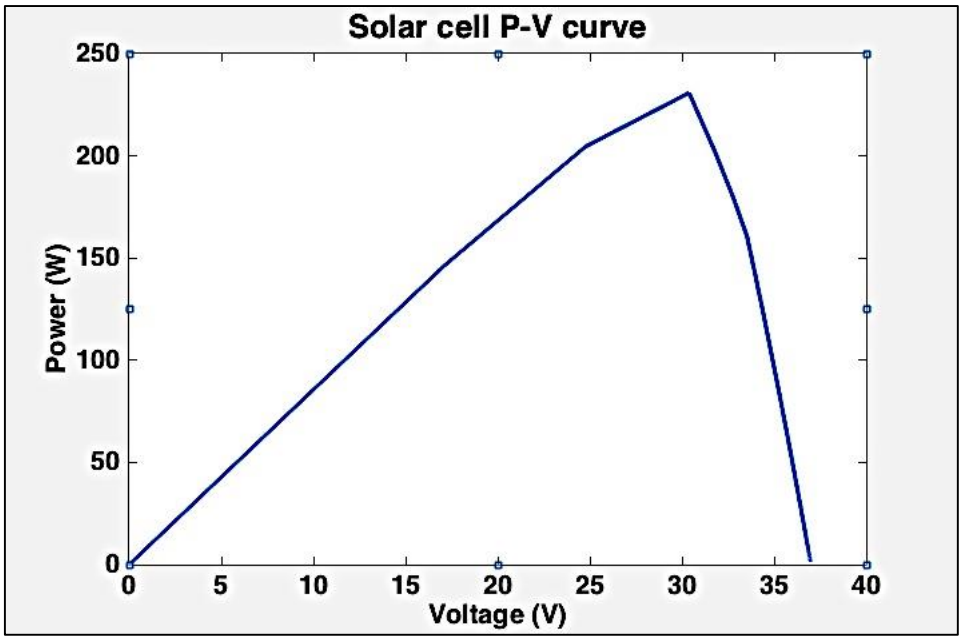

Figure 2.5: Solar cell PV curve.

Photovoltaic arrays have intermittent nature, and their characteristics are dependent on solar irradiance and temperature. To model the solar irradiance effect it is possible to vary the short circuit current in the proposed model since the short circuit current variation due to irradiance fluctuation is high in comparison with the open circuit voltage change. However, temperature influence modeling is usually not of interest. First, temperature fluctuation is not an instant phenomenon, and intrinsically occurs in long time interval. Second, short circuit current and open circuit voltage variations owing to temperature change are trivial that can be neglected. Anyway, to model the temperature fluctuation it is possible to inversely add an ideal DC voltage source to the diode branch as depicted in [8].

2.3 Boost (Step-up) Converter Simulation

To be able to implement MPPT, PV array is connected to a boost converter as can be seen in Figure 2.6. As a result, it is possible to track maximum power point by properly adjusting the duty ratio of the converter. The boost converter model parameters are given in Table 2.4. A stray large capacitance (as Ci in Figure 2.6) needs to be modeled at the output of the PV panel, especially if there is going to be a long distance between the array and the converter. This capacitance adversely affects the MPPT convergence process by phase shifting the current and subsequently power ripple [11].

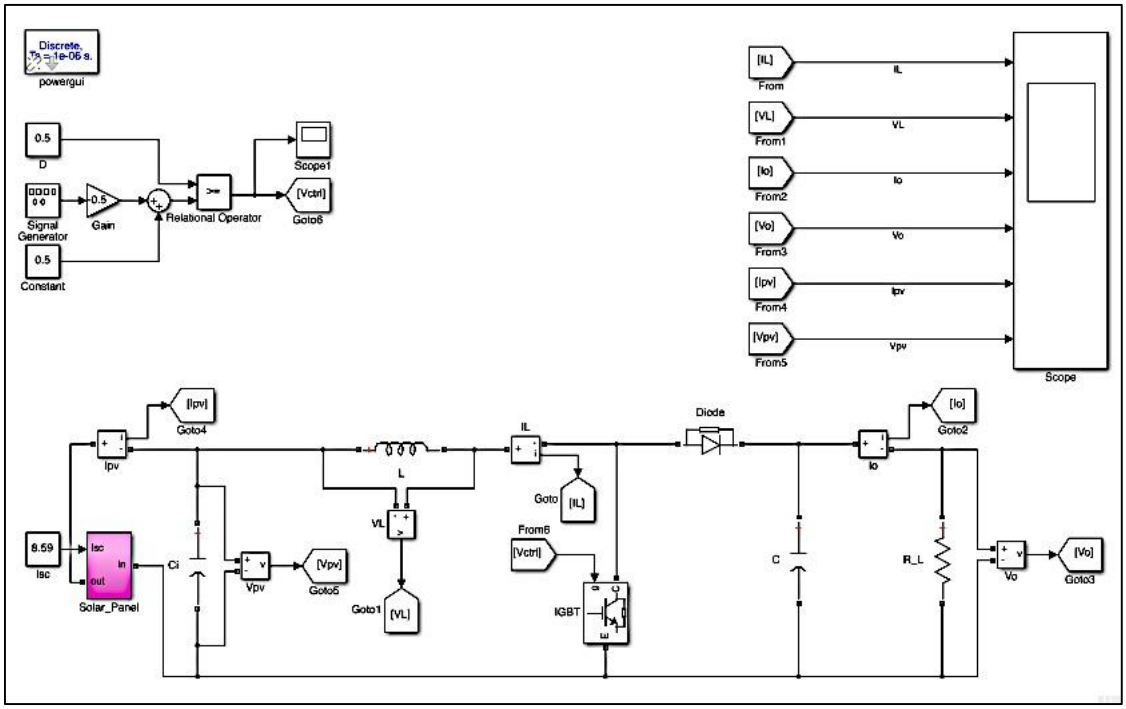

Figure 2.6: PV panel and boost converter model.

Table 2.4: Boost converter model parameters.

C_i	L	C	R_L
2 mF	2000 uH	200 uF	100 Ω

Simulation results regarding inductor, load and PV currents and voltages are presented from Figure 2.7 to Figure 2.12; so that, boost converter operation in connection with PV panel can be validated. The PV panel is composed of 9 series PV cells, duty ratio is set to 0.5, and switching frequency is 10 KHz. It is clear that the obtained figures assure the proper operation of the system.

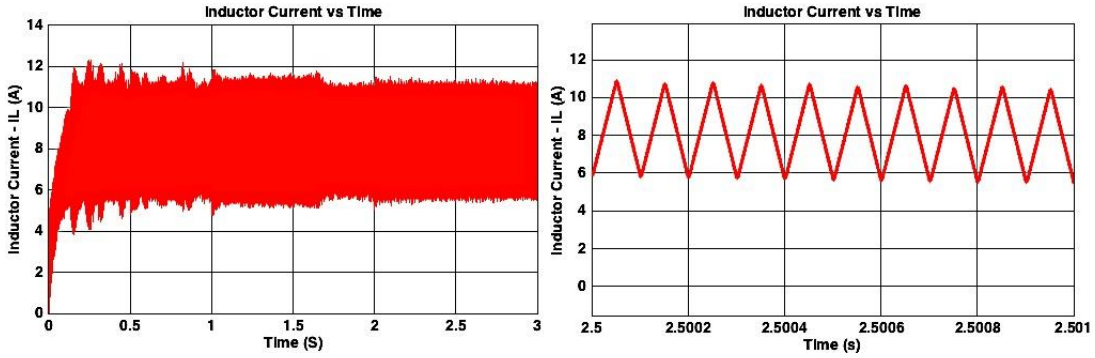

Figure 2.7: Boost converter inductor current vs time.

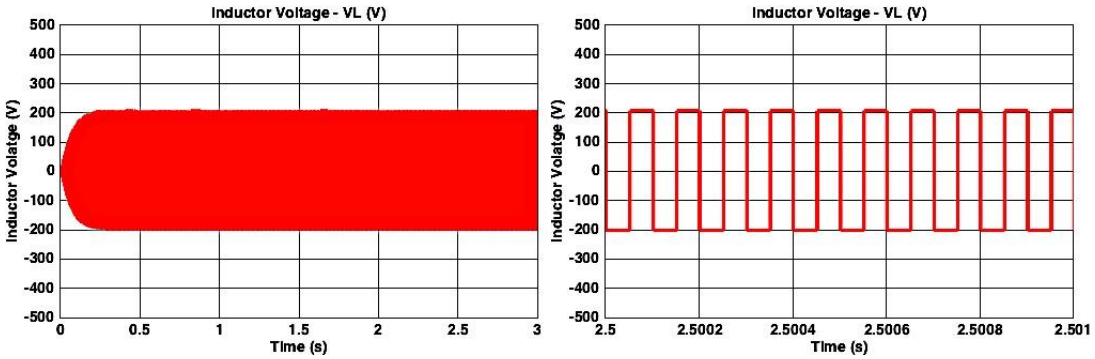

Figure 2.8: Boost converter inductor voltage vs time.

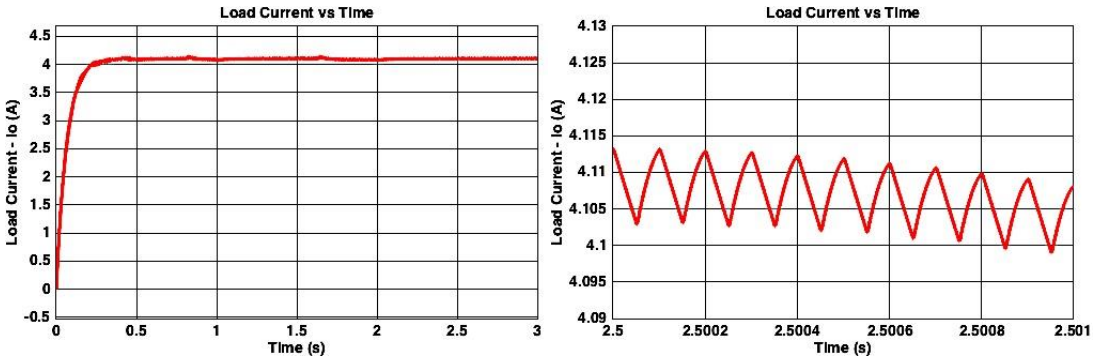

Figure 2.9: Boost converter load current vs time.

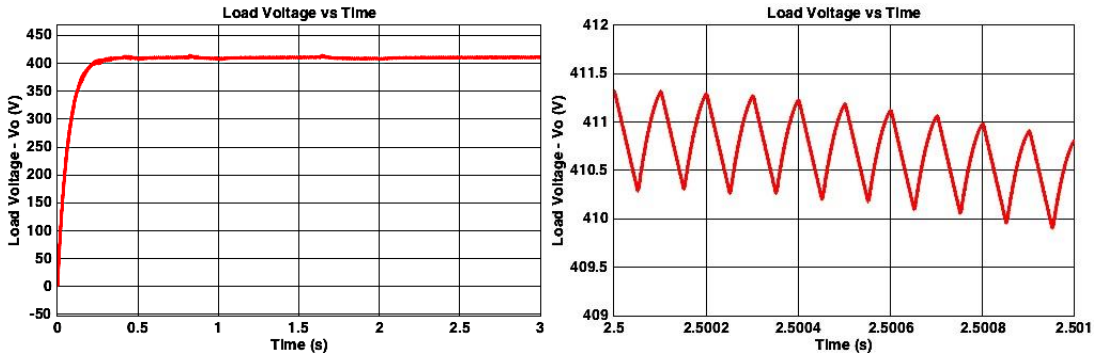

Figure 2.10: Boost converter load voltage vs time.

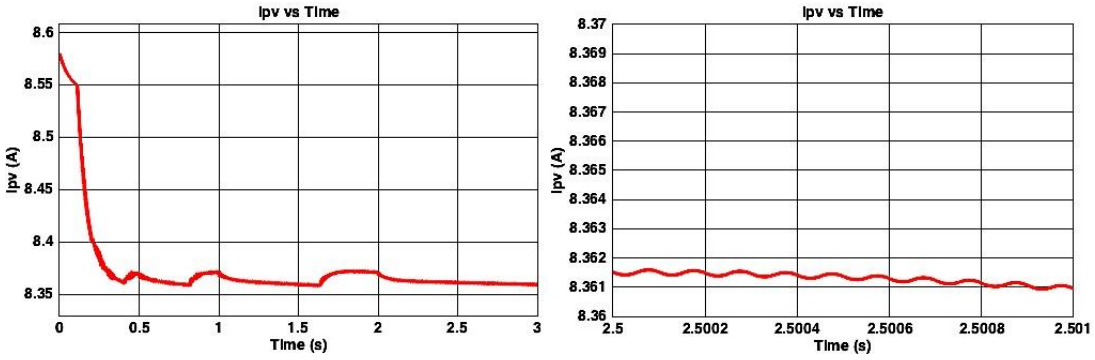

Figure 2.11: Boost converter PV current vs time.

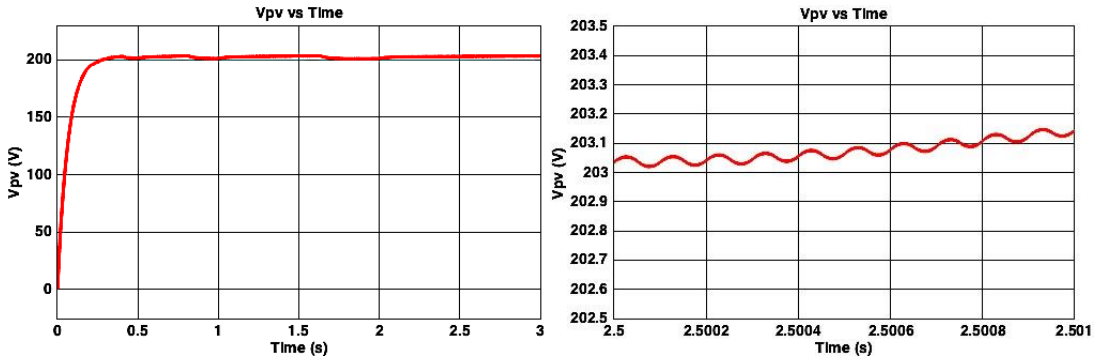

Figure 2.12: Boost converter PV voltage vs time.

2.4 Maximum Power Point Tracking

Maximum power point tracking implementation is essential for grid-connected PV systems to extract maximum power at any moment of time. This is as a result of solar cell specification variation under different conditions. Factors such as solar irradiance, temperature, geographical location, installation configuration, shading and soiling, and weather condition are responsible for short circuit current and open circuit voltage fluctuations leading to efficiency and power alteration [2].

2.4.1 Perturb and Observe MPPT

Various MPPT strategies have already been integrated into grid-connected photovoltaic conversion plants. One of the most common ones is perturb and observe technique that has widely been used in modular multilevel converter based grid-connected photovoltaic systems. Although P&O method is simple, flexible and robust, it requires an external electronic system to induce perturbation. Moreover, there is always trade-off between steady state error and convergence speed. The operating principle is based on the fact that the relative derivative of PV power with respect to the PV voltage is equal to zero at MPP, has positive value at PV voltages less than MPP voltage, and negative value at PV voltages more than MPP voltage (see Figure 2.13). The abovementioned principle is summarized in following equations [2], [12]:

$$\frac{\partial P_{PV}}{\partial V_{PV}} = 0 \Rightarrow V_{PV} = V_{MPP} \tag{2.4}$$

$$\frac{\partial P_{PV}}{\partial V_{PV}} \rangle 0 \Rightarrow V_{PV} \langle V_{MPP} \tag{2.5}$$

$$\frac{\partial P_{PV}}{\partial V_{PV}} \langle 0 \Rightarrow V_{PV} \rangle V_{MPP} \tag{2.6}$$

Where P_{PV} and V_{PV} are PV power and voltage respectively, and V_{MPP} is the maximum power point voltage.

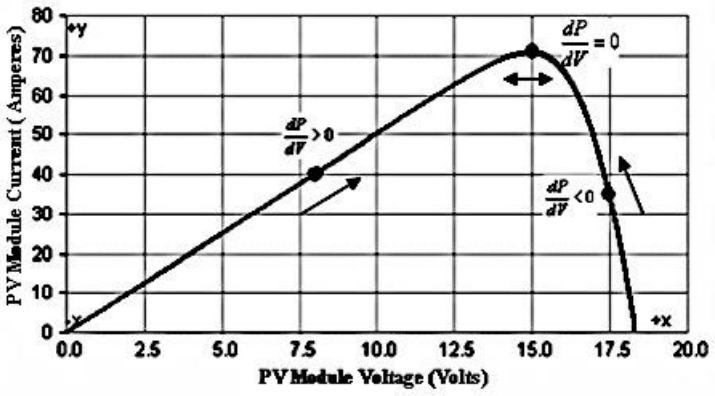

Figure 2.13: P&O MPPT method philosophy [12].

In this strategy, PV operating point; in other words, PV control parameter (duty ratio or reference voltage) needs to be perturbed at a fixed perturbation frequency at a specific step size. There is an inherent trade-off in choosing the step size; that is, the larger the step size the shorter the convergence time and the higher the steady state error. There is an appropriate method to efficiently select the two P&O MPPT parameters: perturbation frequency and step size, instead of choosing them by trial and error [2], [13].

The criterion in selecting perturbation frequency is based on the fact that perturbation period needs to be larger than the settling time; therefore, system has adequate time to settle to steady state condition before the next perturbation. That is, perturbation frequency should be smaller than the reciprocal of the settling time. On the other hand, to estimate the optimized step size, the acceptable control parameter tolerance with respect to the initial optimum value ($\Delta D \; or \; \Delta V$) is divided by the algorithm transient time (expected MPPT convergence time) to obtain the amount of variation per second, then the result is divided by perturbation frequency to get the step size [2], [13].

Considering Figure 2.14, it is possible to implement P&O MPPT algorithm by defining either the duty ratio or the reference voltage as the perturbation parameter. According to detailed theoretical and experimental assessment of these two methods in [13], findings can be summarized as follows: Direct duty ratio perturbation technique offers higher system stability characteristics at slower transient responses, and perturbation frequency can be increased up to PWM rate without losing stability. Besides, direct duty ratio perturbation provides better energy utilization at both slow and rapid changing transients. On the contrary, reference voltage

perturbation shows better system performance by having faster dynamic response to irradiance and temperature transients.

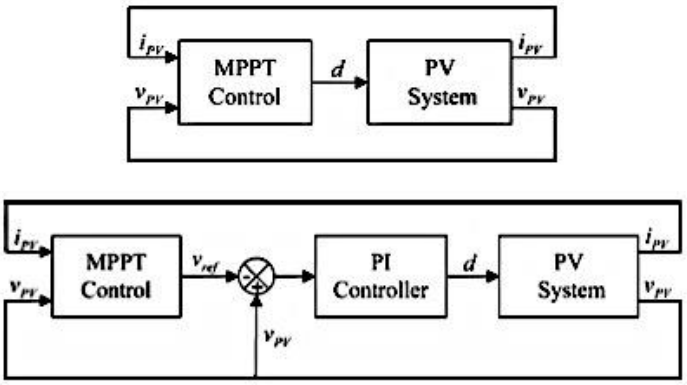

Figure 2.14: MPPT implemented by two different P&O techniques (up) direct duty ratio perturbation block diagram, (down) reference voltage perturbation block diagram [13].

2.4.2 Perturb and Observe MPPT Simulation

P&O MPPT algorithm considered for simulation is based on direct duty ratio perturbation method. Table 2.5 shows boost converter model parameters. P&O MPPT algorithm flowchart and MATLAB/Simulink implementation are presented in Figure 2.15 and Figure 2.16 respectively. Since the settling time of the system is about 200 ms, the perturbation frequency is chosen to be 4 HZ ($f_{perturbation} < 1/T_{settling}$). Considering $\Delta D = 0.4$ *(*$\Delta D = D_{max} - D_{initial}$ or $\Delta D = D_{initial} - D_{min}$, while $D_{min} = 0.1$, $D_{initial} = 0.5$ and $D_{max} = 0.9$) and $t_{tr} = 2$ s (expected MPPT convergence time); accordingly, step size will be equal to 0.05 ($\Delta d_{step\ size} = \Delta D / t_{tr} / f_{perturbation}$).

Table 2.5: Boost converter model parameters in connection with P&O MPPT method implementation.

C_i	L	C	R_L
200 uF	750 uH	200 uF	100 Ω

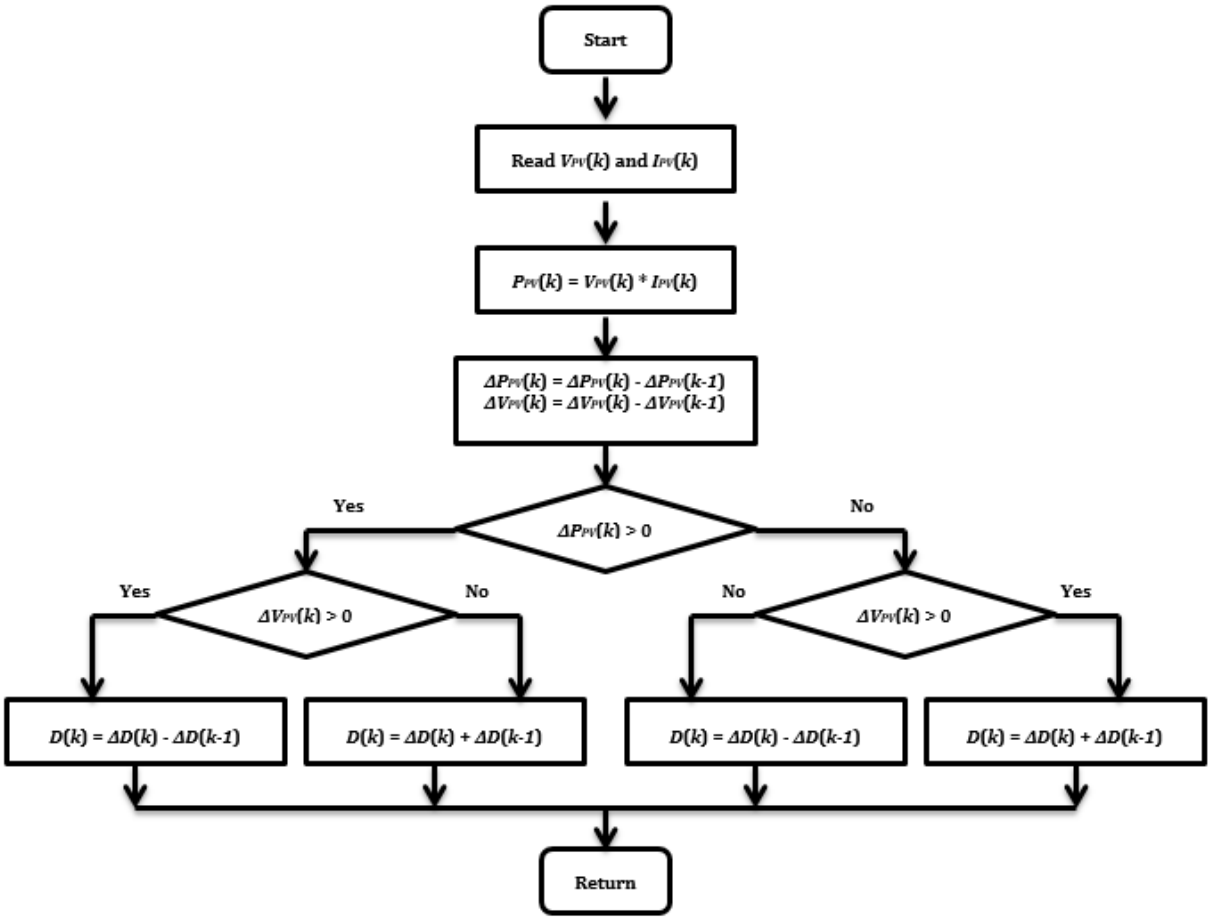

Figure 2.15: P&O MPPT algorithm flowchart.

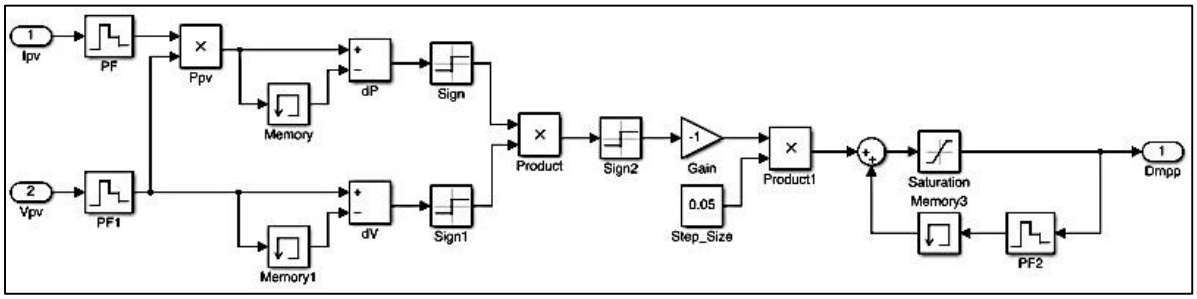

Figure 2.16: P&O MPPT algorithm implementation in MATLAB/Simulink.

To make sure MPPT algorithm can converge to the right duty cycle leading to MPPT, maximum power point duty cycle can theoretically be calculated as [7]:

$$V_o = \frac{1}{1 - D_{MPP}} . V_{PV-MPP} \tag{2.7}$$

$$I_{PV-MPP} = \frac{1}{1 - D_{MPP}} . I_o \tag{2.8}$$

By combining (2.7) and (2.8), and knowing that $V_o = R_L * I_o$:

$$D_{MPP} = 1 - \sqrt{\frac{V_{PV-MPP}}{R_L . I_{PV-MPP}}} = 1 - \sqrt{\frac{29.9V * 9}{100\Omega * 8.03A}} = 0.42 \tag{2.9}$$

Furthermore, the expected maximum power point parameters at different test conditions are as given in Table 2.6 [10]:

Table 2.6: Expected maximum power point parameters at different test conditions.

***S* (W/m^2)**	***V_{MPP}* (V)**	***I_{MPP}* (A)**	***P_{MPP}* (kW)**
1000	269.1	8.03	2.161
800	283.5	6.3	1.786
600	293	4.61	1.351

2.4.2.1 P&O MPPT Algorithm Case Study 1

In this case study, PV system is operating under STC conditions, and simulation results are demonstrated in Figure 2.17. P&O MPPT algorithm has converged to MPP after 0.5 s, and the obtained D_{MPP} is equal to 0.4. Comparing this value with the theoretical calculated value (D_{MPP} = 0.42) there is 4.76% error. However, it is apparent that in P&O MPPT algorithm the error level can be in the worst-case scenario equal to step size that is 5% in this case. It can also be seen that PV current ripple is higher than the output current ripple, while PV voltage ripple is lower than the output voltage ripple. Summary of the simulation results is available in Table 2.7.

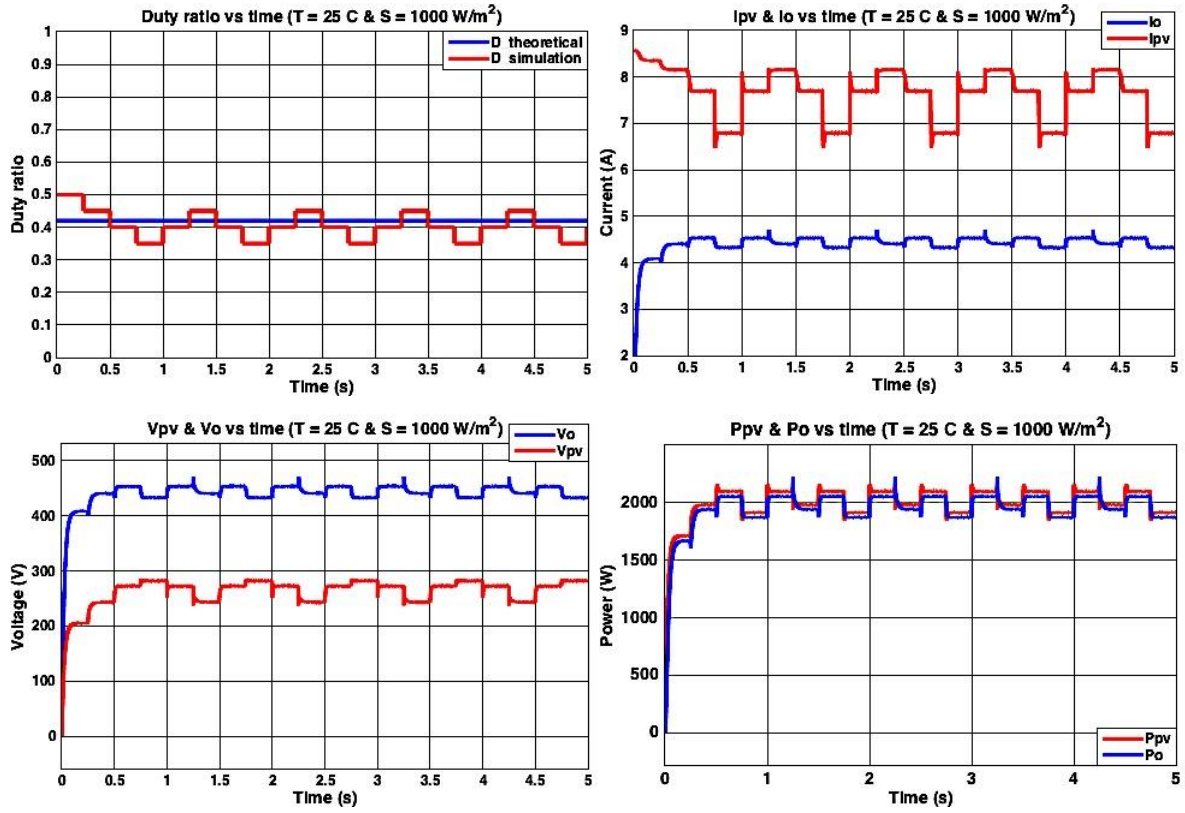

Figure 2.17: P&O MPPT algorithm case study 1 simulation results.

2.4.2.2 P&O MPPT Algorithm Case Study 2

To investigate how the system responses to irradiance variation, temperature is kept constant at 25 °C and irradiance is reducing in 200 W/m^2 steps every 3 s in this case study. Simulation results are presented in Figure 2.18. P&O MPPT algorithm has converged to the MPP after 0.25 s in the first step change, and within 0.5 s in the second one. In fact, it seems that P&O MPPT method response time strongly depends on two factors. First, its location in three-level operation at the moment variation occurs; second, amount of variation. For instance, in the first three seconds duty ratio value fluctuates in three levels of 0.45, 0.4 and 0.35. At the moment step change occurs (t = 3 s), duty ratio is at 0.4, and after one perturbation it converges to 0.35 that is the correct value at irradiance of 800 W/m^2. Moreover, at t = 3 s duty ratio needs to change from 0.42 to 0.33 (0.42 - 0.33 = 0.09), and at t = 6 s it should fluctuate from 0.33 to 0.2 (0.33 – 0.2 = 0.11). It is clear that at t = 6 s longer variation is required. Convergence speed can be improved by increasing the step size; however, it will adversely affect the steady sate error. Summary of the simulation results is available in Table 2.7.

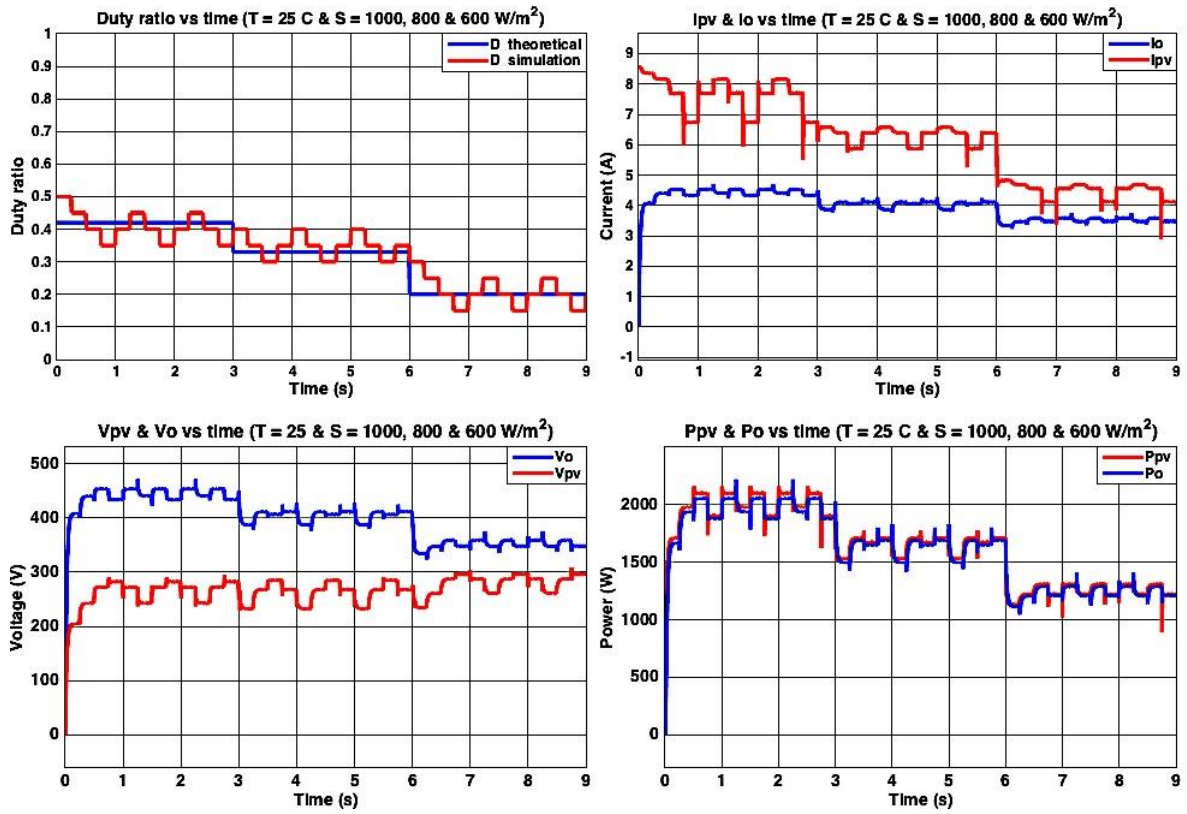

Figure 2.18: P&O MPPT algorithm case study 2 simulation results.

2.4.2.3 P&O MPPT Algorithm Case Study 3

The aim of this case study is to examine system behavior under large transients. As a result, solar irradiance is varying from 1000 W/m^2 to 600 W/m^2 at t = 3 s, and back to 1000 W/m^2 at t = 6 s while the temperature is kept constant. Simulation results are given in Figure 2.19. It can be seen that P&O MPPT algorithm is able to converge to MPP within a reasonable convergence speed. The convergence time is about 1 s that is less than the defined transient time (t_{tr} = 2 s) with 5% steady-state error at worst case scenario. Summary of the simulation results is available in Table 2.7.

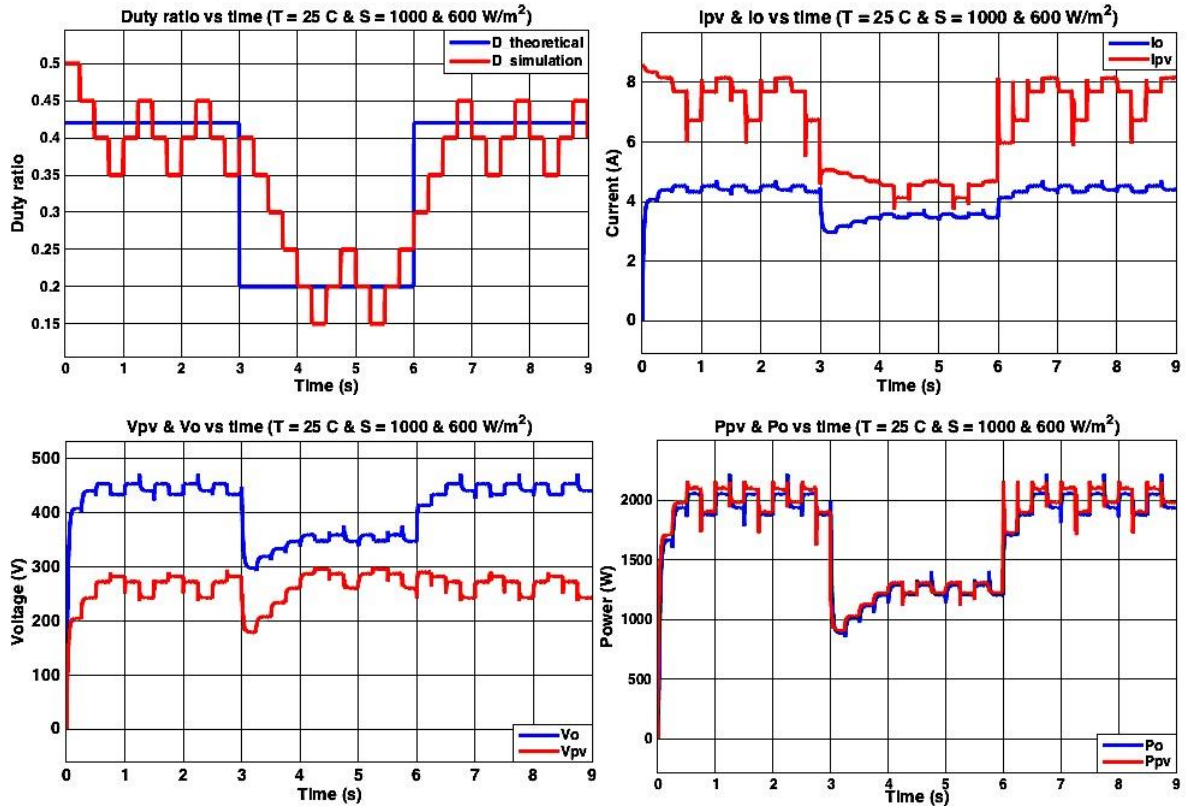

Figure 2.19: P&O MPPT algorithm case study 3 simulation results.

Table 2.7: Summary of P&O MPPT algorithm simulation results.

S (W/m^2)	I_{SC} (A)	D_{MPP}	V_{MPP} (V)	I_{MPP} (A)	P_{MPP} (W)	V_o (V)	I_o (A)	P_0 (W)
1000	8.59	0.4	270	7.7	2079	453	4.5	2038
800	6.9	0.35	267	6.4	1708	410	4.1	1681
600	5.1	0.2	295	4.2	1239	350	3.5	1225

2.4.3 Ripple Correlation Control MPPT

Ripple correlation control is an MPPT algorithm that can compensate P&O MPPT method deficiencies. It reduces steady state error and accelerates convergence time. Above all, there is no need for an external electronic system to induce perturbation. In fact, RCC exploits the converter generated current and voltage ripple as perturbation source to apply MPPT algorithm. RCC MPPT operating principle is as follows [2], [10]-[11], [14]:

$$\frac{\partial p_{PV}}{\partial t}.\frac{\partial v_{PV}}{\partial t}=0\Rightarrow V_{PV}=V_{MPP} \tag{2.10}$$

$$\frac{\partial p_{PV}}{\partial t}.\frac{\partial v_{PV}}{\partial t}\rangle 0\Rightarrow V_{PV}\langle V_{MPP} \tag{2.11}$$

$$\frac{\partial p_{PV}}{\partial t}.\frac{\partial v_{PV}}{\partial t}\langle 0\Rightarrow V_{PV}\rangle V_{MPP} \tag{2.12}$$

Where P_{PV} and V_{PV} are PV power and voltage respectively, and V_{MPP} is the maximum power point voltage.

Equations are based on the fact that product of time derivative of power and voltage is negative at right side of MPP, positive at left side of MPP, and zero at MPP. Accordingly, it can be shown that:

$$\frac{dd}{dt}=K\frac{dp_{PV}}{dt}.\frac{dv_{PV}}{dt} \tag{2.13}$$

Or,

$$d(t)=K\int\frac{dp_{PV}}{dt}.\frac{dv_{PV}}{dt} \tag{2.14}$$

Where d is the converter duty ratio, and K is a constant gain.

Since P_{PV} cannot be directly measured:

$$d(t)=K\int\frac{dv_{PV}i_{PV}}{dt}.\frac{dv_{PV}}{dt}=K\int(i_{PV}\frac{dv_{PV}}{dt}+v_{PV}\frac{di_{PV}}{dt}).\frac{dv_{PV}}{dt} \tag{2.15}$$

Indeed, RCC control aim is to track $\frac{dd}{dt}=0$, where $d(t) = d_{MPP}$.

2.4.4 Ripple Correlation Control MPPT Simulation

To implement RCC MPPT algorithm in MATLAB/Simulink is simpler to transfer equation (2.15) from time domain into frequency domain [10]:

$$d(s) = K\frac{1}{s}\left(\left(i_{PV}sv_{PV} + v_{PV}si_{PV}\right).sv_{PV}\right) = K\frac{1}{s}\left(2s^2v_{PV}^2i_{PV}\right) \tag{2.16}$$

Instead of having two consecutive derivators that can lead to instability, it is possible to write:

$$d(s) = K\frac{1}{s}\left(\left(sv_{PV}i_{PV}\right).sv_{PV}\right) \tag{2.17}$$

However, after implementing equation (2.17) in MATLAB/Simulink, software program could not converge to the solution. To avoid this issue, PV current and voltage ripple values were per-unitized before entering the derivators, so that the magnitude of their product was significantly reduced and convergence could be obtained. The RCC MPPT algorithm implementation in MATLAB/Simulink is presented in Figure 2.20.

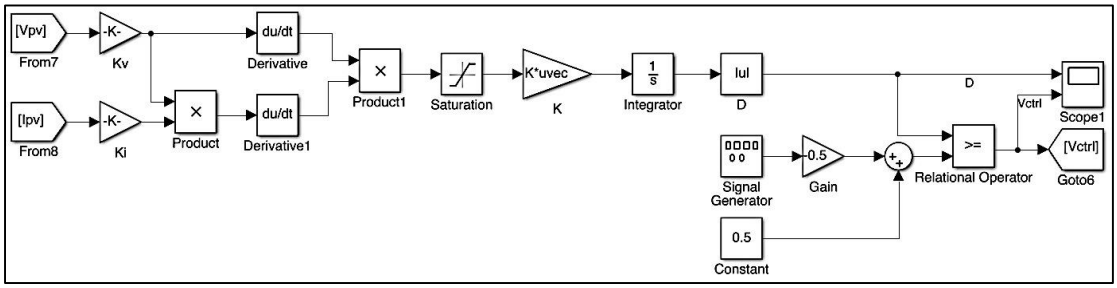

Figure 2.20: RCC MPPT algorithm implementation in MATLAB/Simulink.

2.4.4.2 RCC MPPT Algorithm Case Study 1

Simulation results for aforementioned system are demonstrated in Figure 2.21 under STC conditions. The RCC MPPT algorithm has converged to the solution in approximately 300 ms. This time is exactly equal to condition without RCC MPPT implementation, and can be interpreted as the time required for the system to be initiated. The resultant duty cycle is nearly equal to 0.41 that is very close to the theoretical value with 2.38 % error. The measured V_{MPP}, I_{MPP} and P_{MPP} are about 269 V, 8 A and 2152 W respectively with negligible error comparing to the expected values. Besides, input and output powers are almost equal, and output voltage and current contain about 3.24 % and 3.26 % ripples respectively. Summary of the simulation results is available in Table 2.8.

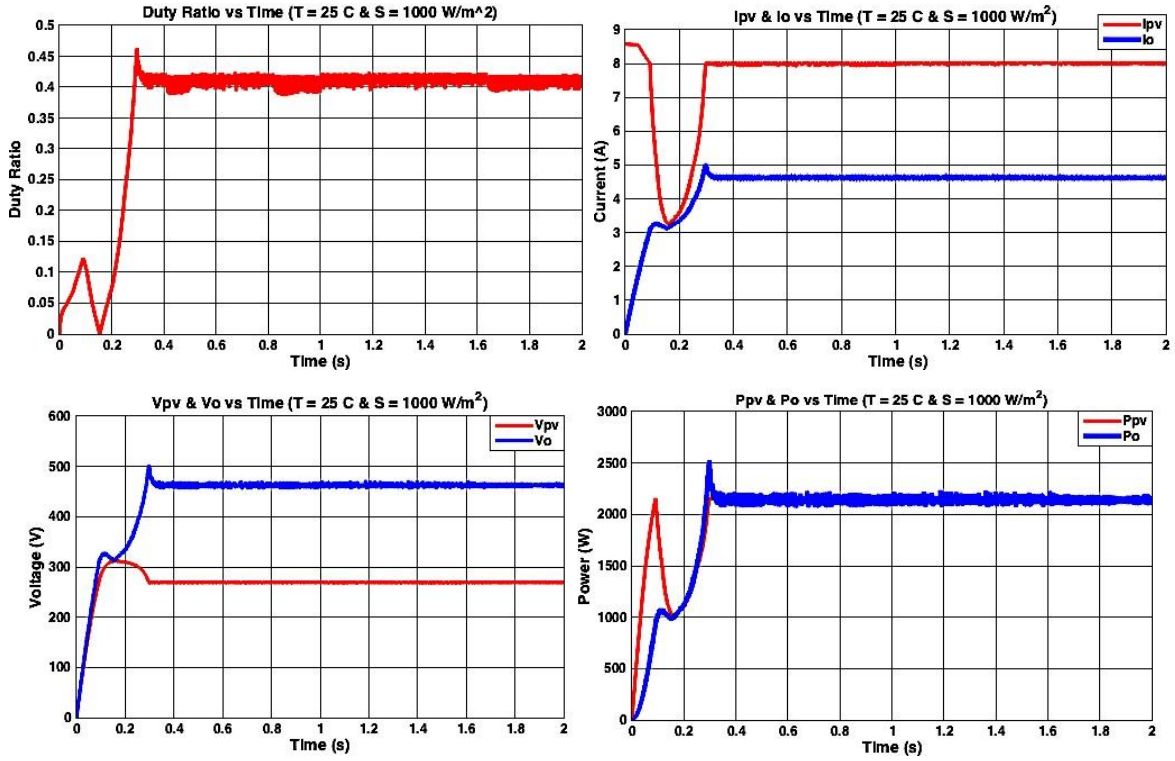

Figure 2.21: RCC MPPT algorithm case study 1 simulation results.

2.4.4.3 RCC MPPT Algorithm Case Study 2

Figure 2.22 demonstrates simulation results regarding evaluating system dynamics under small variations. In this case study, temperature has been kept constant at 25 °C and irradiance is fluctuating from 1000 W/m^2 to 800 W/m^2 at t = 1 s and from 800 W/m^2 to 600 W/m^2 at t = 2 s. Results are fairly compatible with expectations and also with theoretical calculations. The system shows good performance considering settling time that is equal to about 75 ms at t = 1 s and 60 ms at t = 2 s. However, negative overshoot level is relatively high, and it is around 31.25 % at t = 1 s and 63.16 % at t = 2 s. Therefore, measures are needed to be taken to limit overshoot magnitude. Summary of the simulation results is available in Table 2.8.

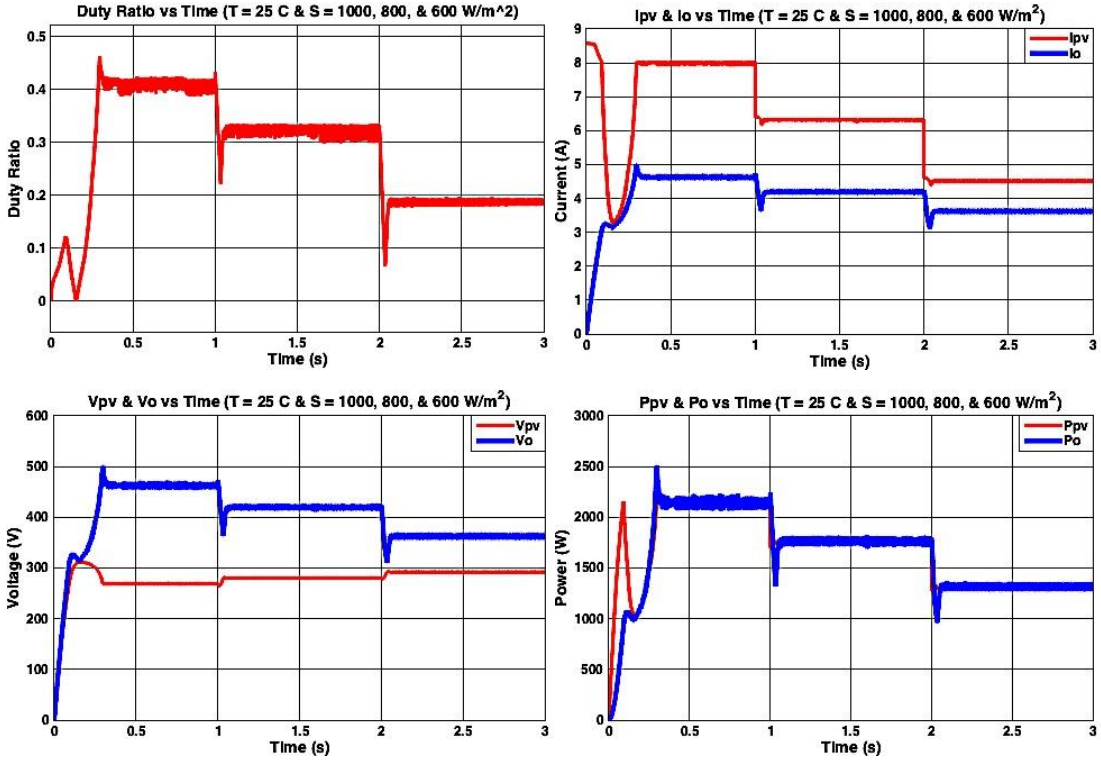

Figure 2.22: RCC MPPT algorithm case study 2 simulation results.

2.4.4.4 RCC MPPT Algorithm Case Study 3

To further study dynamic and transient performance of the system, its stability was examined under larger irradiance fluctuation. Unfortunately, the system became unstable and could not converge to the solution for irradiance variation of larger than 400 W/m^2. It seems the large negative overshoot is responsible for instability, and soon after the negative overshoot the system immediately settles at the origin. However, Figure 2.23 shows the dynamic stability under irradiance change from 1000 W/m^2 to 600 W/m^2 at t = 1 s and back to 600 W/m^2 at t = 2 s. It can be seen that the negative overshoot magnitude is so high, and is equal to 100%. To force the system to be stable, constant gain (K) was reduced; as a result, the system became slower and converged to initial condition after 600 ms; moreover, the settling time at t = 1 s was higher than the previous case, and was approximately 125 ms. Interestingly, positive overshoot and settling time at t = 2 s remained relatively constant. . Summary of the simulation results is available in Table 2.8.

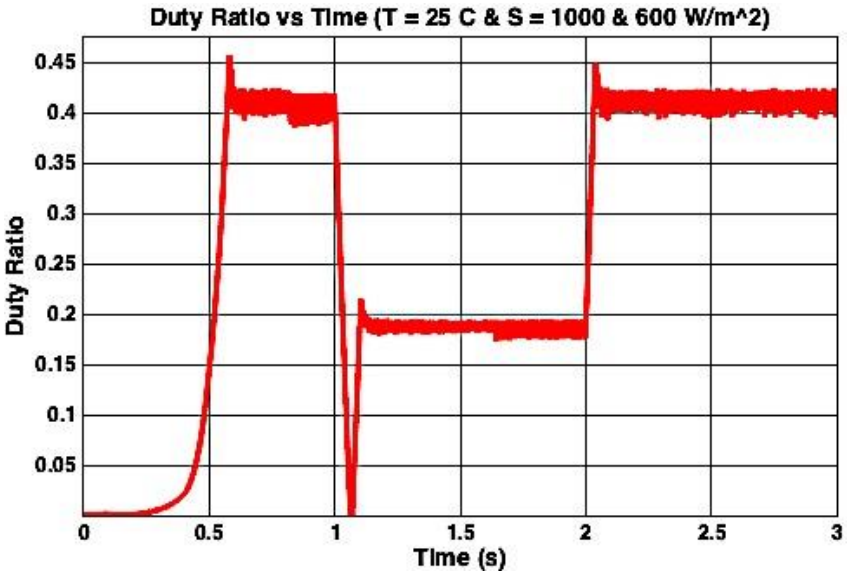

Figure 2.23: RCC MPPT algorithm case study 3 simulation results.

Table 2.8: Summary of RCC MPPT algorithm simulation results.

S (W/m^2)	I_{SC} (A)	D_{MPP}	V_{MPP} (V)	I_{MPP} (A)	P_{MPP} (W)	V_o (V)	I_o (A)	P_0 (W)
1000	8.59	0.41	269	8	2152	463	4.6	2130
800	6.9	0.32	280	6.3	1764	420	4.2	1764
600	5.1	0.19	292	4.5	1314	363	3.63	1318

2.5 Comparison of P&O and RCC MPPT algorithms

Comparing the results obtained from the two MPPT algorithms, it can be said that both methods show satisfactory performance. However, RCC MPPT can find MPP much faster than the P&O MPPT method. Indeed, it is able to converge to MPP after few hundreds of milliseconds, while the P&O MPPT transient time is 2 seconds at worst case scenario. Besides, RCC MPPT method steady state error is much lower than P&O MPPT strategy with an error level of equal to the step size. On the contrary, P&O MPPT seems to be more reliable than the RCC MPPT under large variations and shows better system performance during dynamics and transients. This is due to the large negative overshoot of RCC MPPT that can lead to instability of the algorithm.

Chapter 3

3 Modular Multilevel Converter

Modular multilevel converter (MMC) topology was first introduced by Marquardt in 2003 as a state-of-the-art technology for high voltage direct current (HVDC) applications [16]. However, MMC is now becoming one of the most promising type of voltage source converter (VSC) not only in HVDC systems but also it is achieving high popularity in other applications like flexible ac transmission systems (FACTS), offshore wind farms, photovoltaic (PV) systems, and variable speed drives [2], [17].

In this chapter, after introducing MMC topology, operating principle, and mathematical model; a primary model of MMC with phase-shifted pulse width modulation (PSPWM) technique is simulated. Furthermore, a typical MMC-based grid-connected photovoltaic conversion system operation with respect to P&O and RCC MPPT algorithms is investigated. Finally, phase disposition pulse width modulation (PDPWM) technique is applied to equip MMC with sub-module (SM) voltage balancing function.

3.1 MMC Topology and Characteristics

Figure 3.1 shows a typical MMC schematic diagram (double-star based configuration) that is a DC/three-phase AC converter. In this configuration each converter phase is called leg and every leg is composed of two upper (P) and lower (N) arms. As can be seen from the figure, in each arm there are a series connection of N cells or sub-modules (SM), an inductor, and a resistor [2].

Under normal operation of MMC, SMs are controlled to generate the required AC voltages. Indeed, SMs can be considered as controllable voltage sources. Among all possible SM circuit topologies, half bridge circuit or chopper-cell is the most popular one. This is due to the high-energy efficiency and low number of components in the aforementioned SM [2].

The arm inductor application is to control and limit the circulating current caused by instantaneous voltage differences of the arms by attenuating the switching components of the arm current. Besides, during the short circuit fault at the DC-side the arm inductor suppresses the fault current by providing low di/dt. On the other hand, to model the power losses within each arm of the MMC the arm resistor is used [2], [16]-[20].

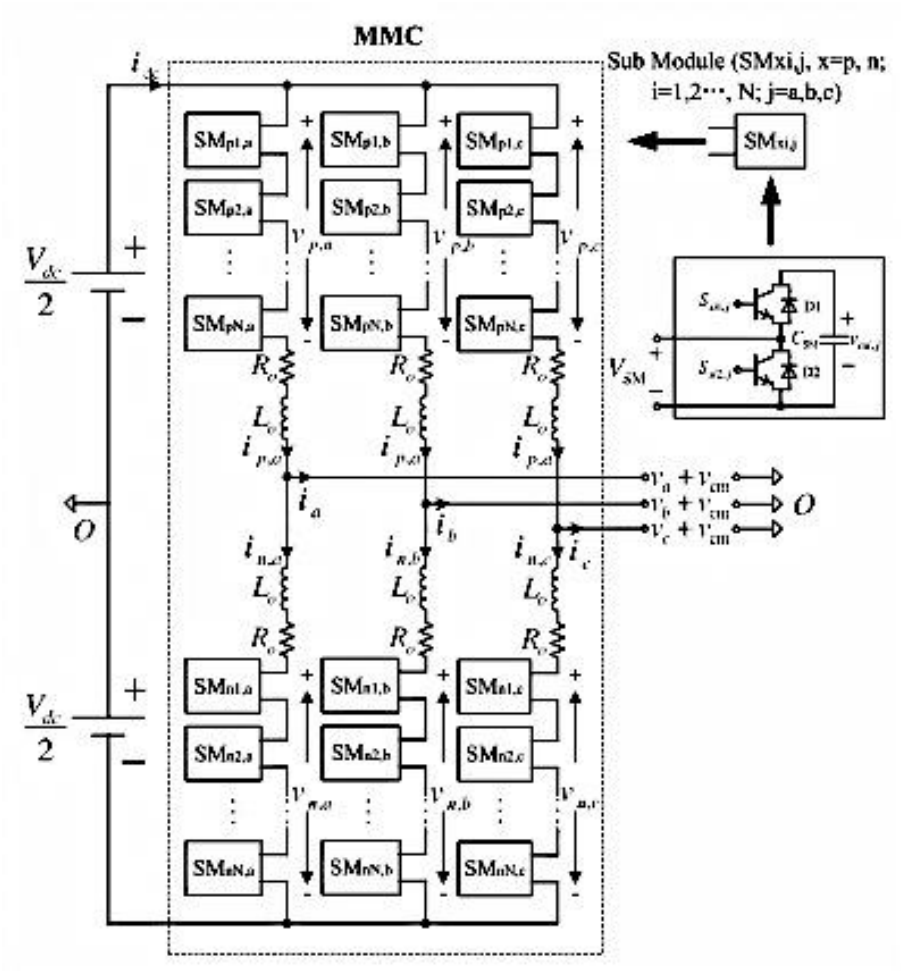

Figure 3.1: MMC schematic diagram [17].

Nowadays MMCs are becoming one of the most promising and widespread topologies among other multilevel converters in medium/high power/voltage applications as a result of their exceptional characteristics that some of them are presented as follows [2], [16]-[20]:

- Elimination or reduction of bulky passive filters as a result of the superior harmonic performance leading to low THD and excellent waveform quality of the AC-side
- Fast fault recovery because of the fact that DC-bus short circuit dose not discharge the SM capacitors
- High energy efficiency
- Low semiconductor power losses due to the small necessary switching frequency
- Modularity, redundancy, and scalability owing to the large number of SMs making MMCs applicable for any voltage level
- No need for concentrated DC-link capacitor resulting in low dv/dt and low device voltage stress
- No need for interfacing transformer especially for medium voltage applications

3.2 SM Operating Principles

Among various SM proposed configurations, half-bridge circuit or chopper-cell is the most popular one due to its better performance and lower cost. According to Figure 3.1, there are 2N SMs in every MMC leg, and the voltage across each SM is equal to V_{dc}/N. This is due to the fact that at every moment only N SMs in each leg are connected, and the sum of the SM voltages should be equal to V_{dc}. Every SM is composed of two complementary switches (i.e. IGBT/diode parallel combination) and one pre-charged capacitor. That is, when the lower switch is on the capacitor is bypassed, and the output voltage is equal to zero. On the contrary, when the upper switch is on the capacitor is charging or discharging (depending on the current direction) and the capacitor voltage is transferred to the output [17]. Figure 3.2 illustrates different states of the SM and the current flow direction. The state where both switches are connected is not allowed since it leads to short circuit across the capacitor, and only during the initial startup or due to a serious fault both switches are disconnected simultaneously [2], [21].

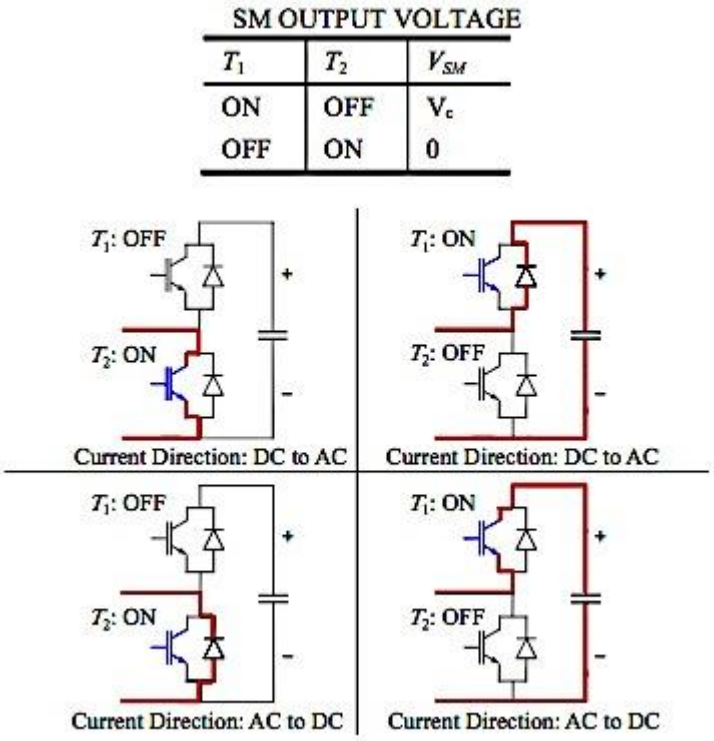

Figure 3.2: Different states of the SM and the current flow direction [21].

3.4 MMC Operating Principles

A typical DC/three-phase AC MMC that consists of three legs with 2N SMs in each leg generates N+1 levels in the output phase voltage and 2N+1 levels in the output line voltage [22]. In order to get the desired output voltage SMs are controlled by turning the SM switches on and off while at any moment during normal operation only N switches in each leg are on [2].

As a result it is required to charge all the SM capacitors to nominal value V_{dc}/N prior to normal operation. One approach is to individually energize each SM capacitor one after another by applying an external DC voltage source with lower voltage level than the main V_{dc} to avoid extremely high currents [16]-[18]. A better method is to add a resistor in series to the arm during the charging procedure and to bypass it later in normal operation. In this technique the main V_{dc} can be used and the external DC voltage source is eliminated [2], [23].

It can be said that, each MMC arm acts as a controllable voltage source. Throughout normal operation the output phase voltage varies between $-V_{dc}/2$ and $V_{dc}/2$ while the output line voltage fluctuates from $-V_{dc}$ to V_{dc} in steps of V_{dc}/N. For instance, to raise the output voltage it is needed to turn off upper arm SMs and turn on the same number of SMs in the lower arm simultaneously. However, it is better to increase or decrease the voltage one step at each switching time to improve the output waveform quality and reduce the harmonic pollutions [2], [24].

Accordingly, referring to Figure 3.1, the ideal upper arm and lower arm voltage waveforms as a result of sinusoidal modulation can be expressed as [20]:

$$V_{a\_upper\ arm}(t) = \left(\frac{1}{2} + m.sin(wt)\right)V_{dc} \tag{3.1a}$$

$$V_{a\_lower\ arm}(t) = \left(\frac{1}{2} - m.sin(wt)\right)V_{dc} \tag{3.1b}$$

Where m is the modulation index ($0 < m \leq 0.5$).

Therefore the phase voltage is,

$$V_{ao}(t) = -V_{a\_upper\ arm}(t) + \frac{V_{dc}}{2} = -m.\sin(wt)V_{dc} \tag{3.2}$$

3.5 MMC Mathematical Model

A typical DC/three-phase AC MMC circuit diagram is depicted in Figure 3.1, and based on this configuration the mathematical model is presented [2], [17].

The upper and lower arm currents ($i_{p,j}$ and $i_{n,j}$) are as follows:

$$i_{p,j} = \frac{i_{dc}}{3} + i_{circ,j} + \frac{i_j}{2} \tag{3.3a}$$

$$i_{n,j} = \frac{i_{dc}}{3} + i_{circ,j} - \frac{i_j}{2} \tag{3.3b}$$

Where i_{dc} is the DC component of the DC-side current, $i_{circ,j}$ is the circulating current of the leg j, and i_j is the AC current of phase j (j=a, b, c).

Then, the circulating current considering (3.3) is calculated as:

$$i_{circ,j} = \frac{i_{p,j} + i_{n,j}}{2} - \frac{i_{dc}}{3} \tag{3.4}$$

The mathematical equations defining the dynamic behavior of MMC are:

$$\frac{V_{dc}}{2} - V_{p,j} = L_0 \frac{di_{p,j}}{dt} + R_0 i_{p,j} + V_j + V_{cm} \tag{3.5a}$$

$$\frac{V_{dc}}{2} - V_{n,j} = L_0 \frac{di_{n,j}}{dt} + R_0 i_{n,j} - V_j - V_{cm} \tag{3.5b}$$

Where V_{dc} is the DC-link voltage, $V_{p,j}$ and $V_{n,j}$ are the upper and lower arm voltages of phase j respectively, and V_j and V_{com} are the fundamental and common mode components of the phase voltages respectively.

Afterwards, equation (3.6) is acquired from (3.3) and (3.5) (by subtracting (3.5b) from (3.5a) and substituting $i_{p,j}$ and $i_{n,j}$ from (3.3)):

$$V_j + V_{cm} = \frac{V_{n,j} - V_{p,j}}{2} - \frac{R_0}{2} i_j - \frac{L_0}{2} \frac{di_j}{dt} \tag{3.6}$$

Where R_0 and L_0 are arm resistance and inductance respectively.

Likewise, equation (3.7) is attained from (3.4) and (3.5) (by adding (3.5a) and (3.5b) and substituting $i_{circ,j}$ from (3.4):

$$L_0 \frac{di_{circ,j}}{dt} + R_0 i_{circ,j} = \frac{V_{dc}}{2} - \frac{V_{n,j} - V_{p,j}}{2} - R_0 \frac{i_{dc}}{3} \tag{3.7}$$

The upper and lower arm voltages of phase *j* can be explained as:

$$V_{p,j} = n_{p,j} V_{cp,j} \tag{3.8a}$$

$$V_{n,j} = n_{n,j} V_{cn,j} \tag{3.8b}$$

Where $n_{p,j}$ and $n_{n,j}$ are the number of SM in phase *j* in the upper and lower arm respectively, and $V_{cp,j}$ and $V_{cn,j}$ are the SM capacitor voltage in the upper and lower arm respectively.

Next, by replacing $V_{p,j}$ and $V_{n,j}$ from (3.8) to (3.6) and (3.7) equation (3.9) is derived:

$$V_j + V_{cm} = \frac{n_{n,j} V_{cn,j} - n_{p,j} V_{cp,j}}{2} - \frac{R_0}{2} i_i - \frac{L_0}{2} \frac{di_j}{dt} \tag{3.9a}$$

$$L_0 \frac{di_{circ,j}}{dt} + R_0 i_{circ,j} = \frac{V_{dc}}{2} - \frac{n_{n,j} V_{cn,j} + n_{p,j} V_{cp,j}}{2} - R_0 \frac{i_{dc}}{3} \tag{3.9b}$$

Furthermore,

$$P_{dc} = P_{ac} + P_{loss} \Rightarrow V_{dc} i_{dc} = \sum_{j=a,b,c} V_j i_j + P_{loss} \tag{3.10}$$

Consequently, $P_{p,j}$ and $P_{n,j}$ which are the upper and lower arm power of the phase *j* can be found from:

$$P_{p,j} = V_{p,j} i_{p,j} = n_{p,j} V_{cp,j} i_{p,j} \tag{3.11a}$$

$$P_{n,j} = \frac{dW_{n,j}}{dt} = \frac{d\left(\frac{N}{2} C_{SM} V_{cn,j}^2\right)}{dt} = V_{cn,j} N C_{SM} \frac{dV_{cn,j}}{dt} \tag{3.11b}$$

Besides, the upper and lower arm power of each phase can also be expressed as:

$$P_{p,j} = \frac{dW_{p,j}}{dt} = \frac{d\left(\frac{N}{2} C_{SM} V_{cp,j}^2\right)}{dt} = V_{cp,j} N C_{SM} \frac{dV_{cp,j}}{dt} \tag{3.12a}$$

$$P_{n,j} = \frac{dW_{n,j}}{dt} = \frac{d\left(\frac{N}{2} C_{SM} V_{cn,j}^2\right)}{dt} = V_{cn,j} N C_{SM} \frac{dV_{cn,j}}{dt} \tag{3.12b}$$

Where C_{SM} is the SM capacitance.

Finally, by combining (3.11) and (3.12) the dynamics of each SM capacitor voltage ripple can be presented as follows:

$$\frac{dV_{cp,j}}{dt} = \frac{i_{p,j}}{NC_{SM}} n_{p,j} = \frac{1}{NC_{SM}} \left(\frac{i_{dc}}{3} + i_{circ,j} + \frac{i_j}{2} \right) n_{p,j} \tag{3.13a}$$

$$\frac{dV_{cn,j}}{dt} = \frac{i_{n,j}}{NC_{SM}} n_{n,j} = \frac{1}{NC_{SM}} \left(\frac{i_{dc}}{3} + i_{circ,j} - \frac{i_j}{2} \right) n_{n,j} \tag{3.13b}$$

By using equations (3.3), (3.9), (3.10), and (3.13) a dynamic model of the MMC for control purposes can be achieved.

3.6 MMC Control Requirements

The main objective in MMC control is to manage the AC/DC currents and voltages at the converter terminals based on the application type to deliver high-energy efficiency and high quality waveforms at the lowest costs. In the following sections the most significant MMC control requirements and strategies are briefly introduced.

3.6.1 MMC Arm Current and Circulating Current Control

MMC arm current can be controlled to govern the converter input/output currents and voltages. Basically, arm voltages can control the arm current. Additionally, considering equation (3.3), it is apparent that circulating current is one of the arm current components, and it plays a key role in arm current control. Circulating current initiates from the instant voltage difference between the upper and lower arm, and contains negative sequence components with twice the fundamental frequency. This current component does not have any effect on the ac-side currents and voltages; however, it can increase the arm current magnitude, and subsequently enhances the MMC power loss and SM capacitor voltage ripple magnitude. Therefore, arm current is controlled to suppress the circulating current. Although the harmful effects of circulating current can be partly limited by proper sizing of the arm inductor, efficient control techniques are essential to successfully control and suppress it. Several strategies for MMC arm current and circulating current control have been proposed. Circulating current can be controlled independently or as a part of the arm current. For instance, it can be controlled during modulation stage independent of the arm current. Besides, applying resonant controllers or model-based predictive control (MPC) are other common control techniques for circulating current. Control methods for arm current are various and are not limited to the following

approaches: Closed-loop strategy using PI or LQR controllers, control based on Lagrange multipliers, indirect modulation techniques, predictive current control, and decoupled control models (using d-q coordinates, positive-negative sequence decomposition, etc.) [2], [17], [19].

3.6.2 SM Capacitor Voltage Control

So as to guarantee the appropriate operation of the MMC, SM capacitor voltage needs to be controlled. That is, the average value of all the capacitor voltages must be kept at a given voltage reference level. Besides, minimization of the capacitor voltage ripple is another objective. This voltage ripple that originates from the interaction between the arm current especially circulating current and modulation signals, contains fundamental and second harmonic components. Moreover, keeping the voltage balance among the arms is another element to be considered. To derive the dynamic model of the average capacitor voltage, all the capacitors in the MMC can be lumped into an equivalent one. Thus [2], [17], [19].

$$\frac{C_{eq}}{2}\frac{d}{dt}V_{c,avg}^2 = V_i i_i - V_o i_o - P_{losses} \tag{3.14}$$

Where the first term is the average energy variation in equivalent capacitor, and then the next terms show converter input power, output power, and power losses respectively. Apparently, to keep the capacitor average voltage constant at its reference value it is necessary that the input power be equal to the output power plus power losses. On the other hand, circulating current is the most pivotal component in control of the capacitor voltage ripple and the voltage balance among the arms. To suppress the capacitor voltage ripple, appropriate harmonic components are injected into the circulating current. And, to keep the voltage balance among the arms, arm current can be modified in each arm. However, only circulating current component of the arm current is usually adjusted to avoid the unwanted effects on input and output currents [2], [17], [19].

3.6.3 SM Capacitor Voltage Balance Control

One challenge in improvement of the MMC performance is to keep the voltage balance of SMs in each arm. In other words, the SM capacitor voltages need to be maintained at their reference value that is V_{dc}/N. Some techniques that have already been used to meet this demand are: Closed-loop controller for each SM using predictive strategy, phase-shifted carrier PWM (PSC-PWM) scheme, and sorting method. Sorting method is by far the most common voltage balance control technique. It basically depends on the current direction in each arm, modulation index, and SM capacitor voltage error. To carry out voltage balance control, SM capacitor voltages in

each arm are measured and sorted. Sorting algorithm can be implemented by using a look up table or can be integrated into the modulation strategy. The operation principle is that when the arm current direction is positive, SMs with the lowest capacitor voltage level are identified and triggered (they will start to charge). Whereas, SMs with highest capacitor voltage level are activated to discharge when the current direction is negative. It is worth mentioning that at any moment, only out of N SMs in each leg are inserted, and the capacitor voltages of the SMs that are bypassed remain constant. Sorting method has two major downsides that need special attention. One is the required processing time, and the other is the high switching frequency that increases the losses. Some methods are proposed to overcome these drawbacks like a closed-loop modified sorting method with a phase-shifted carrier PWM strategy, an open-loop method with selective harmonic elimination (SHE) PWM strategy, a predictive algorithm to calculate and distribute the amount of charge stored in the SM capacitors, etc. [2], [17], [19].

3.7 MMC with Phase-Shifted Pulse Width Modulation Simulation

In this section, MATLAB/Simulink simulation results of a three-phase four-level modular multilevel converter (MMC) with phase-shifted pulse width modulation (PSPWM) technique are given. The objective is to present an overview on MMC fundamental operating principles, as well as to evaluate the simulation model credibility by comparing the results with the mathematical equations. The overall view of the simulation model is demonstrated in Appendix A, and the parameters extracted from [20] are shown in Table 3.1 [2].

Table 3.1: MMC with PSPWM model parameters [2].

Parameters	*Value*	*Parameters*	*Value*
Fundamental Frequency	50 Hz	Arm Inductance	1.3 mH
Switching Frequency	2 KHz	Arm Resistance	0.4 Ω
Amplitude Modulation Index	0.95	SM Capacitance	6 mF
DC-Link Voltage	600 V	Load Inductance	30 mH
Number of SMs in each Arm	3	Load Resistance	8.5 Ω

The PSPWM technique is one of the multi-carrier PWM strategies that can easily be implemented. In this simulation, three sinusoidal balanced reference waveforms at fundamental frequency of 50 Hz with an amplitude modulation index of 0.95, and three triangular carriers at switching frequency of 2 KHz with 120° phase displacement regarding the number SMs in each arm are used [2].

The simulation results for AC-side phase and line voltages are shown in Figure 3.3 and Figure 3.4. As can be seen from the figures, the phase voltages are composed of four voltage levels (N_{SM}+1) of -300V, -100V, 100V, and 300V, whereas the line voltages consist of seven voltage levels (2*N_{SM}+1) of -600V, -400V, -200V, 0, 200V, 400V, and 600V. Equations for phase and line voltages are as follows [2]:

$$\begin{cases} V_a(t) = -m.\frac{V_{dc}}{2}.\sin(wt) + harmonics \\ V_b(t) = -m.\frac{V_{dc}}{2}.\sin\left(wt - \frac{2\pi}{3}\right) + harmonics \\ V_c(t) = -m.\frac{V_{dc}}{2}.\sin\left(wt - \frac{4\pi}{3}\right) + harmonics \end{cases} \tag{3.15}$$

$$\begin{cases} V_{ab}(t) = -m.V_{dc}.\sin(wt) + harmonics \\ V_{bc}(t) = -m.V_{dc}.\sin\left(wt - \frac{2\pi}{3}\right) + harmonics \\ V_{ca}(t) = -m.V_{dc}.\sin\left(wt - \frac{4\pi}{3}\right) + harmonics \end{cases} \tag{3.16}$$

Where, m is the amplitude-modulating index ($0 \leq m \leq 1$), and in this case m and V_{dc} are equal to 0.95, and 600 V respectively [2].

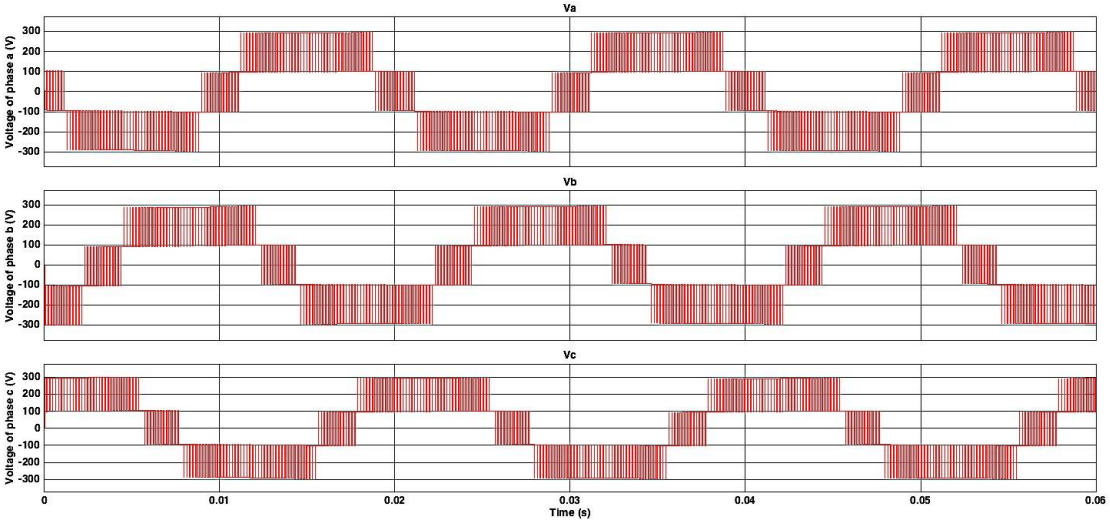

Figure 3.3: MMC with PSPWM AC-side phase voltages V_a, V_b, and V_c [2].

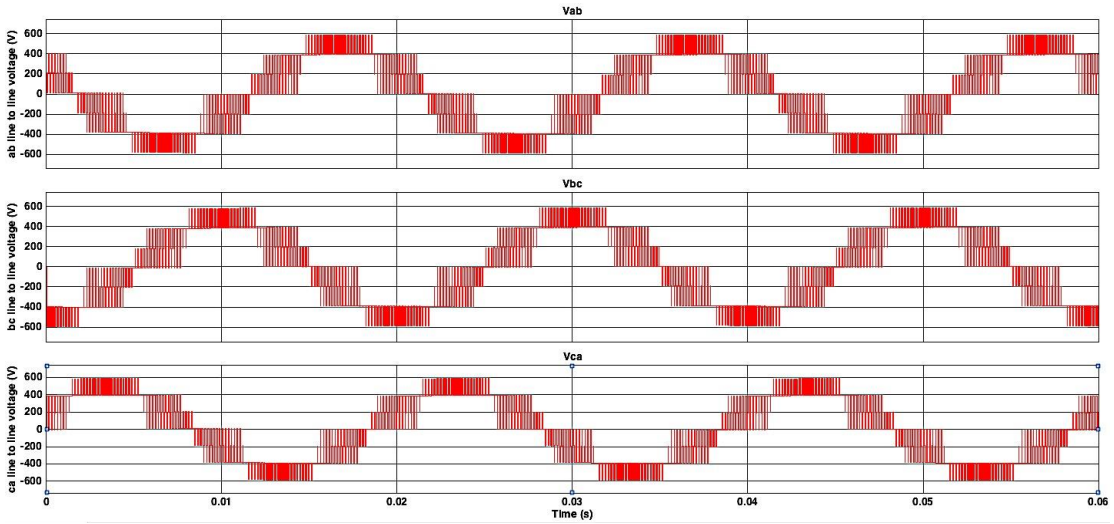

Figure 3.4: MMC with PSPWM AC-side line voltages V_{ab}, V_{bc}, and V_{ca} [2].

Figure 3.5 demonstrates the DC-side and AC-side currents. It is apparent from the figure that the DC-side current fluctuates between 15.5 A and 16 A, and maximum value of the AC-side current is approximately 24 A [2].

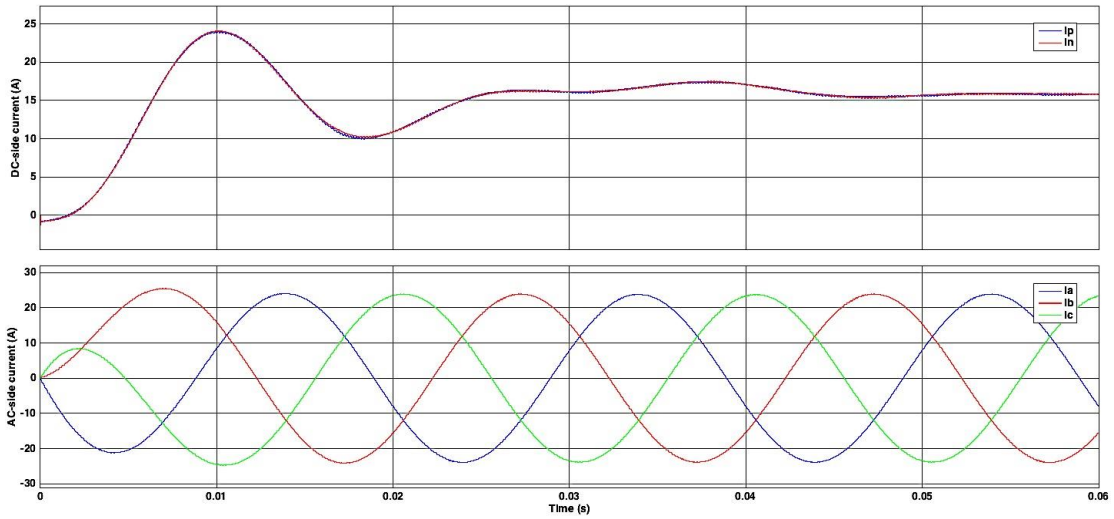

Figure 3.5: MMC with PSPWM (Up) DC-side currents, and (down) AC-side currents [2].

Upper arm and lower arm currents of the phases a, b, and c are depicted in Figure 3.6. It is known that arm currents contain DC component apart from the one half of the AC-side load current at fundamental frequency and circulating current at twice the fundamental frequency. As can be seen from the figure, the presence of DC component in arm currents can be validated. In fact, DC-side current divides equally among the three phases and improves the power balance in capacitors. Figure 3.7 shows the upper arm and lower arm SM capacitor voltages in each phase. Since the DC-link voltage is 600 V, the SM capacitor voltages are expected to be equal to 200 V (600 V / N_{SM}); however, they have voltage fluctuation between 195 V and 202 V. The

obtained results show the importance of integration of control techniques to balance the capacitor voltages and to suppress the circulating currents while the unbalance capacitor voltages can trigger the flow of circulating currents that leads to increased power loss and efficiency reduction [2].

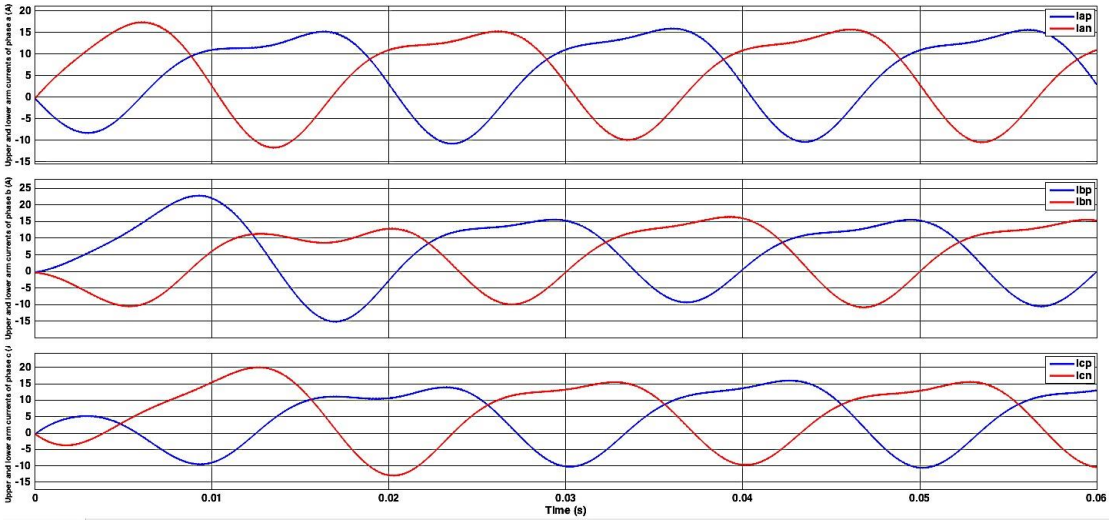

Figure 3.6: MMC with PSPWM upper arm and lower arm currents of the phases a, b, and c [2].

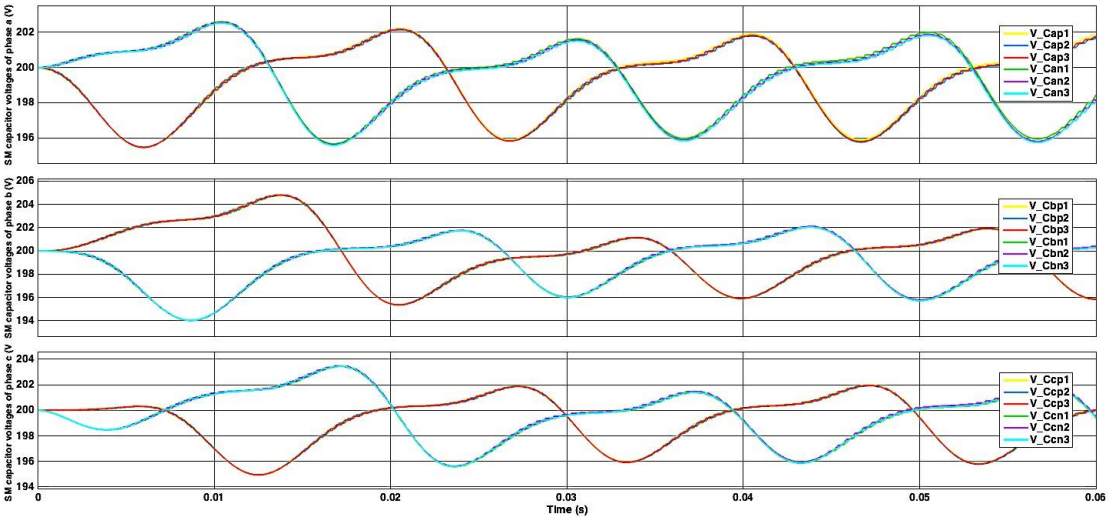

Figure 3.7: MMC with PSPWM upper arm and lower arm SM capacitor voltages of the phases a, b, and c [2].

The output voltage of SM at phase-a upper arm is shown in Figure 3.8 that can be used as a basis for evaluation of PWM performance. According to the figure, the SM is switched on and off 40 times within one period that corresponds to the applied switching frequency of 2 KHz (40 * 50 HZ = 2 KHZ) [2].

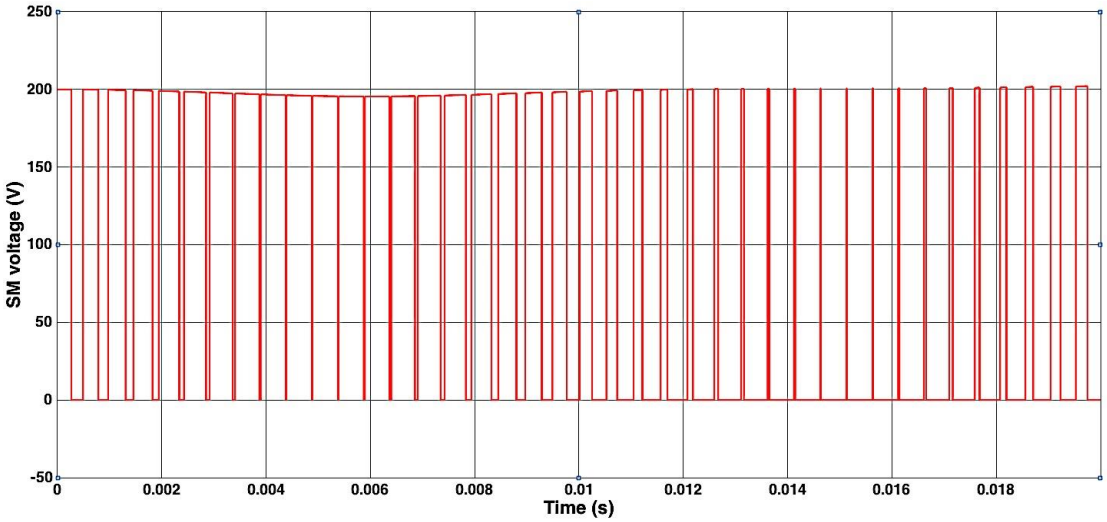

Figure 3.8: MMC with PSPWM: SM output voltage at phase-a upper arm [2].

Figure 3.9 display the frequency spectrum of the upper arm current and voltage respectively. The upper arm current total harmonic distortion (THD) is equal to 32.67%. It is clearly depicted in the figure that the arm current is formed due to the contribution of the DC-side current, AC-side current (first harmonic order), and circulating current (second harmonic order). On the other hand, upper arm voltage is composed of a DC component in addition to the fundamental frequency component that complies with the expectation. Anyhow, considering the high THD level of the phase and line voltages in Figure 3.10 confirm the requisite of implementation of effective voltage balancing control methods to improve the MMC performance [2].

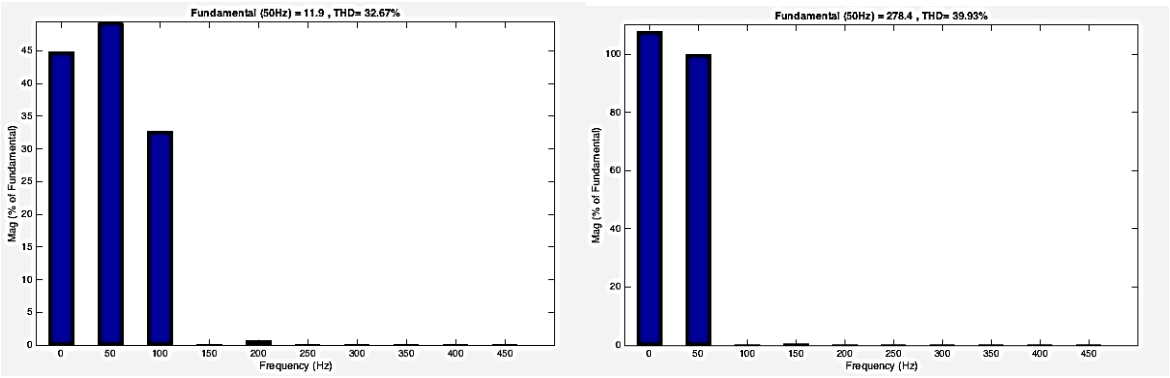

Figure 3.9: MMC with PSPWM (left) harmonic spectrum of the upper arm current, and (right) harmonic spectrum of the upper arm voltage [2].

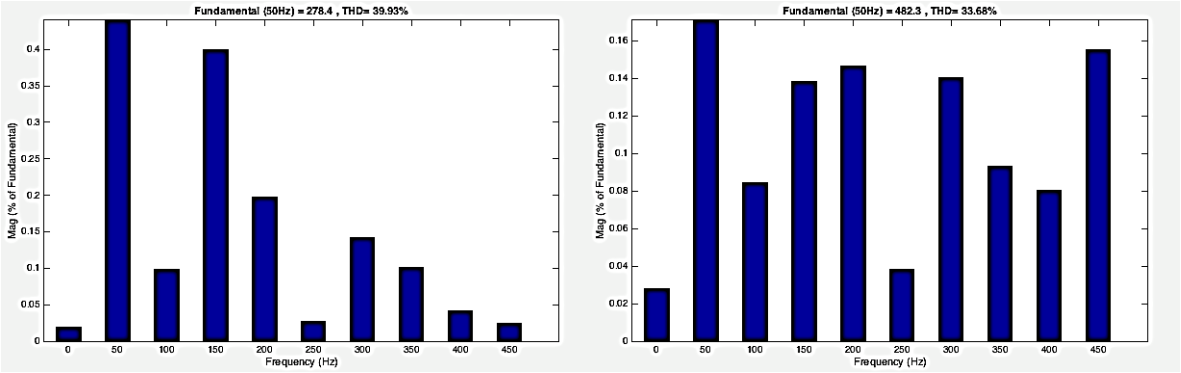

Figure 3.10: MMC with PSPWM (left) harmonic spectrum of the phase voltage, and (right) harmonic spectrum of the line voltage [2].

3.8 MMC-based Grid-Connected-Photovoltaic Conversion Plant Simulation

In this section, MATLAB/Simulink simulation results of a MMC-based grid-connected-photovoltaic conversion plant are given. One-line diagram of the simulation model is presented in Figure 3.11. As can be seen from the figure, the system is composed of two PV arrays that each array consists of nine solar cells (P_{rated} = 2161 W for each PV array). PV arrays are connected to a DC/DC boost converter where MPPT algorithm is also implemented. DC/DC boost converters are then linked to the grid via a three-phase four-level DC/AC modular multilevel converter (MMC) with phase-shifted pulse width modulation (PSPWM) technique. Parameters pertinent to the MMC are given in Table 3.2.

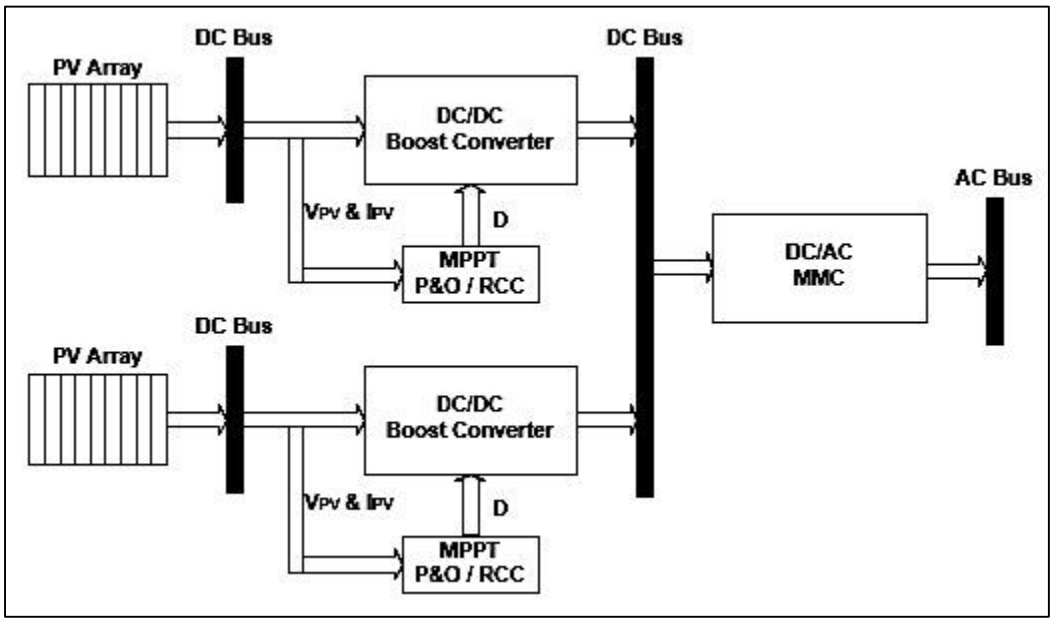

Figure 3.11: MMC based grid-connected-photovoltaic conversion plant one-line diagram.

Table 3.2: MMC-based grid-connected photovoltaic conversion plan model parameters.

Parameters	*Value*	*Parameters*	*Value*
Fundamental Frequency	50 Hz	Arm Inductance	1.3 mH
Switching Frequency	2 KHz	Arm Resistance	0.4 Ω
Amplitude Modulation Index	0.95	SM Capacitance	6 mF
Grid Voltage	600 V	Line Inductance	3000 uH
Number of SMs in each Arm	3	Line Resistance	82 Ω

First, the system is simulated without considering MPPT algorithm. Duty cycle is fixed at 0.5, and PV system is operating under STC conditions. Summary of the simulation results for each PV array are demonstrated in Table 3.3.

Table 3.3: Summary of the MMC-based grid-connected photovoltaic conversion plan without MMPT algorithm simulation results.

S (W/m^2)	D	V_{PV} (V)	I_{PV} (A)	P_{PV} (W)	V_{dC} (V)	I_{dc} (A)	P_{dc} (W)
1000	0.5	250	8	2000	492	4	1968

Figure 3.12 and Figure 3.13 show MMC AC-side phase voltages and line voltages respectively. Since MMC comprises of 3 SMs, phase voltages are composed of 4 voltage levels of -492 V, -164 V, 164 V and 492 V, whereas line voltages consisting of 7 voltage levels of -984 V, -656 V, -328 V, 0, 328 V, 656 V and 984 V.

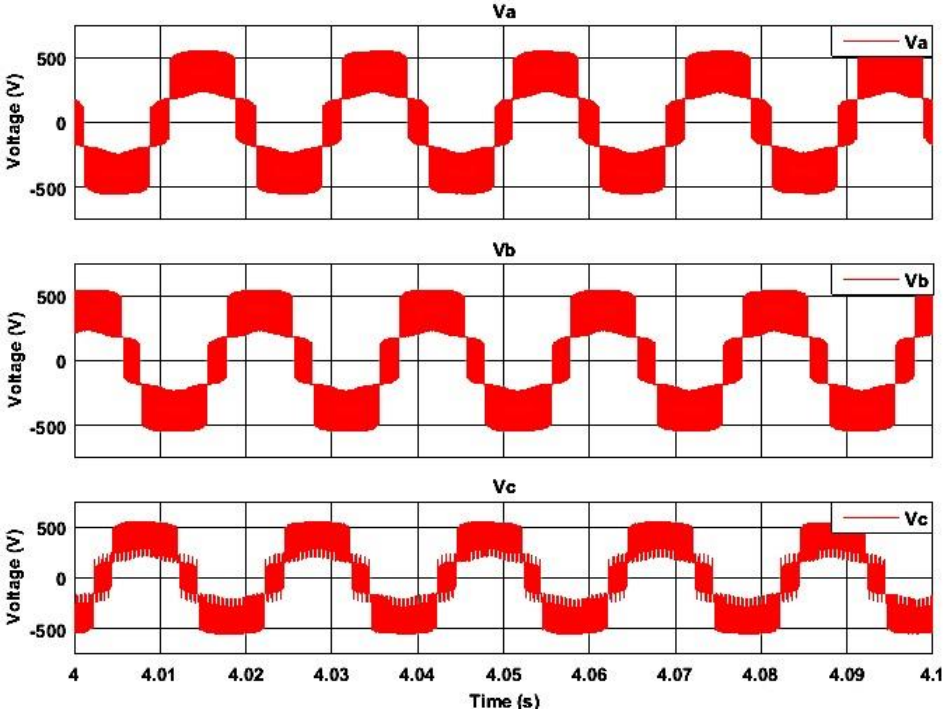

Figure 3.12: MMC-based grid-connected photovoltaic conversion plan without MMPT algorithm AC-side phase voltages Va, Vb, and Vc.

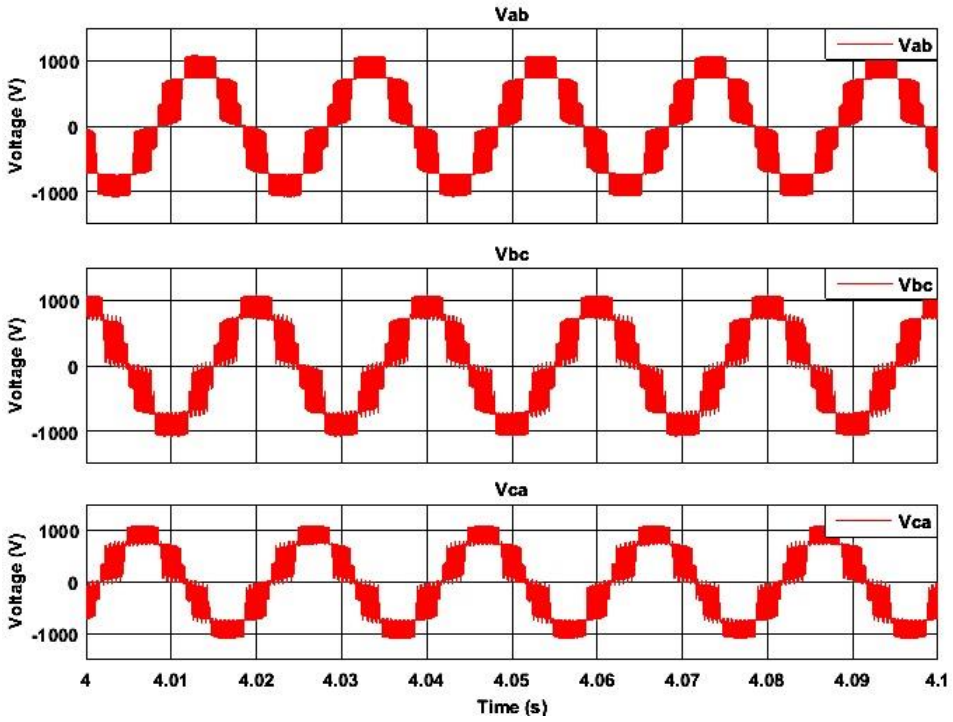

Figure 3.13: MMC-based grid-connected photovoltaic conversion plan without MMPT algorithm AC-side line voltages V_{ab}, V_{bc}, and V_{ca}.

MMC AC-side and DC-side currents are depicted in Figure 3.14. DC-side current is about 4 A, and is varying from 2 A to 6 A. The high level of current fluctuation can be due to the PV current and voltage ripples that are caused by the boost converter. AC-side current that is going to be injected into the grid is unbalanced. In fact, the supplied currents are not equal in magnitude and are not equally displaced in time. Phase a and c are approximately in-phase with magnitude of about 7.5 A, while phase b current is 180° displaced with magnitude of around 12.5 A.

Figure 3.15 demonstrates MMC upper arm and lower arm currents of the phases a, b, and c. As can be seen from the figure, upper arm and lower arm currents are 180° out of phase. It is known that, arm currents are a combination of DC component, AC-side current at fundamental frequency, and circulating current at twice the fundamental frequency. The presence of these components in arm currents is validated through Figure 3.9. Circulating current does not have any effect on AC-side current; however, by increasing the arm current amplitude it increases the losses and adversely affects the system performance.

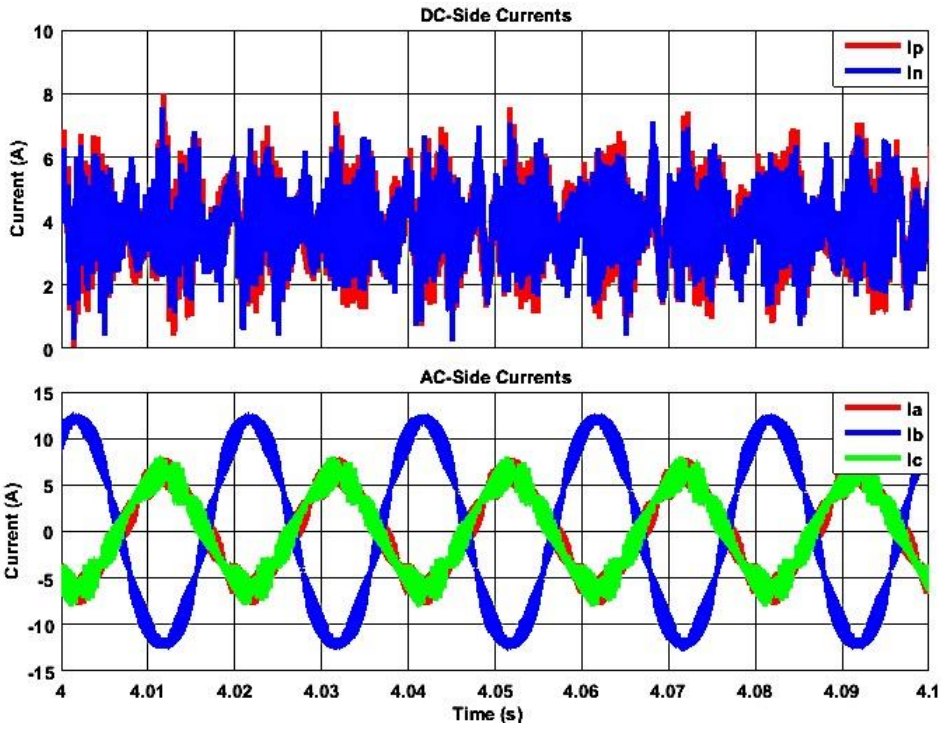

Figure 3.14: MMC-based grid-connected photovoltaic conversion plan without MMPT algorithm (Up) MMC DC-side currents, and (down) MMC AC-side currents.

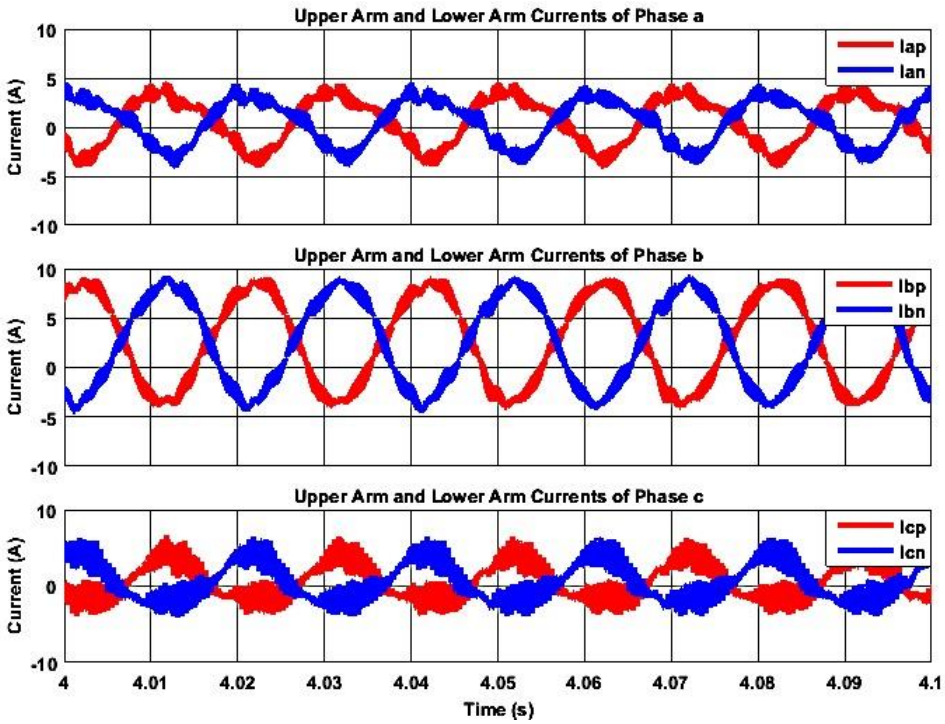

Figure 3.15: MMC-based grid-connected photovoltaic conversion plan without MMPT algorithm upper arm and lower arm currents of the phases a, b, and c.

SM capacitor voltages of phases a, b and c are shown in Figure 3.16. Since the DC-side voltage is almost 984 V, it is expected that capacitor voltages fluctuate around 328 V. Indeed, to guarantee the appropriate performance of MMC it is required that capacitor voltages being kept around their reference value (V_{dc} / N_{SM}), and not only the capacitor voltages in different phases, but also the capacitor voltages in the same arm be in balanced. Furthermore, level of the capacitor voltage ripple is required to be minimized as well. However, it is clear from the figure that this essential is not almost met in the system. Phase a and b capacitor voltages are fluctuating around 370 V instead of being 328 V; on the other hand, phase c capacitor voltages values ranging from 300 V to 425 V.

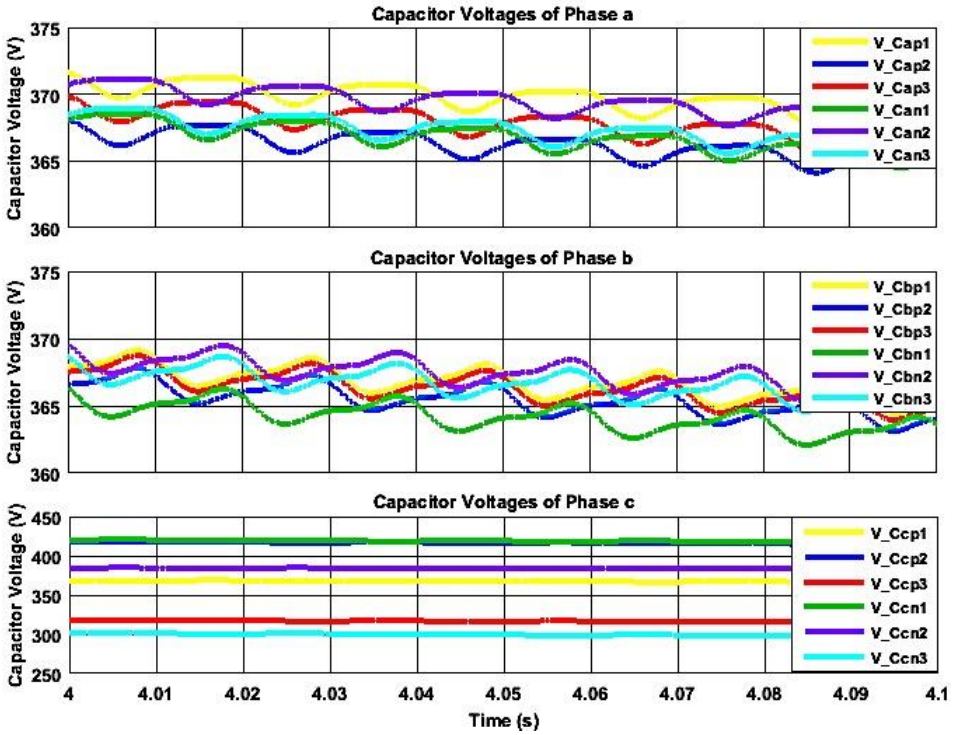

Figure 3.16: : MMC-based grid-connected photovoltaic conversion plan without MMPT algorithm upper arm and lower arm SM capacitor voltages of the phases a, b, and c.

System performance can be improved by implementation of MPPT algorithm to track maximum power under irradiance and temperature dynamics and transients. P&O and RCC MPPT algorithms are implemented in the system, and simulation results are summarized in Table 3.4, Figure 3.17 and Figure 3.18. It can be seen that both methods have converged to the same duty cycle value (D_{MPP} = 0.45); however, P&O MPPT technique convergence time is 6 seconds while RCC MPPT strategy meet the MPP after 4.8 seconds. A portion of convergence time is consumed for system initiation. Besides, RCC MPPT algorithm output power is slightly higher than the other method, and that can be related to the lower fluctuation level. This results in higher current level on AC-side of the MMC and higher injected power to the grid subsequently. Furthermore, SM capacitor voltages in RCC MPPT algorithm are more balanced than P&O MPPT method. Phase a and b SM capacitor voltages are relatively fluctuating around reference value of 328 V.

Table 3.4: Summary of the MMC-based grid-connected photovoltaic conversion plan with P&O and RCC MMPT algorithm simulation results under S = 1000 W/m^2.

S (W/m^2)	*MPPT*	D_{MPP}	V_{MPP} (V)	I_{MPP} (A)	P_{MPP} (W)	V_{dc} (V)	I_{dc} (A)	P_{dc} (W)
1000	P&O	0.45	261	8	2088	476	4.2	2000
1000	RCC	0.45	270	8	2160	490	4.2	2058

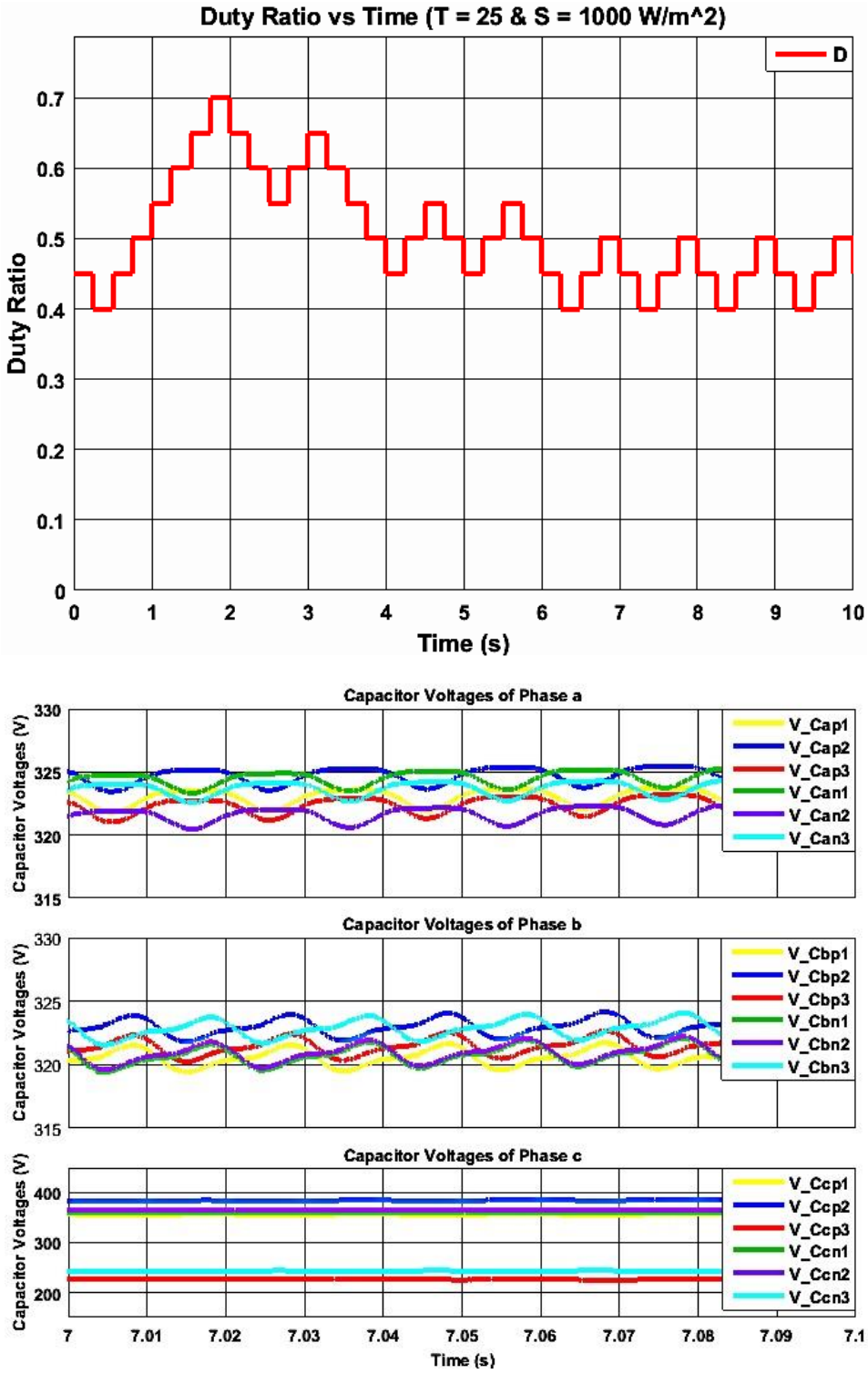

Figure 3.17: MMC-based grid-connected photovoltaic conversion plan with P&O MMPT algorithm under S = 1000 W/m^2 (Up) P&O duty ratio vs time, and(down) MMC upper arm and lower arm SM capacitor voltages of the phases a, b, and c.

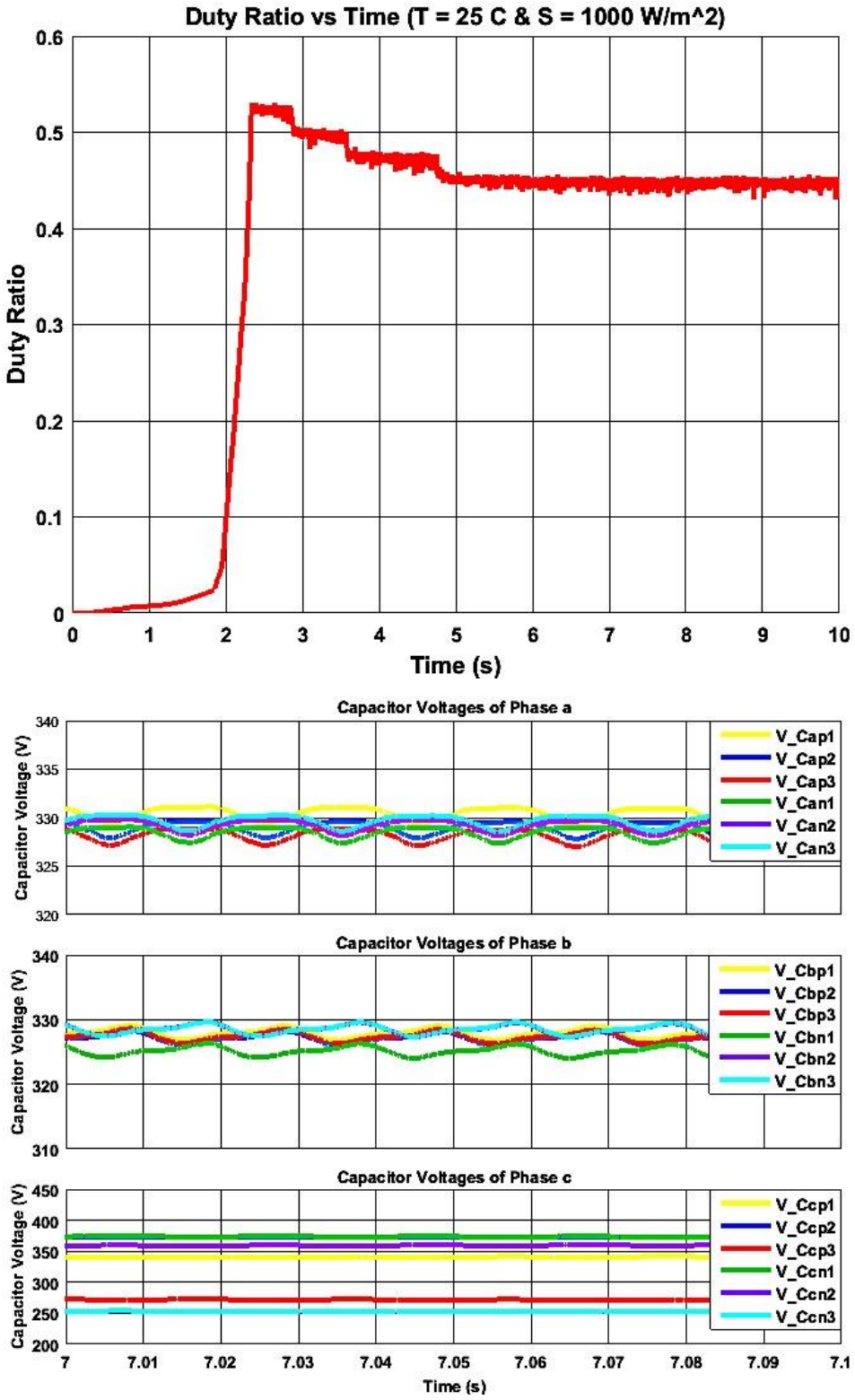

Figure 3.18: MMC-based grid-connected photovoltaic conversion plan with RCC MMPT algorithm under S = 1000 W/m^2 (Up) RCC duty ratio vs time, and (down) MMC upper arm and lower arm SM capacitor voltages of the phases a, b, and c.

To examine system behavior under transients and compare MPPT strategies, irradiance has been reduced from 1000 W/m^2 to 600 W/m^2 at t = 10 s. Simulation results are presented in Table 3.5, Figure 3.19. Both P&O and RCC MPPT techniques have converged to new duty cycle after around 13 seconds, and the travelled route in both methods are quite similar. As expected, system output power with RCC method is rather higher than P&O, and that can be justified as a reason for P&O induced perturbation that causes high level of fluctuation in resultant power.

Table 3.5: Summary of the MMC-based grid-connected photovoltaic conversion plan with P&O and RCC MMPT algorithm simulation results under S = 600 W/m^2.

S (W/m^2)	*MPPT*	D_{MPP}	V_{MPP} (V)	I_{MPP} (A)	P_{MPP} (W)	V_{dc} (V)	I_{dc} (A)	P_{dc} (W)
600	P&O	0.25	280	4.5	1260	375	3.3	1235
600	RCC	0.25	293	4.5	1316	390	3.3	1290

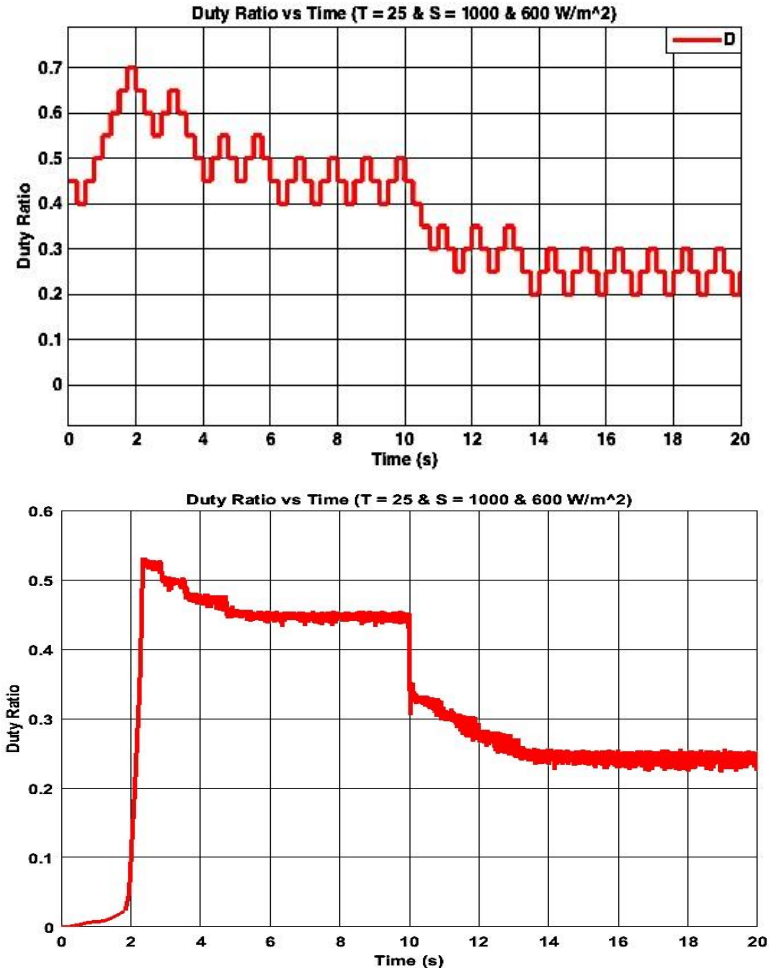

Figure 3.19: MMC-base grid-connected photovoltaic conversion plan with MMPT algorithm under S = 1000 W/m^2 and 600 W/m^2 (Up) P&O duty ratio vs time, and (down) RCC duty ratio vs time.

3.9 MMC with SM Capacitor Voltage Balancing Simulation

3.9.1 SM Capacitor Voltage Balancing Theory

SM capacitor voltage balancing is essential to assure proper performance of the MMC. Voltage balancing is necessary not only between MMC legs, but also among SMs of the same arm. Indeed, balancing strategy demands for SM capacitor voltages to fluctuate around their reference value. The applied SM capacitor voltage balancing method in this chapter is inspired from [25].

This methodology is an improved phase disposition pulse width modulation (PDPWM) technique based on selective virtual loop mapping (SVLM). PDPWM method in comparison with LSPWM produces higher total harmonic distortion (THD) on ac-side voltages; in addition, it increases amplitude of the circulating current leading to increased losses and decreased efficiency. This is due to the fact that PDPWM causes unequal distribution of voltage ripple across the SM capacitors [17]. However, PDPWM in combination with SVLM provides advantages making this methodology appropriate for SM capacitor voltage balancing [25]:

- Easily to be realized in field programmable gate arrays (FPGA).
- Good dynamic performance under transients.
- Suitable for MMCs with a large number of SMs, since it only demands for MIN and MAX capacitor voltages instead of sorting algorithm implementation that is really time consuming.

3.9.2 PDPWM Method

PDPWM method is described in this section while establishing virtual sub-module (VSM) concept. In this method N identical triangular carrier waveforms are displaced symmetrically with respect to zero axis. N is equal to the number of real SMs (RSM) in each arm, and RSMs are numbered from 1 to 2N in each leg. However, PDPWM results are first send to the VSMs, and then will be transferred to the RSMs based on a mapping rule descried in the next section. Figure 3.20 and Table 3.6 demonstrate the PDPWM modulation and carrier waveforms as well as PDPWM truth table. Modulation waveform is compared with carrier waveforms; if modulation waveform is higher than the carrier waveform at each region "1" is send to the related VSM; otherwise, "0" will be sent. For example, considering U_{mu} in region III, comparison results in region III are stored in P_3 whereas "1" is sent to VSMs $1^{'}$ and $2^{'}$, and "0"

is transferred to VSM 4'. VSMs of 5' to 8' will receive negated PWM signals of VSMs of 1' to 4' respectively.

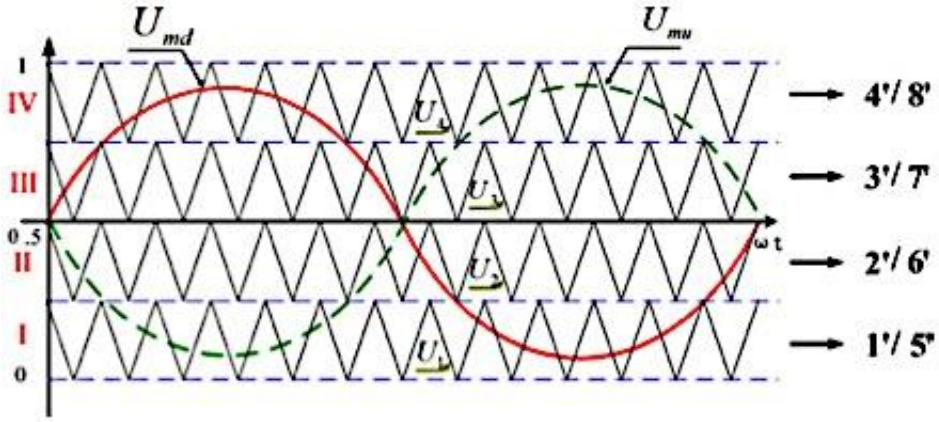

Figure 3.20: PDPWM modulation and carrier waveforms [25].

Table 3.6: PDPWM N+1 level modulation truth table [25].

Region	1'	2'	3'	4'	5'	6'	7'	8'	Range of Normalized Voltage
I	P1	0	0	0	P5	1	1	1	0 ~ 0.25
II	1	P2	0	0	0	P6	1	1	0.25 ~ 0.5
III	1	1	P3	0	0	0	P7	1	0.5~ 0.75
IV	1	1	1	P4	0	0	0	P8	0.75 ~ 1

P5– P8 is the corresponding negated PWM signal of P1~P4 respectively.

3.9.3 SVLM Method

Selective virtual loop mapping can be summarized in the following steps.

1) In the first step, SM capacitor voltages of the upper arm are compared, and corresponding RSM indices of the MIN and MAX capacitor voltages are stored in *Y*(1) and *Y*(2) respectively. Related block diagrams are shown in Figure 3.21[25].
2) In the second step, in case there are more than one MIN or MAX a priority check is carried out. For MIN capacitor voltage value assigning to Y(1), priority is defined as X1>X2>X3>X4 whereas for MAX value assigning to Y(2), priority is X4>X3>X2>X1 [25].

3) In this step, the remaining RSM indices are assigned to the rest of the *Y* array in sequence (*Y*(3), *Y*(4)) [25].

In the following steps, instead of multiport switch selector array implementation as in [25], MATLAB function blocks are used to write a MATLAB function to be used in the Simulink model.

4) In the next step, an intermediate *Z* array is introduced. Considering Table 3.6, it can be seen that there are four interesting VSMs $1^{'}$, $4^{'}$, $5^{'}$ and $8^{'}$. VSMs $1^{'}$ and $8^{'}$ output PWM in regions I and IV, and "1" in the other regions. Likewise, VSMs $4^{'}$ and $5^{'}$ output PWM in regions IV and I, and "0" in the other regions. Consequently, it can be said that, if the arm current direction is positive, RSM with MIN capacitor voltage can be mapped to VSM $1^{'}$ to be charged, and RSM with MAX capacitor voltage can be mapped to VSM $4^{'}$ to be discharged. If the arm current direction is negative the opposite is applicable. *Z*(1) and *Z*(2) can be allocated for storing those elements of *Y* array needed to be charged and discharged respectively. On the other hand, *Z*(3) and *Z*(4) can be assigned for the rest of the *Y* array elements by the aid of a counter "C_M" counting up from 1 and *N*-2 (2 in this case) at switching frequency.
5) In the last step, content of the *Z* array elements are read to figure out which VSM signal should be connected to which RSM one. For instance, if *Z*(1) = 3, it means that RSM = 3 needs to be charged; hence, VSM = $1^{'}$ will be mapped to RSM = 3.

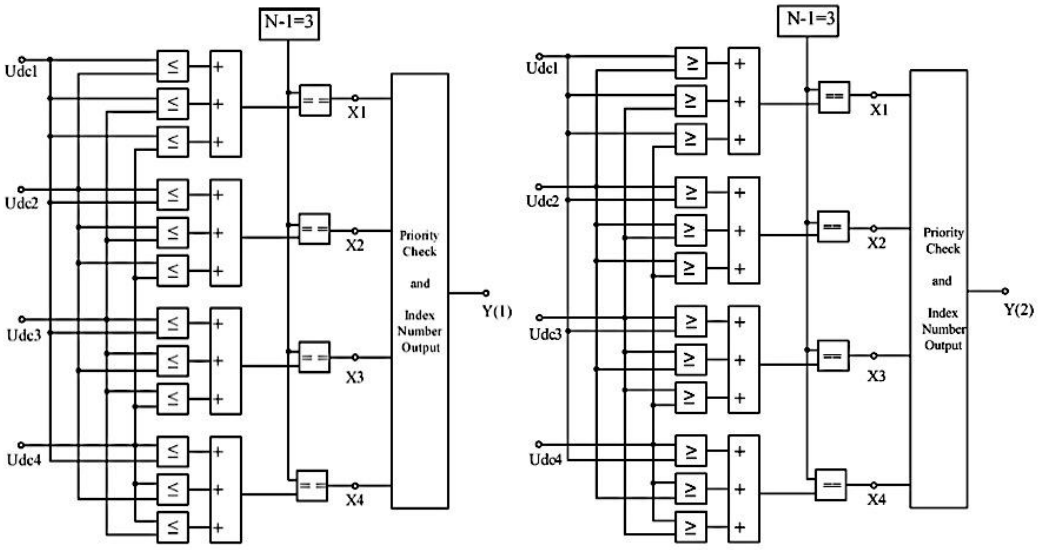

Figure 3.21: SVLM MIN and MAX block diagram [25].

3.9.4 SM Capacitor Voltage Balancing Simulation

The aforementioned capacitor voltage balancing technique is implemented in the MMC-based grid-connected photovoltaic conversion plant while DC/DC converter duty ratio is fixed at 0.5. MMC parameters and MATLAB/Simulink simulation results are summarized in Table 3.7 and Table 3.8. Figure 3.22 shows the PDPWM modulation and carrier waveforms of VSMs for phase-a. As can be seen there is one carrier waveform for each SM in each arm, and theses carriers are displaced symmetrically with respect to the zero axis.

Table 3.7: MMC with SM capacitor voltage balancing model parameters.

Parameters	*Value*	*Parameters*	*Value*
Fundamental Frequency	50 Hz	Arm Inductance	1.3 mH
Switching Frequency	2 KHz	Arm Resistance	0.4 Ω
Amplitude Modulation Index	0.45	SM Capacitance	6 mF
Grid Voltage	600 V	Line Inductance	3000 uH
Number of SMs in each Arm	4	Line Resistance	82 Ω

Table 3.8: Summary of MMC with SM capacitor voltage balancing algorithm simulation results under S = 1000 W/m^2.

S (W/m^2)	***D_{PV}***	***V_{PV}* (V)**	***I_{PV}* (A)**	***P_{PV}* (W)**	***V_{dc}* (V)**	***I_{dc}* (A)**	***P_{dc}* (W)**
1000	0.5	238.5	8.18	1950	475	4	1900

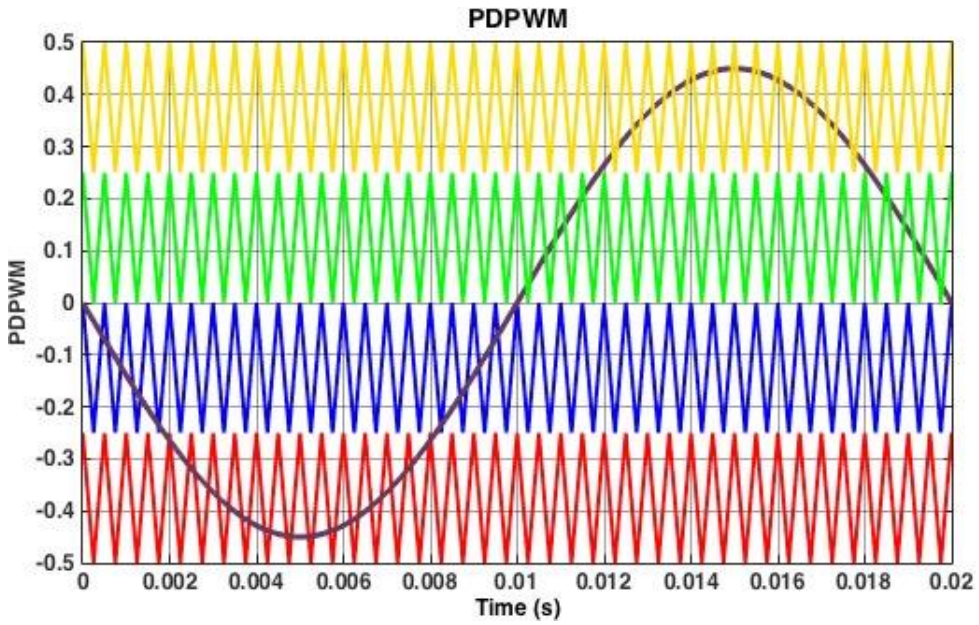

Figure 3.22: PDPWM modulation and carrier waveforms.

Figure 3.23 demonstrates SM capacitor voltage at phase-a upper arm. It fluctuates between 0 and 237.5 V that is equal to one fourth of the input DC voltage received from PV system. Furthermore, SM is switched on and off 20 times within one period (20 * 50 HZ = 1 KHZ) that corresponds to half of the applied switching frequency that is 2 KHz. In fact, it can be said that unlike the PSPWM method the effective switching frequency in PDPWM strategy is half of the applied switching frequency.

Figure 3.24 and Figure 3.25 depicts AC-side 5-level phase voltages and AC-side 9-level line voltages respectively. Figure 3.26 and Figure 3.27 presents AC-side currents and MMC upper arm and lower arm currents that demand for current control implementation.

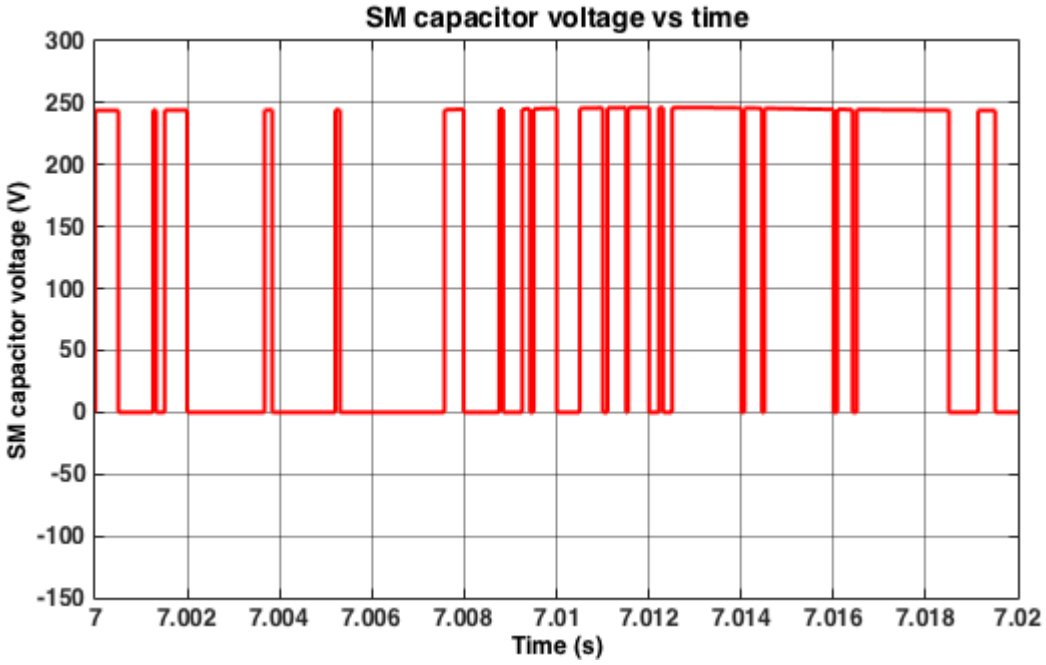

Figure 3.23: MMC with SM capacitor voltage balancing algorithm: SM output voltage at phase-a upper arm.

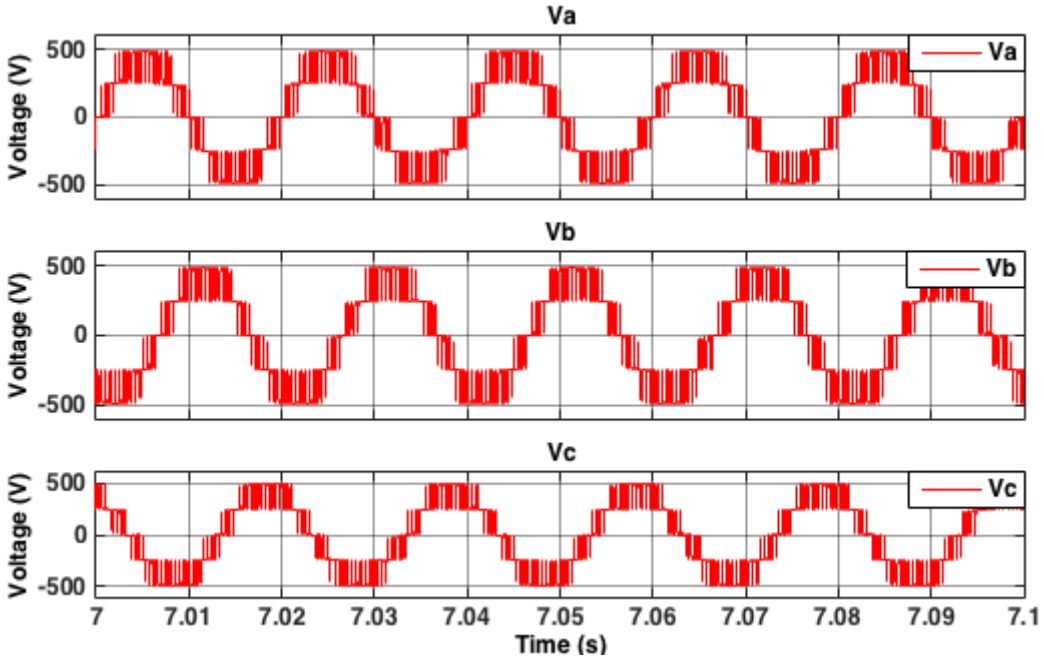

Figure 3.24: MMC with SM capacitor voltage balancing algorithm AC-side phase voltages V_a, V_b, and V_c.

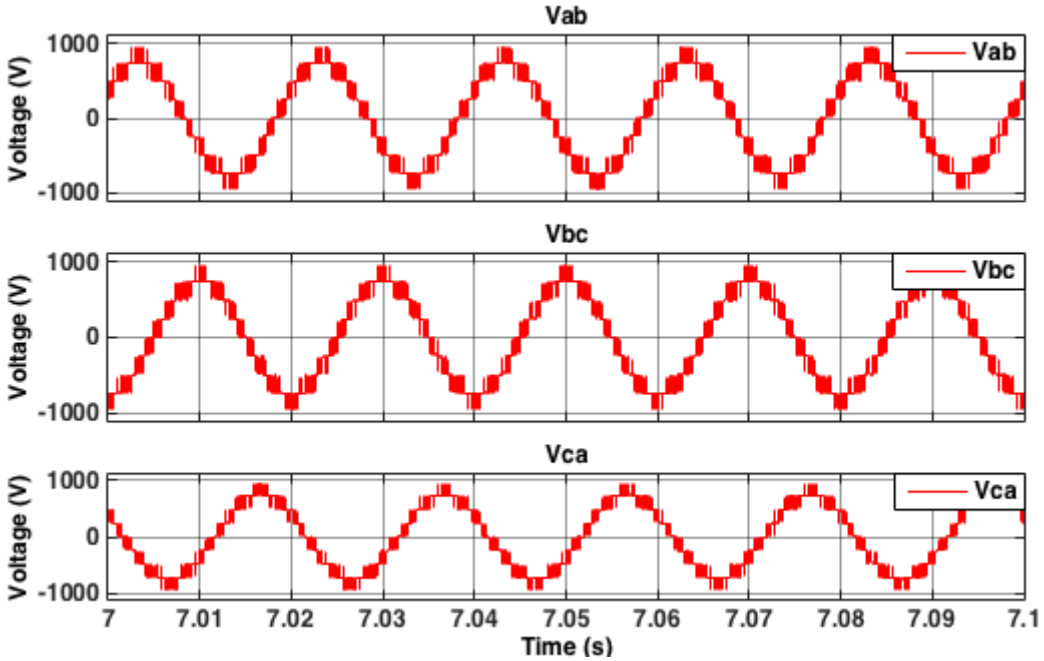

Figure 3.25: MMC with SM capacitor voltage balancing algorithm AC-side line voltages V_{ab}, V_{bc}, and V_{ca}.

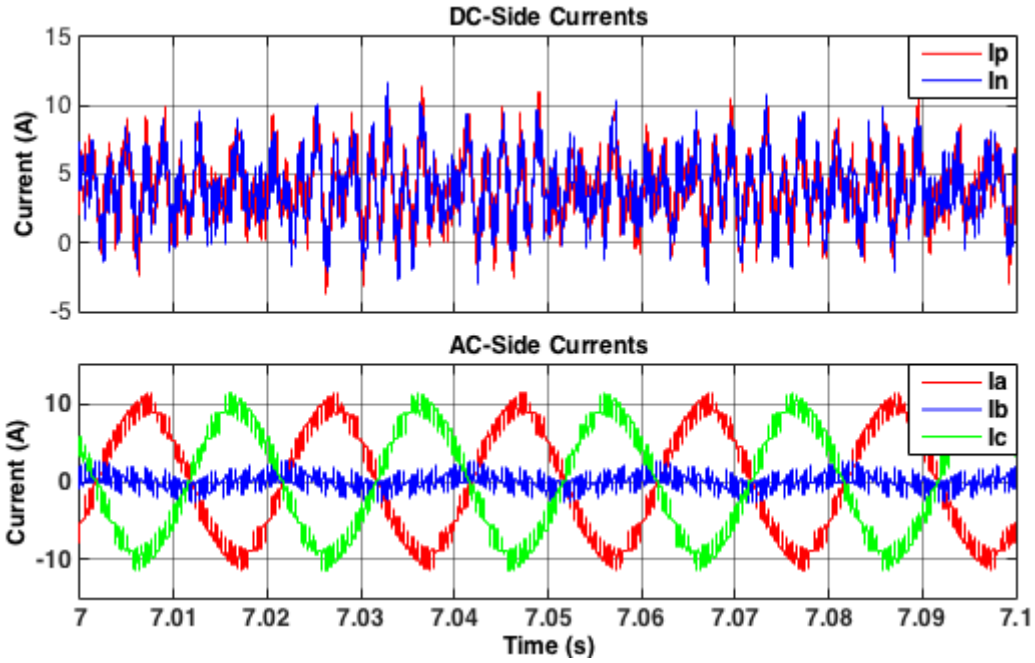

Figure 3.26: MMC with SM capacitor voltage balancing algorithm (Up) MMC DC-side currents, and (down) MMC AC-side currents.

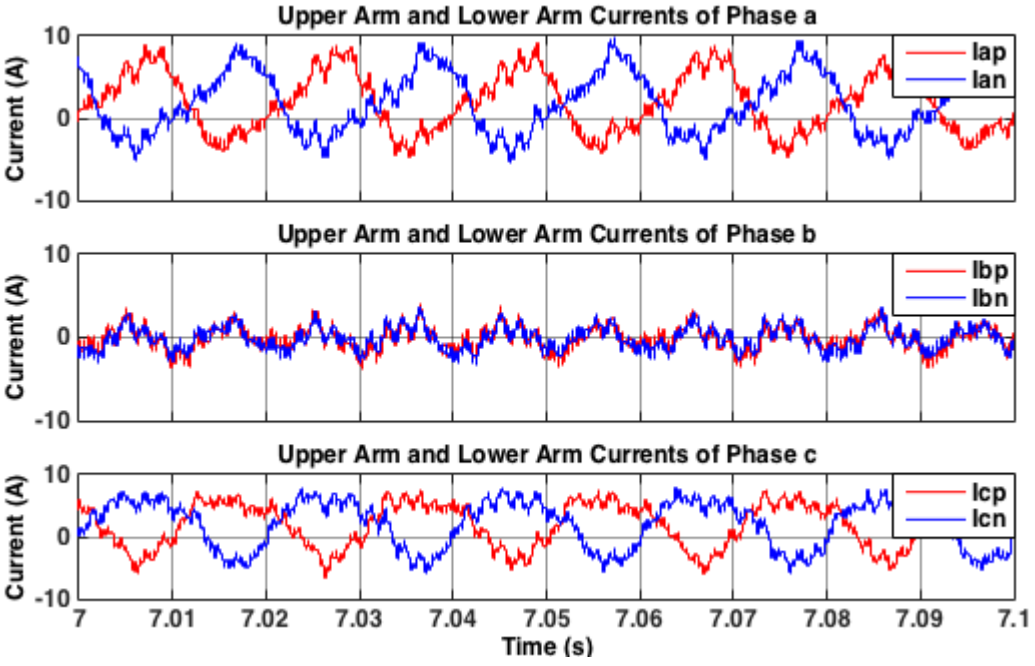

Figure 3.27: MMC with SM capacitor voltage balancing algorithm upper arm and lower arm currents of the phases a, b, and c.

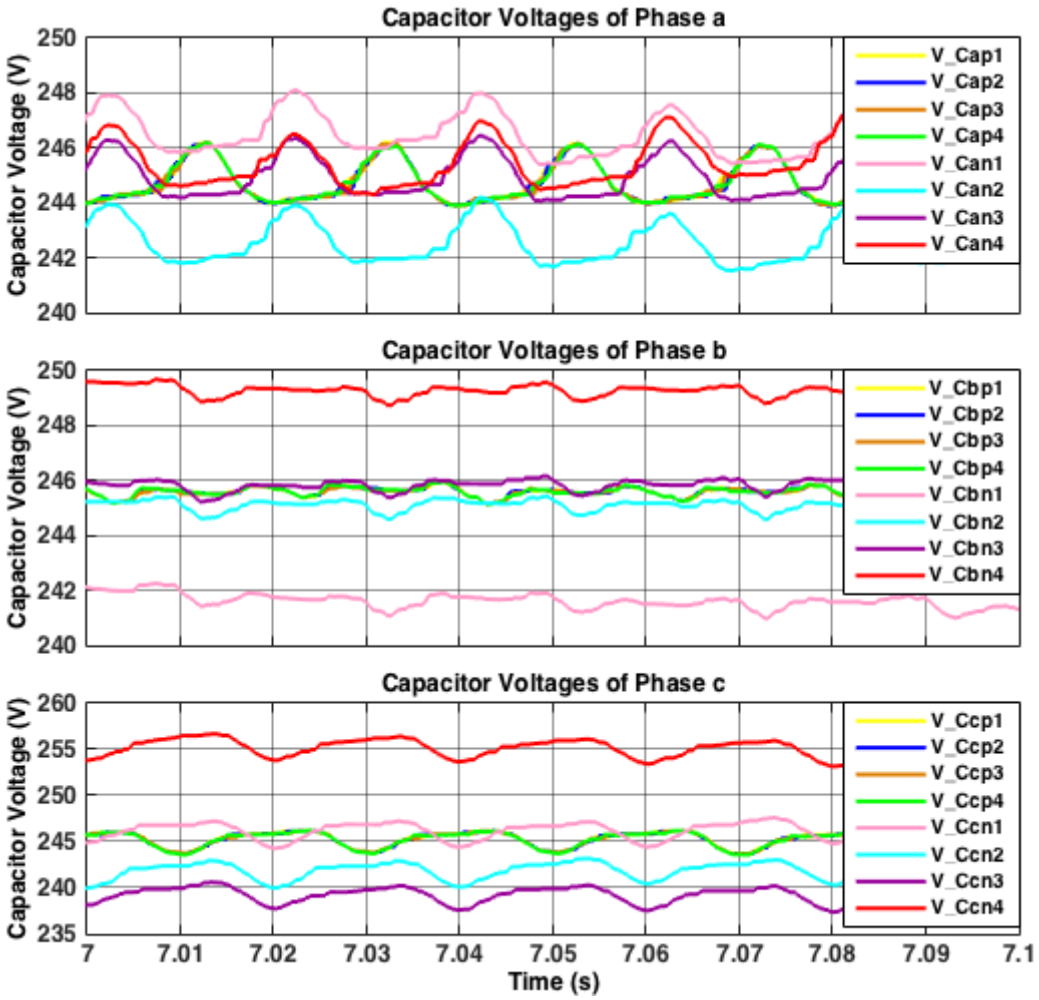

Figure 3.28: : MMC with SM capacitor voltage balancing algorithm upper arm and lower arm SM capacitor voltages of the phases a, b, and c.

Figure 3.28 shows SM capacitor voltage balancing results. It can be seen that the four upper arm capacitor voltages are completely coincide with each other (mostly green line). However, the four lower arm capacitor voltages are not still balanced although they follow each other closely. This can be justified as a result of demand for current control. Since currents are not still balanced, upper arm and lower arm capacitor voltages' behavior are not entirely symmetrical. In other words, upper arm and lower arm capacitors do not charge and discharge at the same rate.

Chapter 4

4 Current Control of MMC-based Grid-Connected Photovoltaic Power Plant

To assure proper operation of the MMC-based grid-connected photovoltaic power plant, and to improve the performance under dynamics and transients, implementation of an efficient control system is inevitable. Control system needs to be responsible for keeping the photovoltaic system operating point at maximum power under different irradiances and temperatures to improve the system efficiency by maximizing the amount of power delivered to the grid. Furthermore, the control system should guarantee the accepted power quality injected to the grid. In other words, injected current to the grid should be balanced, that is the three phases require to have equal amplitudes and equally displaced in time. Moreover, injected current waveform to the grid is required to be as sinusoidal as possible while having an amplitude close to the rated value, a frequency equal to grid frequency, and a phase angle equal to grid voltage's phase angel.

In this chapter, after introduction and implementation of the conventional control method including modulus optimum and symmetrical optimum techniques for tuning of system current and voltage controllers, simulation results are presented. Furthermore, non-linear current control design base on internal model-based control (IMBC) method is also studied.

4.1 Conventional Control Method Implementation

4.1.1 Inner Current Control Loop Implementation

In this section, the conventional direct and quadrature current control method is implemented [26]-[29]. The aim is to control the currents such that balanced high quality three phase currents are injected to the grid at unity power factor. The first step is to drive the dynamic model of the MMC on the ac-side in the *abc*-reference frame.

$$V_{c,abc} = Ri_{l,abc} + L\frac{di_{l,abc}}{dt} + V_{g,abc} \tag{4.1}$$

where $V_{c,abc}$ are the MMC ac-side voltages, R and L are line resistances and inductances respectively, $i_{l,abc}$ are the line currents, and $V_{g,abc}$ are the grid voltages.

Then, using Clark's transformation *abc* variables are transformed into *αβ0*-stationary reference frame.

$$\begin{bmatrix} V_{c,\alpha} \\ V_{c,\beta} \\ V_{c,0} \end{bmatrix} = \frac{2}{3} \begin{bmatrix} 1 & -\frac{1}{2} & -\frac{1}{2} \\ 0 & \frac{\sqrt{3}}{2} & -\frac{\sqrt{3}}{2} \\ \frac{1}{\sqrt{2}} & \frac{1}{\sqrt{2}} & \frac{1}{\sqrt{2}} \end{bmatrix} \begin{bmatrix} V_{c,a} \\ V_{c,b} \\ V_{c,c} \end{bmatrix} \tag{4.2}$$

Consequently,

$$V_{c,\alpha\beta 0} = Ri_{l,\alpha\beta 0} + L\frac{di_{l,\alpha\beta 0}}{dt} + V_{g,\alpha\beta 0} \tag{4.3}$$

Next, by the aid of Park's transformation, first-order differential equation of (4.3) can be transformed into *dq0*-rotating reference frame.

$$\begin{bmatrix} V_{c,d} \\ V_{c,q} \\ V_{c,0} \end{bmatrix} = \begin{bmatrix} \cos(wt) & \sin(wt) & 0 \\ -\sin(wt) & \cos(wt) & 0 \\ 0 & 0 & 1 \end{bmatrix} \begin{bmatrix} V_{c,\alpha} \\ V_{c,\beta} \\ V_{c,0} \end{bmatrix} \tag{4.4}$$

As a result, equation (4.3) in *dq0*-rotating reference frame becomes as follows:

$$V_{c,dq0} = Ri_{l,dq0} + L\frac{di_{l,dq0}}{dt} + jwLi_{l,dq0} + V_{g,dq0} \tag{4.5}$$

Since system is assumed to be balanced $V_{c,0}$ can be neglected, and considering $X_{dq} = X_d + jX_q$, equation (4.5) becomes:

$$V_{c,d} = Ri_{l,d} + L\frac{di_{l,d}}{dt} - wLi_{l,q} + V_{g,d} \tag{4.6a}$$

$$V_{c,q} = Ri_{l,q} + L\frac{di_{l,q}}{dt} + wLi_{l,d} + V_{g,q} \tag{4.6b}$$

It is apparent from equation (4.6) there is a coupling term, $wLi_{l,dq}$, between direct and quadrature axes. This coupling term can be compressed in a control input to be compensated as below:

$$V_d = V_{c,d} + wLi_{l,q} - V_{g,d} \tag{4.7a}$$

$$V_q = V_{c,q} - wLi_{l,d} - V_{g,q} \tag{4.7b}$$

Substituting equation (4.7) to (4.6) results in,

$$V_{dq} = Ri_{l,dq} + L\frac{di_{l,\mathrm{dq}}}{dt} \tag{4.8}$$

Laplace transform of (4.8) is,

$$V_{dq} = RI_{l,dq} + LsI_{l,dq} \tag{4.9}$$

Per-unitizing (4.9) leads to,

$$V_{dq,PU}V_B = R_{PU}Z_B I_{l,dq,PU}I_B + \frac{L_{PU}}{w_B}Z_B sI_{l,dq,PU}I_B \tag{4.10}$$

Thus,

$$V_{dq,PU} = R_{PU}I_{l,dq,PU} + \frac{L_{PU}}{w_B}sI_{l,dq,PU} \tag{4.11}$$

Therefore, system transfer function is equal to,

$$G_s(s) = \frac{I_{l,dq,PU}}{V_{dq,PU}} = \frac{1}{R_{PU} + s\frac{L_{PU}}{w_B}} = \frac{\frac{1}{R_{PU}}}{1 + s\frac{L_{PU}}{w_B R_{PU}}} = \frac{K}{1+sT} \tag{4.12}$$

On the other hand, PWM transfer function can be stated as,

$$G_{PWM}(s) = \frac{1}{1 + s\frac{1}{2f_s}} = \frac{1}{1+sT_d} \tag{4.13}$$

where f_s is the switching frequency, and T_d is the time delay.

Considering *d*-axis current control loop block diagram depicted in Figure 4.1, open-loop transfer function between $I_{d,fb}$ and $I_{d,ref}$ is estimated as follows:

$$\begin{aligned}\frac{I_{d,fb}}{I_{d,ref}} &= \left(K_{P,I}\frac{1+sT_{i,I}}{sT_{i,I}}\right)\left(\frac{1}{1+sT_d}\right)\left(\frac{K}{1+sT}\right)\left(\frac{1}{1+sT_{f,I}}\right) \\ &\cong \left(K_{P,I}\frac{1+sT_{i,I}}{sT_{i,I}}\right)\left(\frac{1}{1+s\left(T_d+T_{f,I}\right)}\right)\left(\frac{K}{1+sT}\right)\end{aligned} \tag{4.14}$$

where $K_{P,I}$ is the current loop PI controller gain constant, $T_{i,I}$ is the current loop PI controller time constant, and $T_{f,I}$ is the current loop filter time constant.

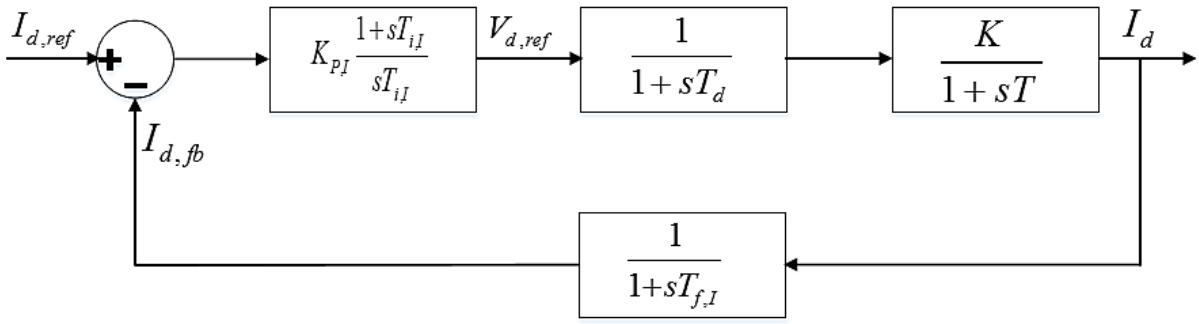

Figure 4.1: *d*-axis current control loop block diagram.

For tuning of the current PI controller, modulus optimum technique is used. According to this method, since T is much higher than $(T_d + T_{f,I})$, it can be considered as dominant pole and canceled out by controller zero while choosing $T_{i,I} = T$. Then, the closed loop transfer function is obtained as,

$$G_{cl}(s) = \frac{\frac{K_{p,I}K}{(T_d + T_{f,I})T}(1 + sT_{f,I})}{s^2 + \frac{1}{(T_d + T_{f,I})}s + \frac{K_{p,I}K}{(T_d + T_{f,I})T}} \tag{4.15}$$

$$w_n = \sqrt{\frac{K_{p,I}K}{(T_d + T_{f,I})T}} \tag{4.16}$$

$$\xi = \frac{1}{2(T_d + T_{f,I})w_n} \tag{4.17}$$

where w_n and ζ are undamped natural frequency and damping factor respectively.

By considering $\xi = \frac{1}{\sqrt{2}}$ to obtain the most efficient response of the second order transfer function (smaller overshoot and faster rise time), the controller gain is calculated as,

$$K_{p,I} = \frac{T}{2K(T_d + T_{f,I})} \tag{4.18}$$

MMC model parameters used in conventional control method are presented in Table 4.1, and resulting inner current control loop parameters are given in Table 4.2. Figure 4.2 shows MATLAB/Simulink inner current control loop implementation block diagram while a constant voltage source of 1076.4 V is connected to MMC dc-side. Inner current control loop responses

to step changes of d-axis reference current from 0.2 to 1 at t = 1 s and from 1 to 0.5 at t = 2 s is demonstrated in Figure 4.3.

Table 4.1: MMC with conventional control method implementation model parameters.

Parameters	*Value*	*Parameters*	*Value*
Fundamental Frequency	50 Hz	Arm Inductance	1.3 mH
Switching Frequency	2 KHz	Arm Resistance	0.4 Ω
Amplitude Modulation Index	0.45	SM Capacitance	6 mF
Grid Voltage	600 V	Line Inductance	0.1 H
Number of SMs in each Arm	4	Line Resistance	20 Ω

Table 4.2: Inner current control loop parameters.

Parameters	*Value*	*Parameters*	*Value*
P_{base}	4.32 kW	$T_{i,I}$	0.005
$V_{ac,base}$	490 V	T_d	0.00025
$I_{ac,base}$	5.9 A	K	4.2
$Z_{ac,base}$	83 Ω	T	0.005
$K_{p,I}$	1.1	$T_{f,I}$	0.0003

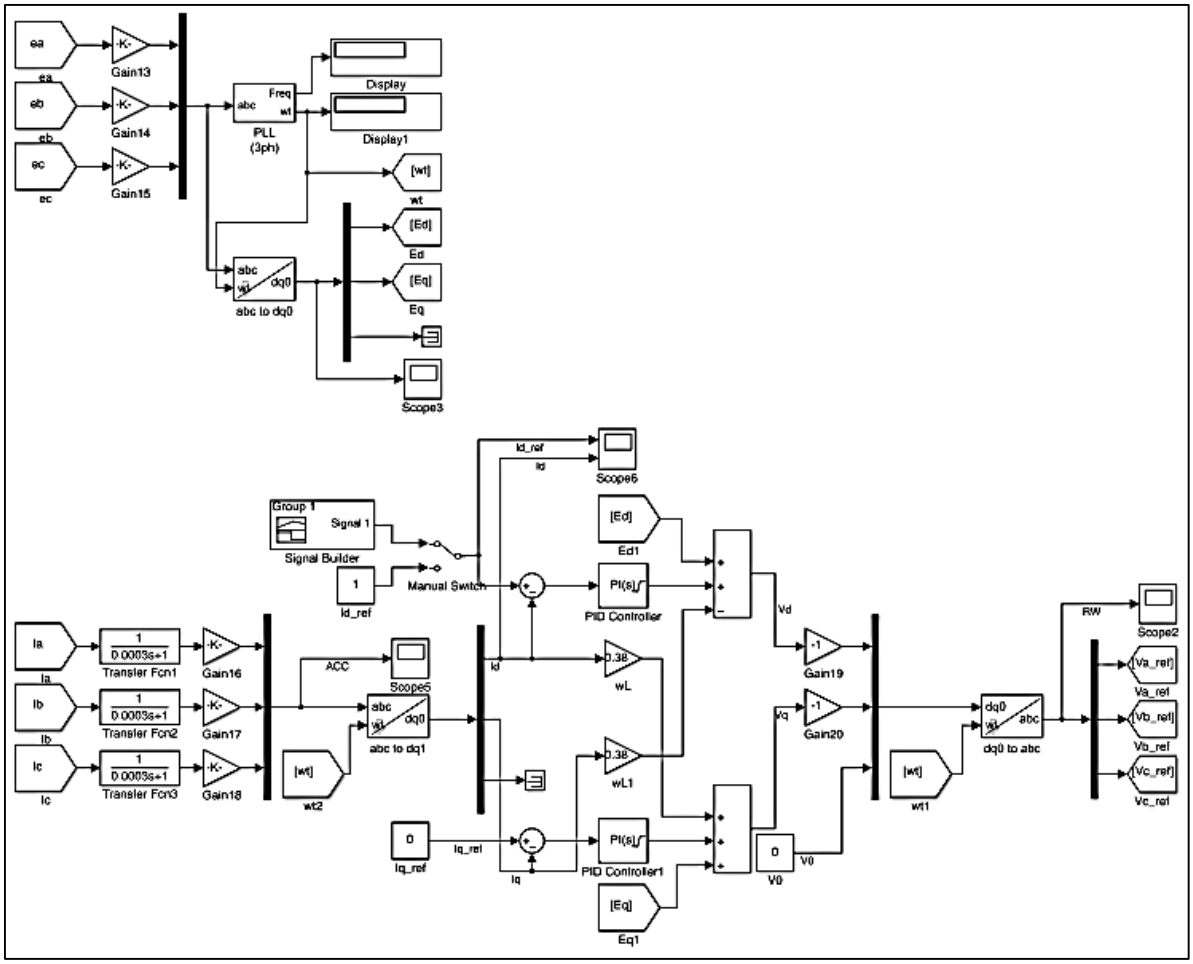

Figure 4.2: MATLAB/Simulink inner current control loop implementation block diagram.

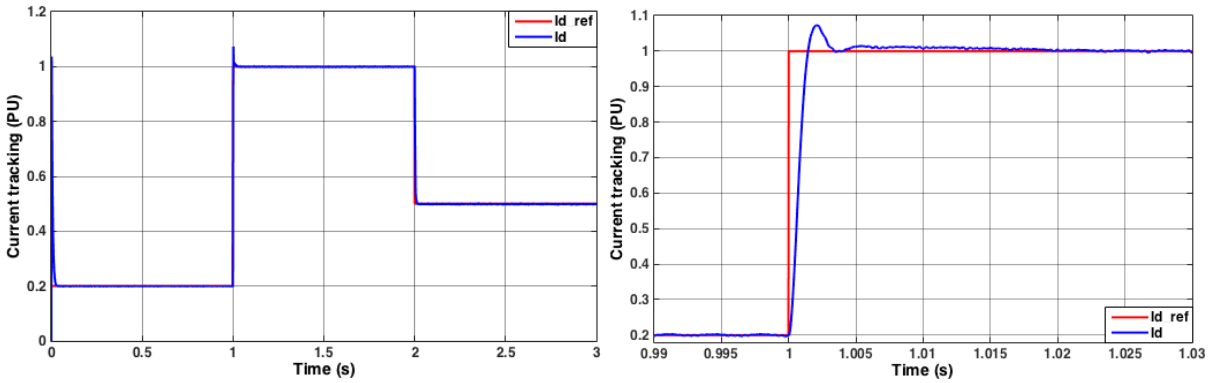

Figure 4.3:Inner current control loop responses to step changes of d-axis reference current from 0.2 to 1 at t = 1 s and from 1 to 0.5 at t = 2 s.

4.1.2 Outer Voltage Control Loop Implementation

In this section, dc voltage control loop is implemented to guarantee maximum power is transferring from PV system to the grid at any moment of time [27]-[29]. The first objective is to extract the dynamic model of the MMC on the dc-side

$$P = \frac{3}{2} V_d I_d = V_{dc} I_{dc} \tag{4.19}$$

where P is the active power, V_d and I_d are the d-axis voltage and current, and V_{dc} and I_{dc} are the dc voltage and current respectively.

Consequently,

$$I_{dc} = \frac{3}{2} \frac{V_d I_d}{V_{dc}} = C \frac{dV_{dc}}{dt} \tag{4.20}$$

where $C = 3\frac{C_{SM}}{N}$, that 3 is the number of MMC legs, and N is the number of SMs in each arm.

Laplace transform of (4.20) is,

$$\frac{3}{2} \frac{V_d I_d}{V_{dc}} = CsV_{dc} \tag{4.21}$$

Per-unitizing (4.21) leads to,

$$\frac{3}{2} \frac{V_{d,PU} V_B I_{d,PU} I_B}{V_{dc,PU} V_{dc,B}} = \frac{1}{wC_{PU} Z_{dc,B}} sV_{dc,PU} V_{dc,B} \tag{4.22}$$

Thus,

$$\frac{V_{dc,PU}}{I_{dc,PU}} = \frac{wC_{PU}}{s} \tag{4.23}$$

On the other hand, equivalent inner current control loop transfer function can be obtained by substitution of (4.18) in (4.15) as,

$$G_{cl}(s) = \frac{(1 + sT_{f,I})}{2\left(T_d + T_{f,I}\right)^2 s^2 + 2\left(T_d + T_{f,I}\right)s + 1} \tag{4.24}$$

The zero at $\frac{1}{T_{f,I}}$ can be ignored since it is at a frequency higher than the inner current control loop bandwidth. Then, the second order transfer function of (4.24) can be approximated by a first order system if the integral of the difference between the system step response and the step reference in both systems are the same.

$$G_{cl}(s)=\frac{1}{2\left(T_d+T_{f,I}\right)s+1} \tag{4.25}$$

dc voltage control loop block diagram is shown in Figure 4.4, where $K_{P,V}$ is the voltage loop PI controller gain constant, $T_{i,V}$ is the voltage loop PI controller time constant, and $T_{f,V}$ is the voltage loop filter time constant.

Therefore, open-loop transfer function between $V_{dc,fb}$ and $V_{dc,ref}$ is calculated as follows:

$$\begin{aligned}\frac{V_{dc,fb}}{V_{dc,ref}}&=\left(K_{P,\mathrm{V}}\frac{1+sT_{i,\mathrm{V}}}{sT_{i,\mathrm{V}}}\right)\left(\frac{1}{1+s2(T_d+T_{f,I})}\right)\left(\frac{V_{d,PU}}{V_{dc,PU}}\right)\left(\frac{wC_{PU}}{s}\right)\left(\frac{1}{1+sT_{f,\mathrm{V}}}\right)\\ &\cong\left(K_{P,\mathrm{v}}\frac{1+sT_{i,\mathrm{V}}}{sT_{i,\mathrm{V}}}\right)\left(\frac{1}{1+s\left(2T_d+2T_{f,I}+T_{f,V}\right)}\right)\left(\frac{V_{d,PU}}{V_{dc,PU}}\right)\left(\frac{wC_{PU}}{s}\right)\end{aligned} \tag{4.26}$$

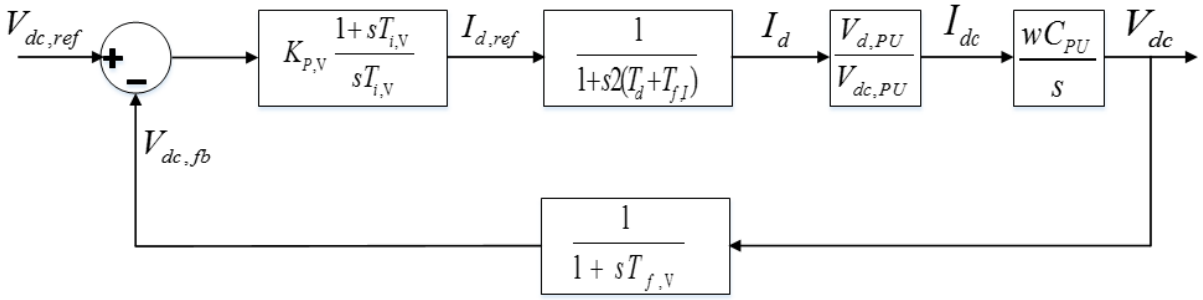

Figure 4.4: dc voltage control loop block diagram.

Symmetrical optimum method is used for tuning of the voltage PI controller. In this method, by maximizing the phase margin, system stability and disturbance rejection will be improved. Based on this method criteria, voltage PI controller parameters are,

$$T_{i,V}=a^2(2T_d+2T_{f,I}+T_{f,V}) \tag{4.27}$$

where a is the symmetrical optimum tuning parameter, and is usually chosen as a number between 2 and 4.

$$K_{p,V} = \frac{\dfrac{1}{wC_{PU}}}{a.\dfrac{V_{d,PU}}{V_{dc,PU}}.(2T_d + 2T_{f,I} + T_{f,V})} \tag{4.28}$$

Resulting outer voltage control loop parameters are presented in Table 4.3; however, further tuning of the voltage PI controller was required to improve the operation. Figure 4.5 demonstrates the overall view of control system block diagram implemented in MMC-based grid-connected PV system. $V_{dc,ref}$ originates from the MPPT system, and V_{dc} is the measured dc voltage across the MMC dc-side.

Table 4.3: Outer voltage control loop parameters.

Parameters	*Value*	*Parameters*	*Value*
$V_{dc,base}$	1076.4 V	$T_{i,V}$	0.055
$I_{dc,base}$	4.015 A	$K_{P,V}$	20.8
$Z_{dc,base}$	268.1 Ω	$T_{f,V}$	0.005
a	3		

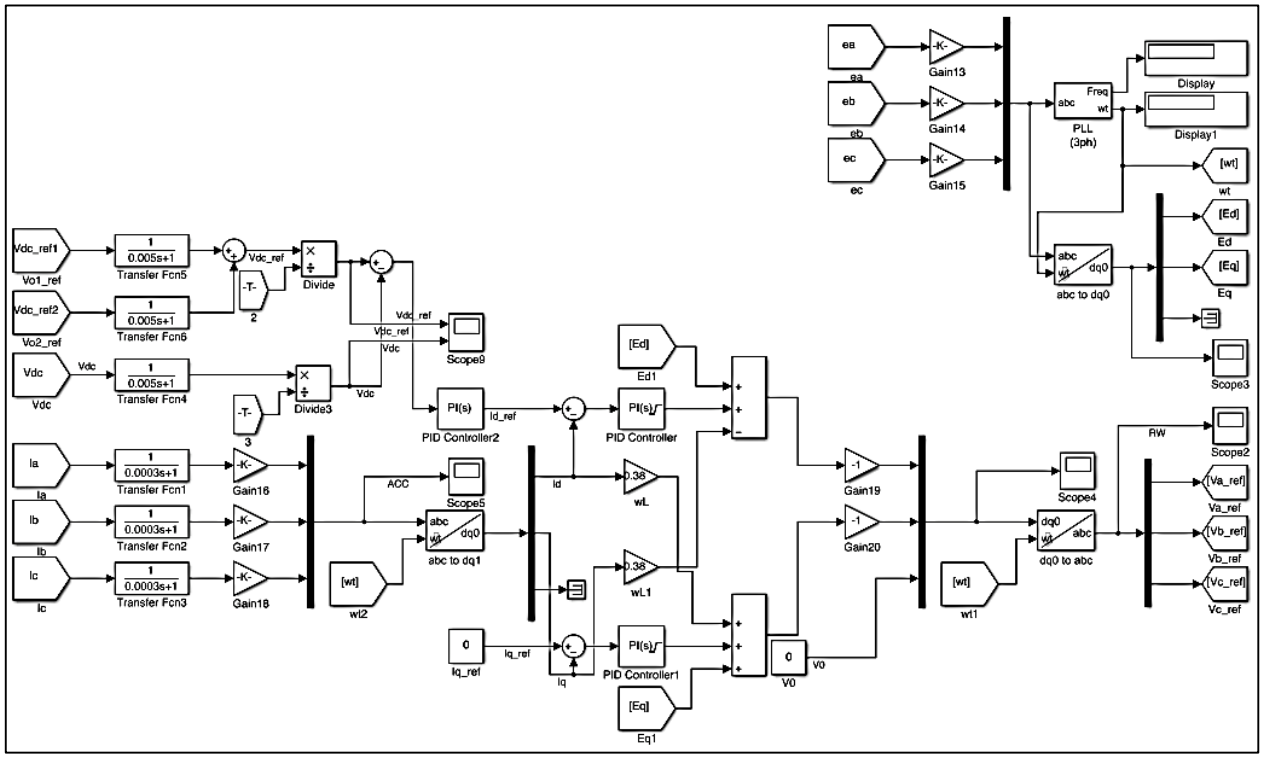

Figure 4.5: MATLAB/Simulink conventional control method implementation block diagram.

Simulation results after applying conventional control method are presented in following figures. Figure 4.6 shows how control system operates under P&O MPPT with perturbation frequency of 2HZ, step size of 0.025 V and transient time of 8 s (referring Figure 4.7). As can be seen, $I_{d,ref}$ and I_d are completely matched, whereas $V_{dc,ref}$ and V_{dc} are not perfectly coincided although V_{dc} is tracking $V_{dc,ref}$ quiet successfully. The error level between 5s and 10s is about 5%, and reduces to approximately 2% in the last 5s when the duty cycle settles in 0.575.

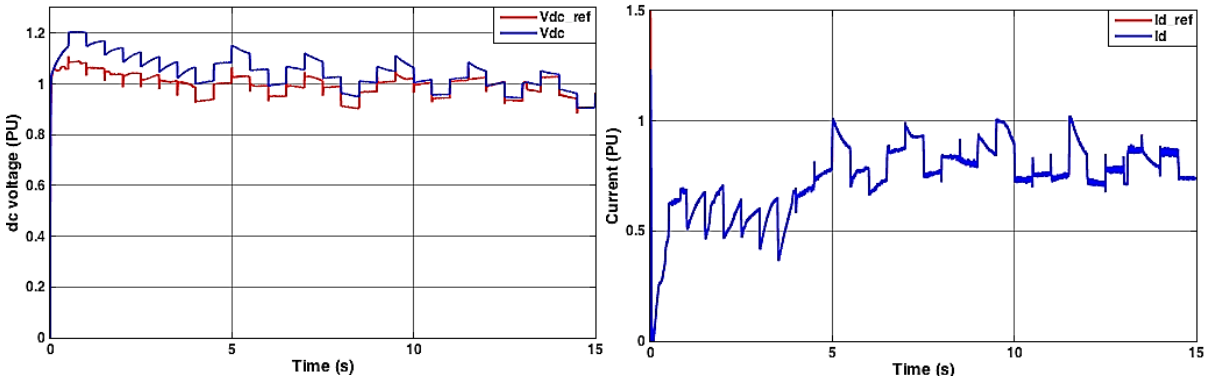

Figure 4.6: (left) $V_{dc,ref}$ and V_{dc} under P&O MPPT, (right) $I_{d,ref}$ and I_d under P&O MPPT.

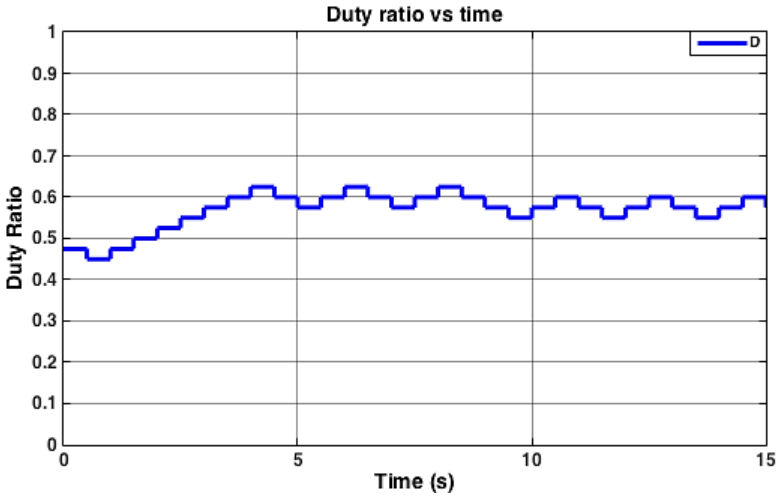

Figure 4.7: Duty cycle under STC.

Figure 4.8 demonstrates how I_{PV} and V_{PV} varies under P&O MPPT while I_{PV} fluctuates around 8.03 A and V_{PV} round 29.9 V that are the maximum power values according to the datasheet, and Figure 4.9 depicts that the current injected to the grid is in phase with the grid voltage; therefore, reactive power is zero.

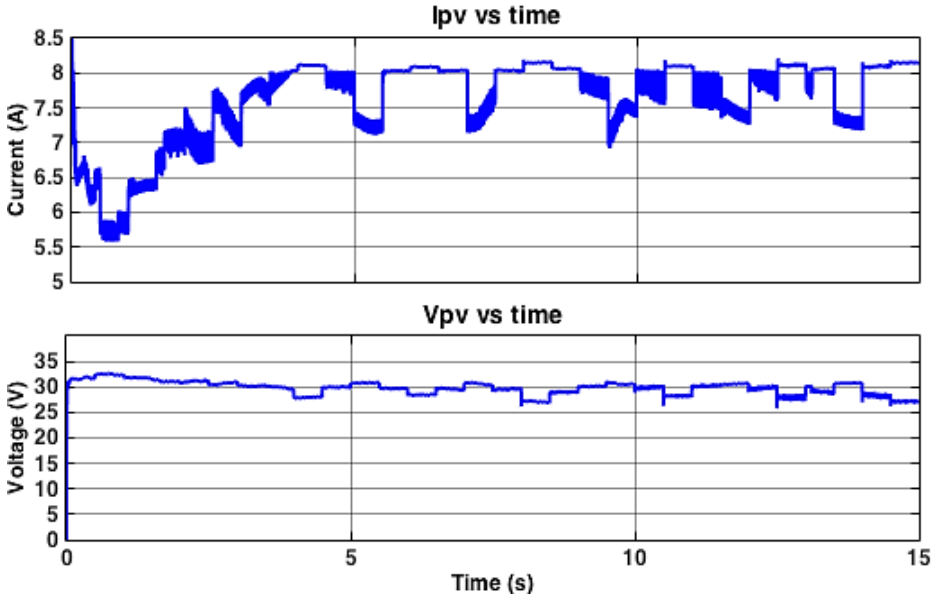

Figure 4.8: (up) I_{PV} and (down) V_{PV} under STC.

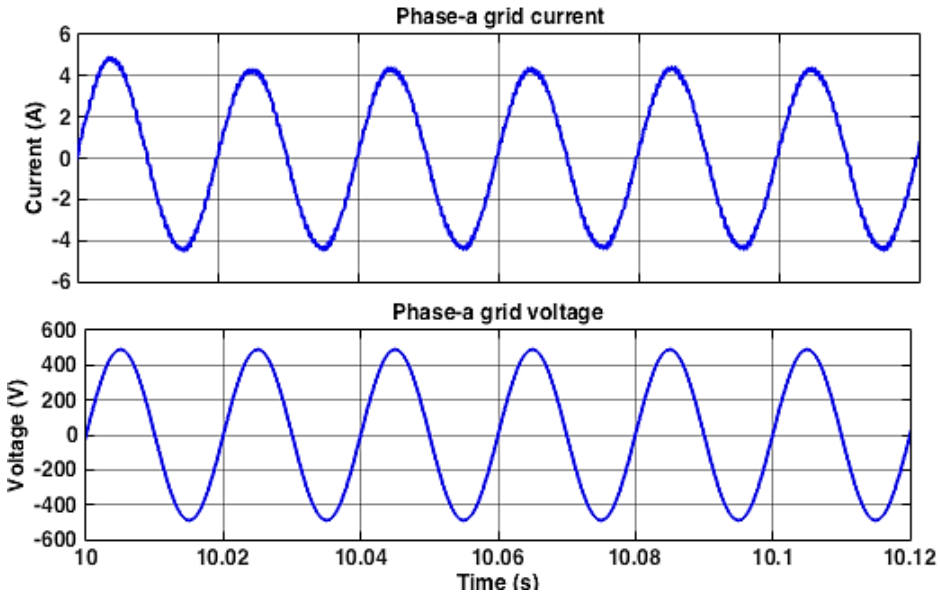

Figure 4.9: (up) Phase-a grid current, (down) Phase-a grid voltage.

Figure 4.10 shows the reference waveform and its frequency spectrum. It demonstrates reference waveform variation during the time as an input to PDPWM-SVLM. The closer view shows amplitude modulation index of 0.45 for $0 \leq m \leq 0.5$. Frequency spectrum is quite satisfying since THD level is about 1.37%.

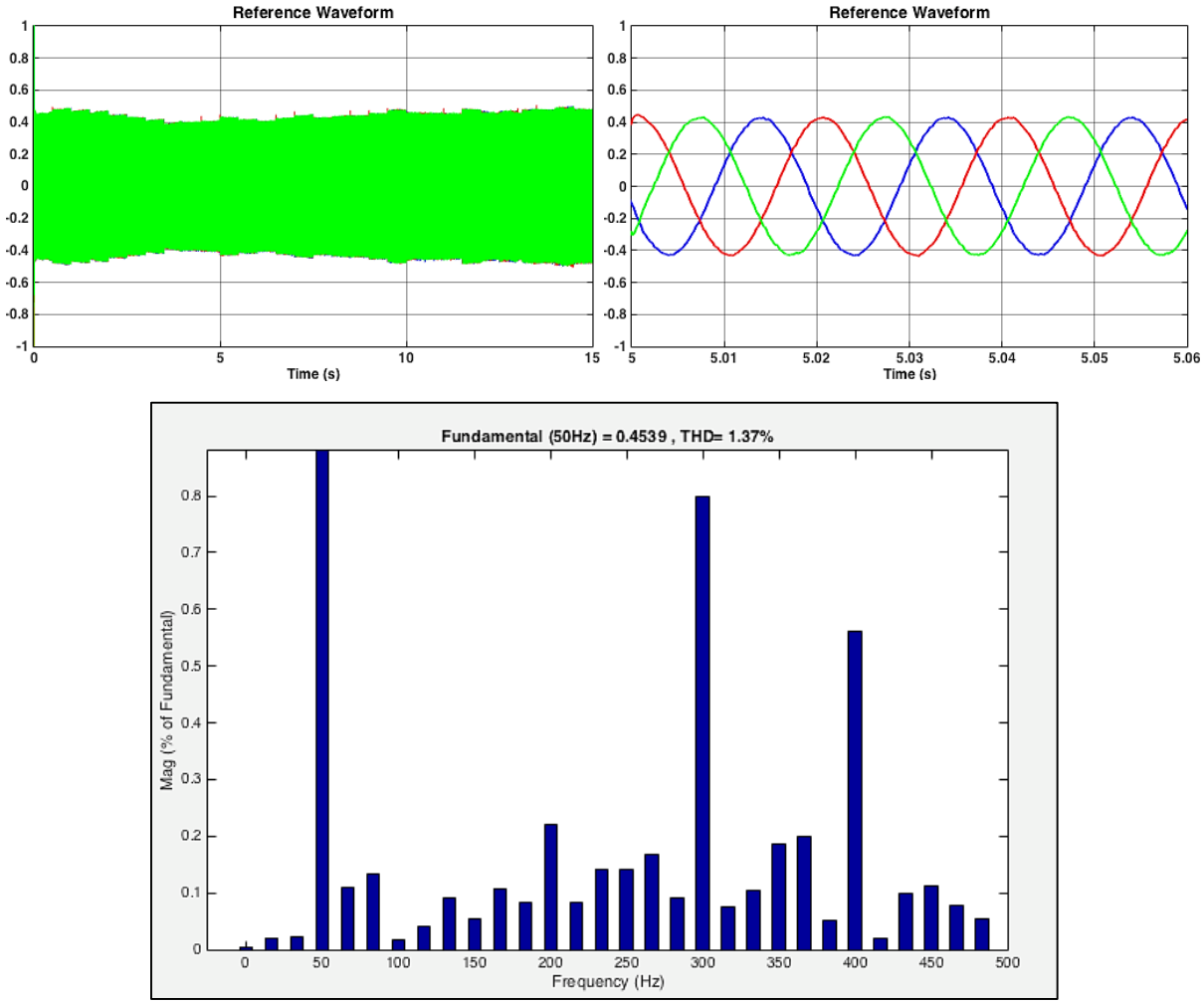

Figure 4.10: Reference waveform and its frequency spectrum.

Figure 4.11 presents the AC-side current waveform in PU and its frequency spectrum. It is apparent that the THD level is about 0.84% which is much less than the standard requested value of 5%.

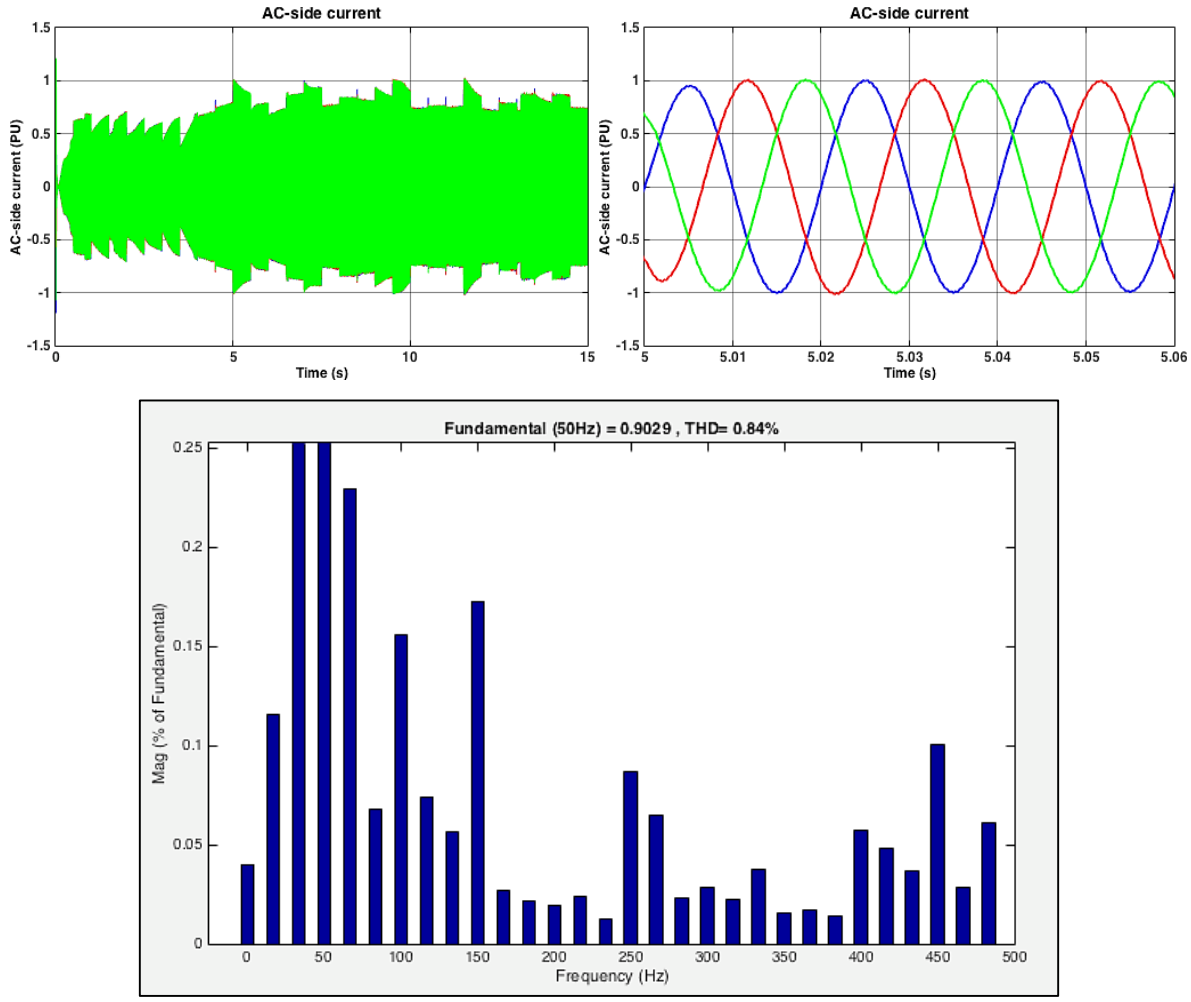

Figure 4.11: AC-side current (PU) and its frequency spectrum.

According to Figure 4.12, it can be seen that 5-level phase voltages are varying between $-V_{dc}/2$ and $V_{dc}/2$ (29.9 × 9 / (1 - 0.575) = 633.2V), and 9-level line voltages are fluctuating between $-V_{dc}$ and V_{dc} (V_{dc} = 1266.4V) based on Figure 4.13. DC-side current, AC-side currents and upper arm and lower arm currents are depicted in Figure 4.14 and Figure 4.15. Figure 4.16 shows SM capacitor voltages fluctuating around 1266.4 / 4 = 316.6 V. Upper arm SM capacitor voltages are fully coincided, while the lower arm capacitor voltages' ripple is approximately 3.2%, 1.2% and 4.7% for phase a, b and c respectively.

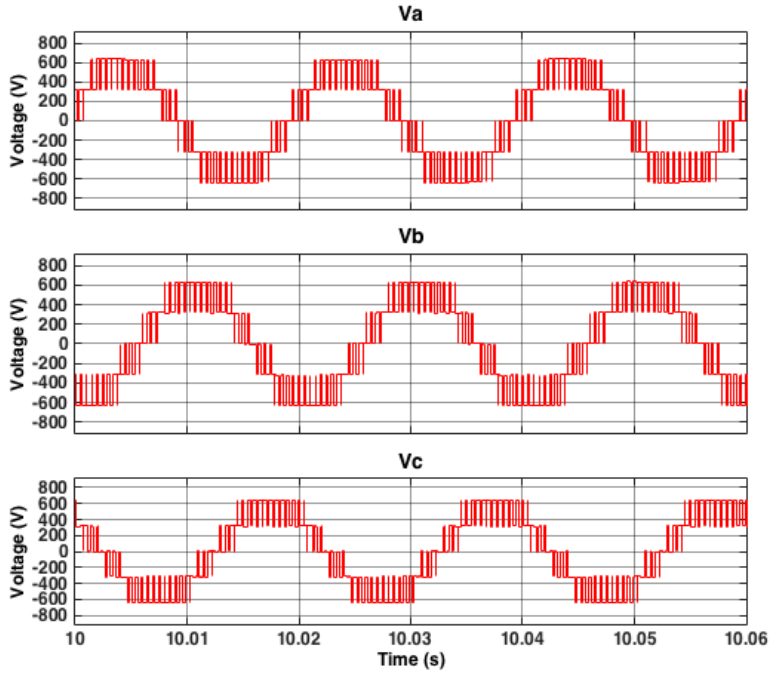

Figure 4.12: MMC AC-side phase voltages V_a, V_b, and V_c.

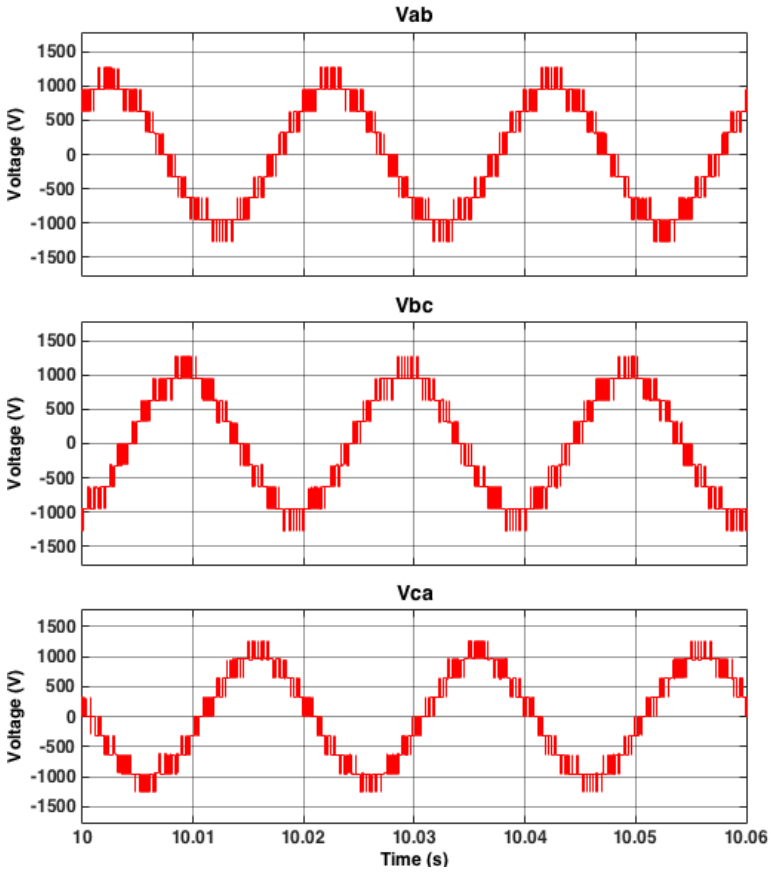

Figure 4.13: MMC AC-side line voltages V_{ab}, V_{bc}, and V_{ca}.

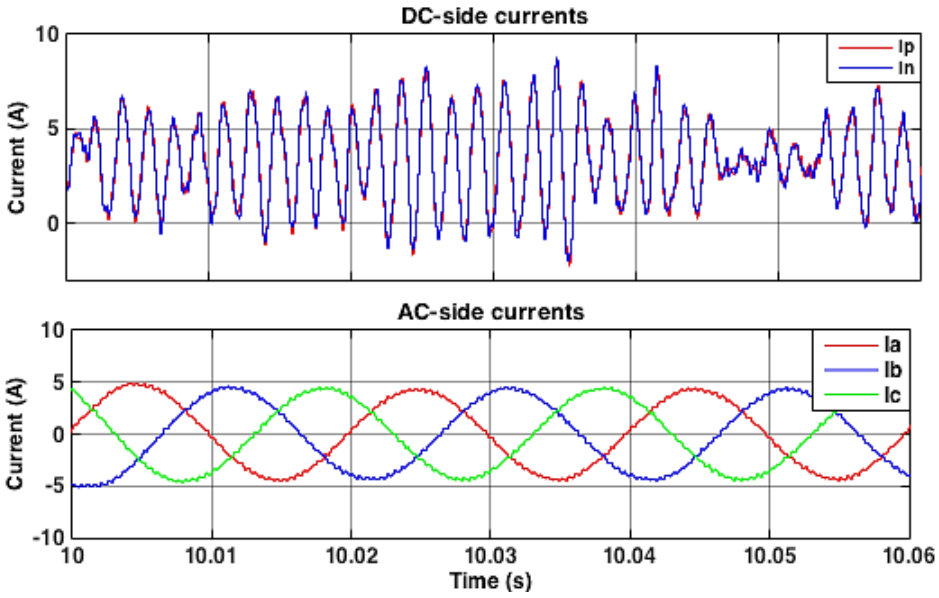

Figure 4.14: (Up) MMC DC-side currents, and (down) MMC AC-side currents.

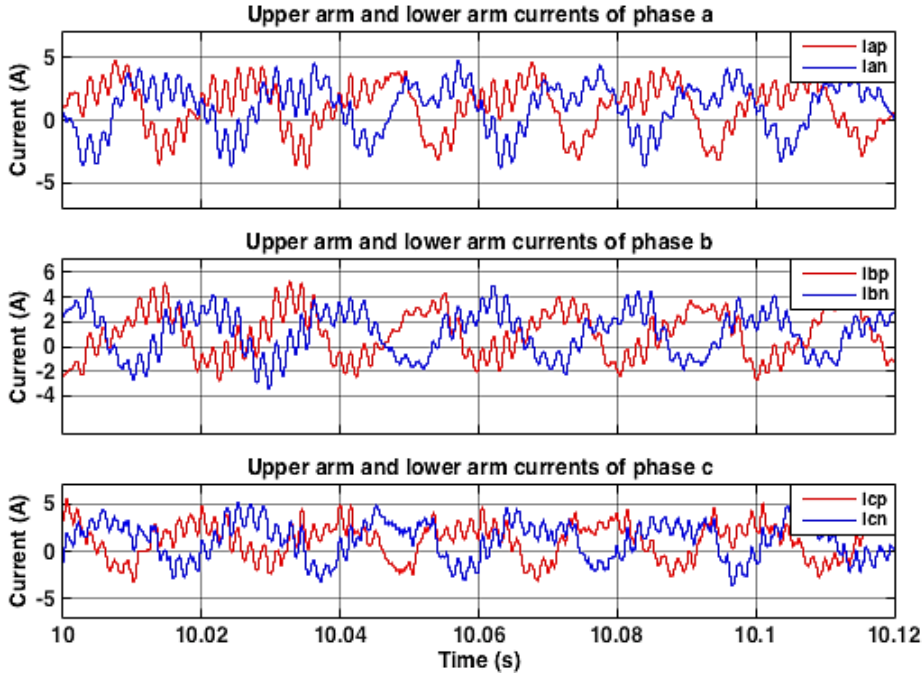

Figure 4.15: MMC upper arm and lower arm currents of the phases a, b, and c.

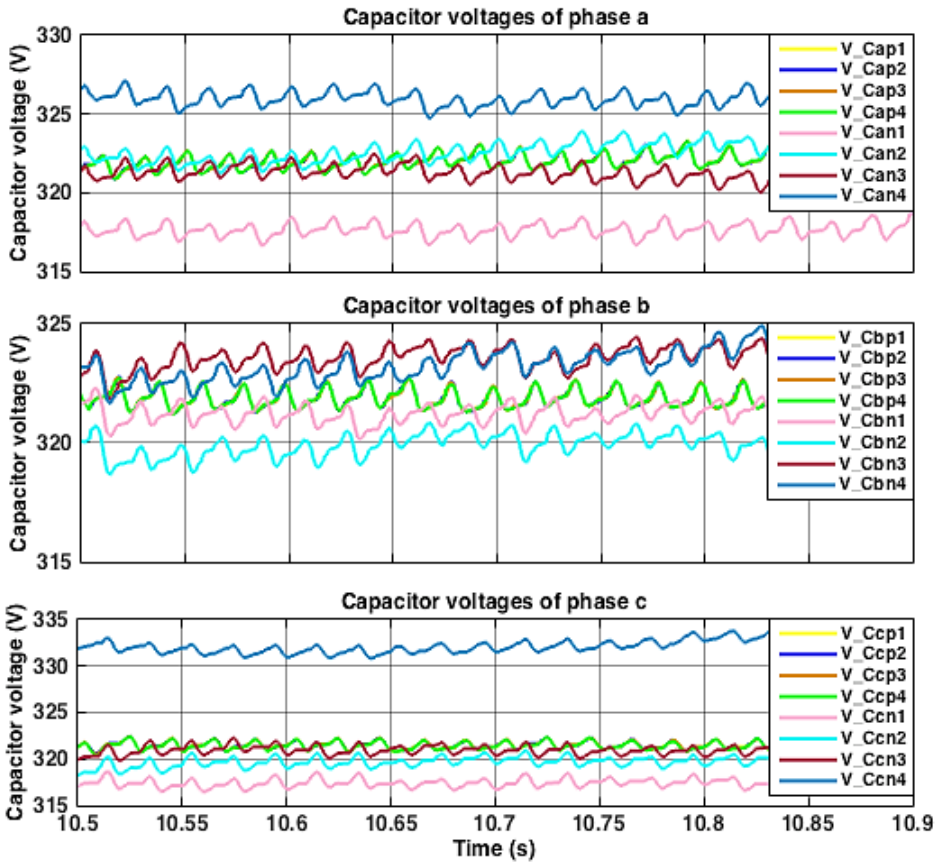

Figure 4.16: MMC upper arm and lower arm SM capacitor voltages of the phases a, b, and c.

4.2 Non-Linear Current Control Design Based on Internal Model-Based Control Method

Internal Model-Based Control (IMBC) is a control topology appropriate for tracking unknown reference trajectories or rejecting unknown disturbances; in other words, IMBC approach is more applicable when there are uncertainties regarding system parameters or reference signals [30]. By implementation of this method to control MMC current it is expected to obtain faster step response and smaller overshoot under transients, better dq-axes decoupling and higher robustness against disturbances [26].

Figure 4.17 shows IMBC block diagram where G_C(s), G_P(s) and $\tilde{G}_P(s)$ are controller, process and process model respectively. It can be seen that, $\tilde{d}(s)$ is reprehensive of mismatch between process and process model and also disturbance effect. Consequently, as a result of perfect tracking $\tilde{d}(s)$ will be equal to zero and *e(s) = r(s)* [26].

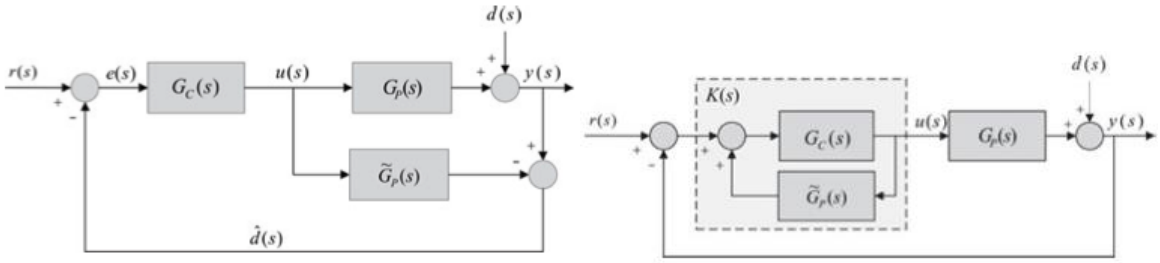

Figure 4.17: (left) IMBC block diagram, (right) IMBC equivalent block diagram [26].

Thus according to [26]:

$$u(s) = (r(s) - d(s)) \frac{G_C(s)}{1 + (G_P(s) - \tilde{G}_P(s)) G_C(s)} \tag{4.29}$$

$$y(s) = G_P(s) u(s) + d(s) \tag{4.30}$$

Then by substitution of (4.29) into (4.30),

$$y(s) = \frac{G_C(s) G_P(s)}{1 + (G_P(s) - \tilde{G}_P(s)) G_C(s)} r(s) + \frac{1 - G_C(s) \tilde{G}_P(s)}{1 + (G_P(s) - \tilde{G}_P(s)) G_C(s)} d(s) \tag{4.31}$$

To achieve perfect tracking (*y(s) = r(s)*) and disturbance rejection (*d(s)* = 0) it is required that,

$$G_P(s) = \tilde{G}_P(s) \,\&\, G_C(s) = G_P^{-1}(s) \tag{4.32}$$

The process model transfer function can be expressed as product of invertible ($\tilde{G}_P^-(s)$) and non-invertible ($\tilde{G}_P^+(s)$) components where the non-invertible component containing right half-plane zeros and system delays can be ignored such that,

$$\tilde{G}_P(s) = \tilde{G}_P^-(s)\tilde{G}_P^+(s) \simeq \tilde{G}_P^-(s) \tag{4.33}$$

To improve controller robustness, it can be multiplied to a low pass filter as below,

$$G_C(s) = \tilde{G}_P^-(s)^{-1} \frac{1}{(1+\lambda s)^n} \tag{4.34}$$

where λ and *n* are the filter parameter and filter order respectively.

Considering equation (4.5), after Laplace transform and per-unitization, system transfer function can be written as,

$$G_s(s) = \frac{I_{l,dq,PU}}{V_{c,dq,PU} - V_{g,dq,PU}} = \frac{1}{R_{PU} + jw\frac{L_{PU}}{w_B} + s\frac{L_{PU}}{w_B}} = \frac{\frac{1}{R_{PU}}}{1+(jw+s)\frac{L_{PU}}{w_B R_{PU}}} = \frac{K}{1+(jw+s)T} \tag{4.35}$$

Similarly, PWM transfer function is,

$$G_{PWM}(s) = \frac{1}{1+(jw+s)\frac{1}{2f_s}} = \frac{1}{1+(jw+s)T_d} \tag{4.36}$$

Then, process model becomes,

$$\begin{aligned} \tilde{G}_P &= \left(\frac{1}{1+(jw+s)T_d}\right)\left(\frac{K}{1+(jw+s)T}\right)\left(\frac{1}{1+(jw+s)T_{f,I}}\right) \\ &\cong \left(\frac{1}{1+(jw+s)\left(T_d+T_{f,I}\right)}\right)\left(\frac{K}{1+(jw+s)T}\right) \end{aligned} \tag{4.37}$$

Hence,

$$G_C(s) = \frac{(1+(jw+s)\left(T_d + T_{f,I}\right))(1+(jw+s)T)}{K(1+\lambda \mathrm{s})} \tag{4.38}$$

Finally,

$$K(s) = \frac{G_C(s)}{1-G_C(s)\tilde{G_P}(s)} = \frac{(1+(jw+s)\left(T_d + T_{f,I}\right))(1+(jw+s)T)}{K\lambda \mathrm{s}} \tag{4.39}$$

K(s) can be simplified into [26],

$$\begin{aligned} K(s) &= K_{PID}(s) + jK_{PI}(s) \\ &= K_p \frac{\tau_I \tau_D s^2 + \tau_I s + 1}{\tau_I s} + jK_P^{'} \frac{\tau_I^{'} s + 1}{\tau_I^{'} s} \end{aligned} \tag{4.40}$$

where,

$$\begin{aligned} K_P &= \frac{T_d + T_{f,I} + T}{K\lambda} \\ \tau_I &= \frac{T_d + T_{f,I} + T}{1 - w^2(T_d + T_{f,I})T} \\ \tau_D &= \frac{(T_d + T_{f,I})T}{T_d + T_{f,I} + T} \\ K_P^{'} &= \frac{2w(T_d + T_{f,I})T}{K\lambda} \\ \tau_I^{'} &= \frac{2(T_d + T_{f,I})T}{w(T_d + T_{f,I} + T)} \end{aligned} \tag{4.41}$$

IMBC current control system parameters and block diagram are presented in Table 4.4 and Figure 4.18. As can be seen the equivalent controller transfer function is complex and it is composed of a PID controller and a PI controller where the error between reference current and measured current are fed into the same axis via the PID controller and the opposite axis via the PI controller. For dc-voltage control the same method as conventional control technique is used.

Figures 4.19 to Figure 4.28 shows IMBC method simulation results. Results are almost compatible with expectation and results obtained from conventional control method. However, reference waveform quality is still low with high THD level even though a low pass filter is inserted in the control loop feedback. So further modifications are required to fix the problem since this has effected the ac-side voltages and currents consecutively.

Table 4.4: IMBC current control system parameters.

Parameters	*Value*	*Parameters*	*Value*
P_{base}	4.32 kW	T_d	0.00025
$V_{ac,base}$	490 V	$K_{f,I}$	0.00159
$I_{ac,base}$	5.9 A	μ	0.0001
$Z_{ac,base}$	83 Ω	K_P	16.5
f	50 Hz	τ_I	0.075
f_s	2000 Hz	τ_D	0.0013
w	314.2 rad/s	P	16.5
R	20 Ω	I	221
L	0.1 H	D	0.0222
R_{PU}	0.24	K'_P	13.9
L_{PU}	0.38	τ'_I	8.58e-6
K	4.15	P'	13.9
T	0.0005	I'	1.63e6

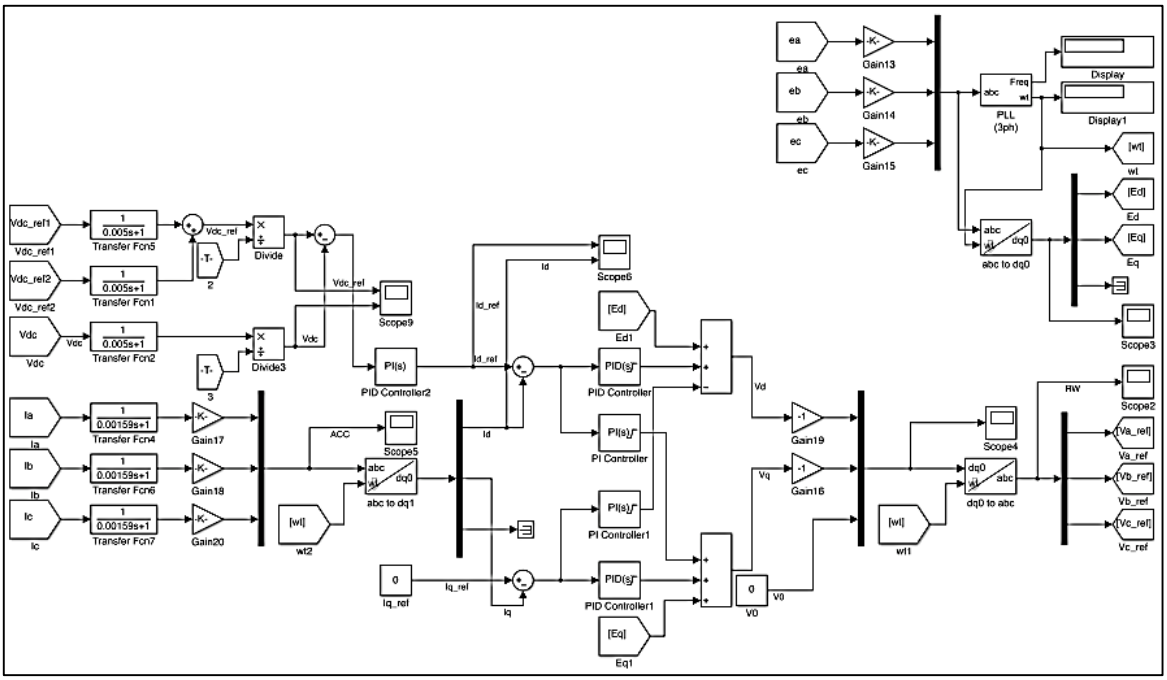

Figure 4.18: IMBC current control system block diagram.

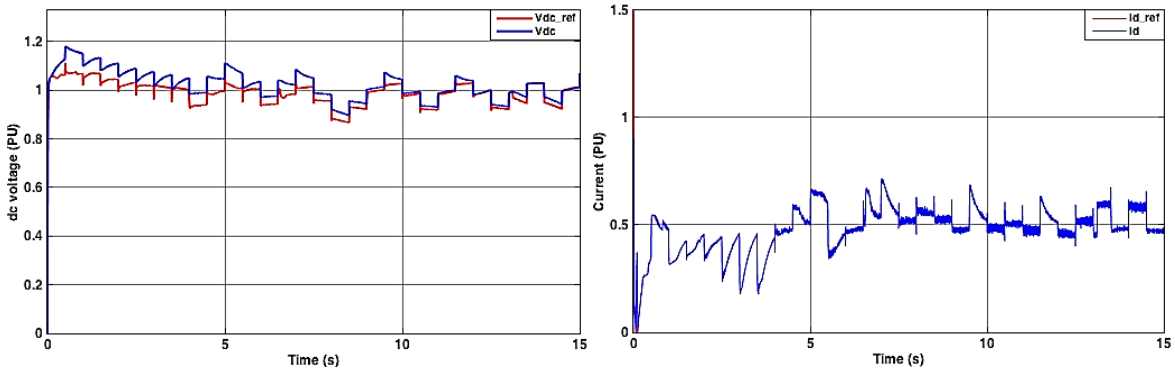

Figure 4.19: IMBC method: (left) $V_{dc,ref}$ and V_{dc} under P&O MPPT, (right) $I_{d,ref}$ and I_d under P&O MPPT.

Figure 4.20: IMBC method: duty cycle under STC.

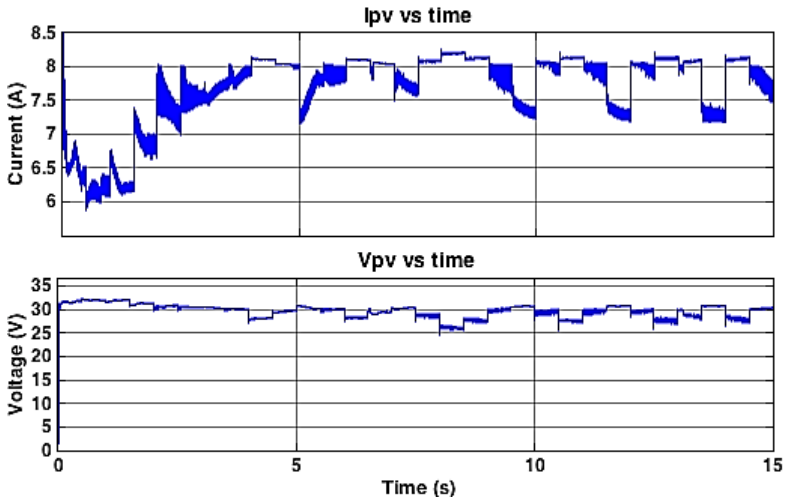

Figure 4.21: IMBC method: (up) I_{PV} and (down) V_{PV} under STC.

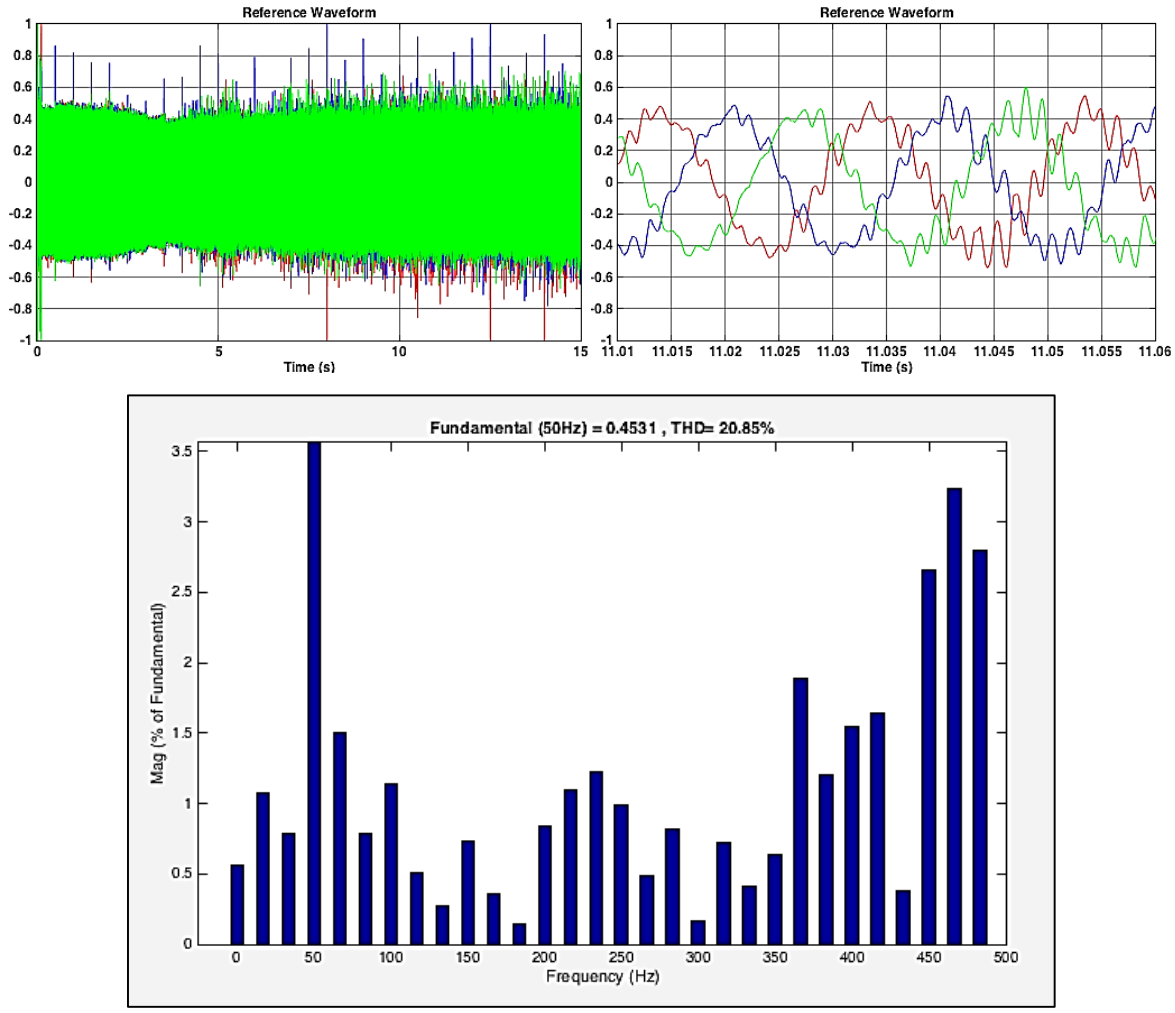

Figure 4.22: IMBC method: Reference waveform and its frequency spectrum.

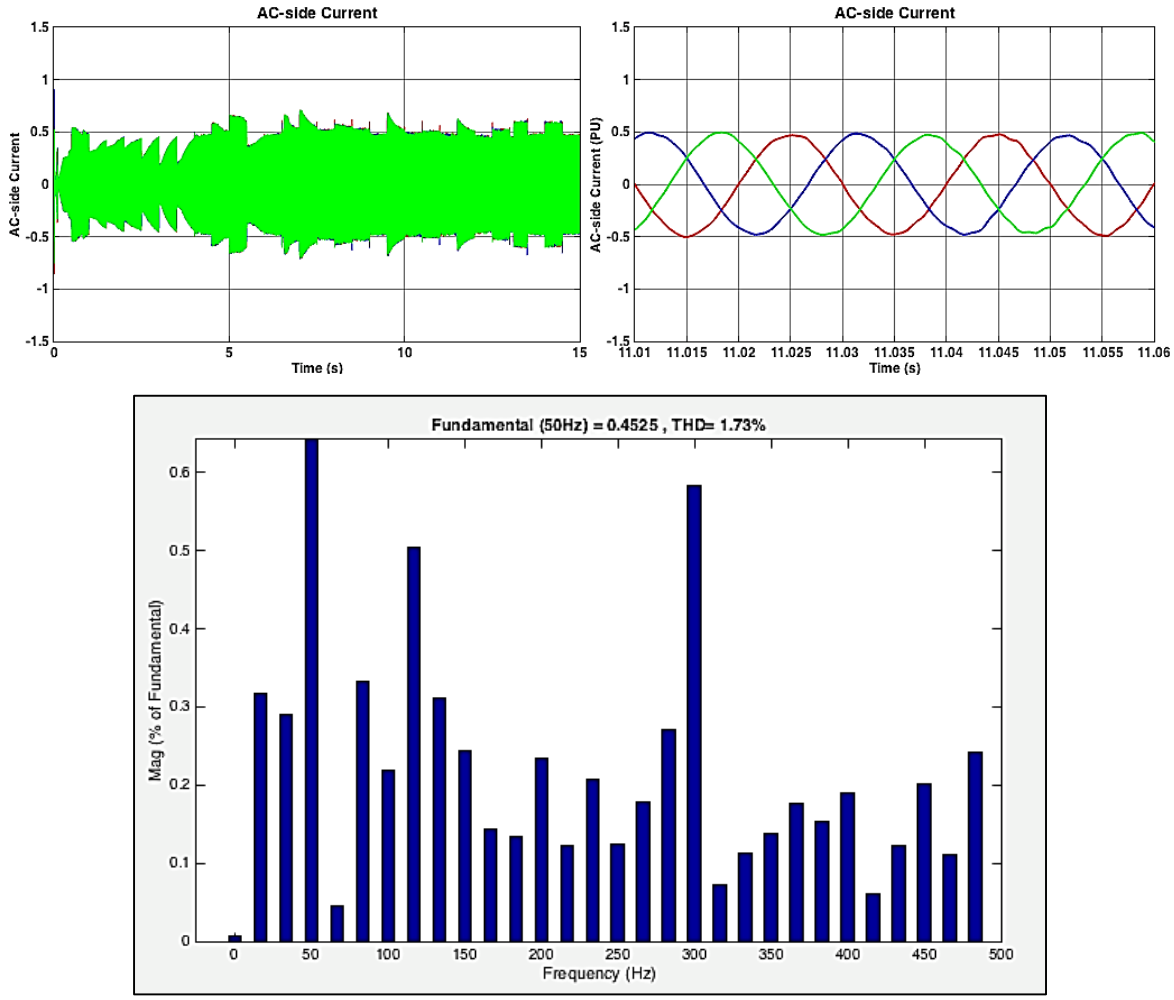

Figure 4.23: IMBC method: AC-side current (PU) and its frequency spectrum.

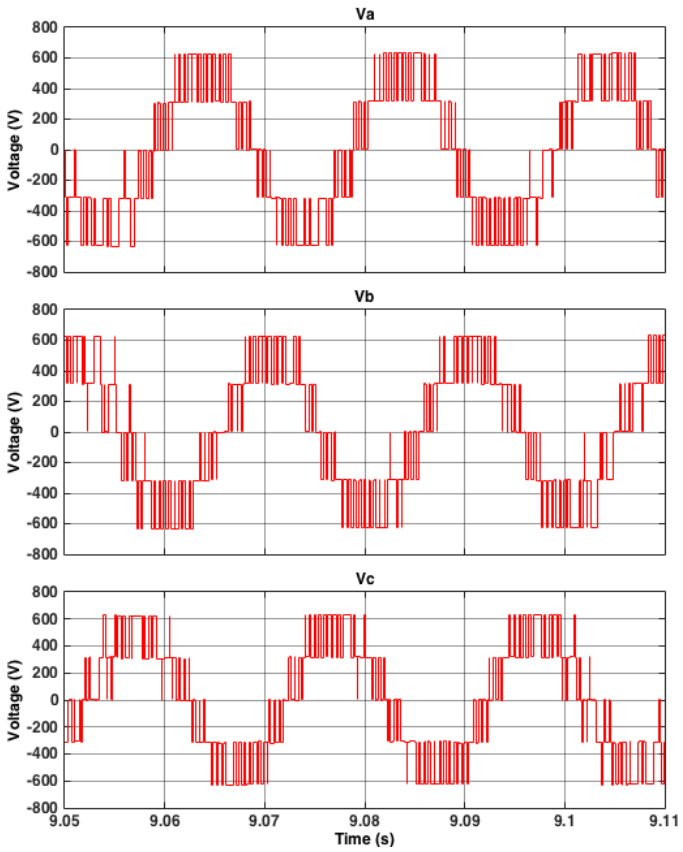

Figure 4.24: IMBC method: MMC AC-side phase voltages V_a, V_b, and V_c.

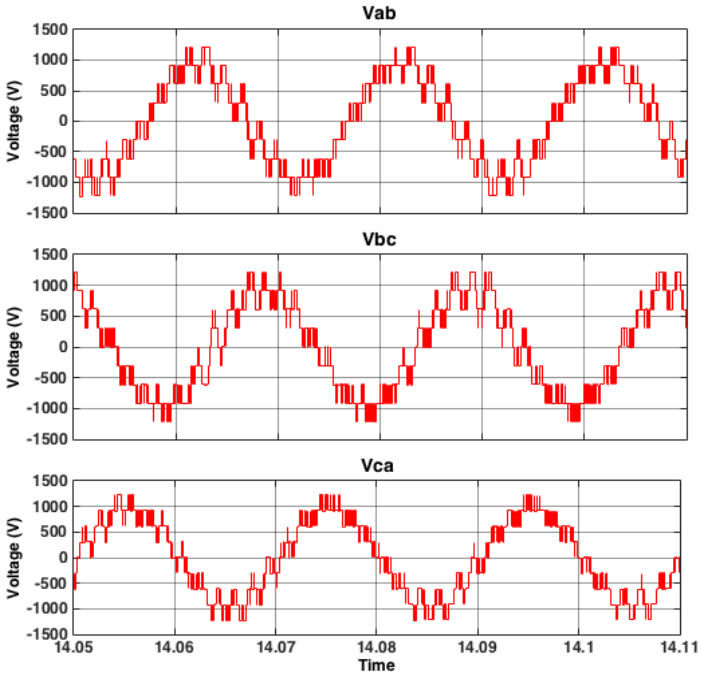

Figure 4.25: IMBC method: MMC AC-side line voltages V_{ab}, V_{bc}, and V_{ca}.

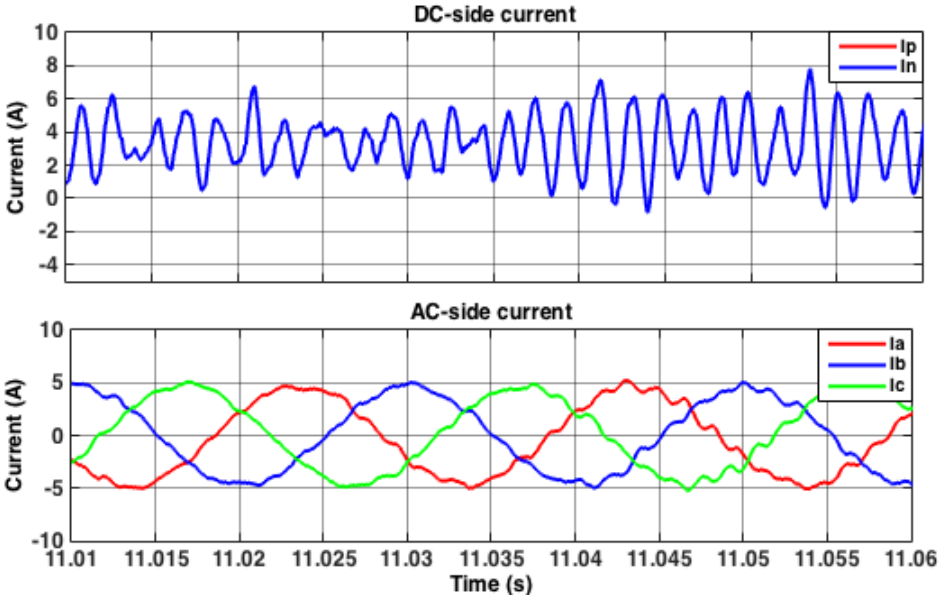

Figure 4.26: IMBC method: (Up) MMC DC-side currents, and (down) MMC AC-side currents.

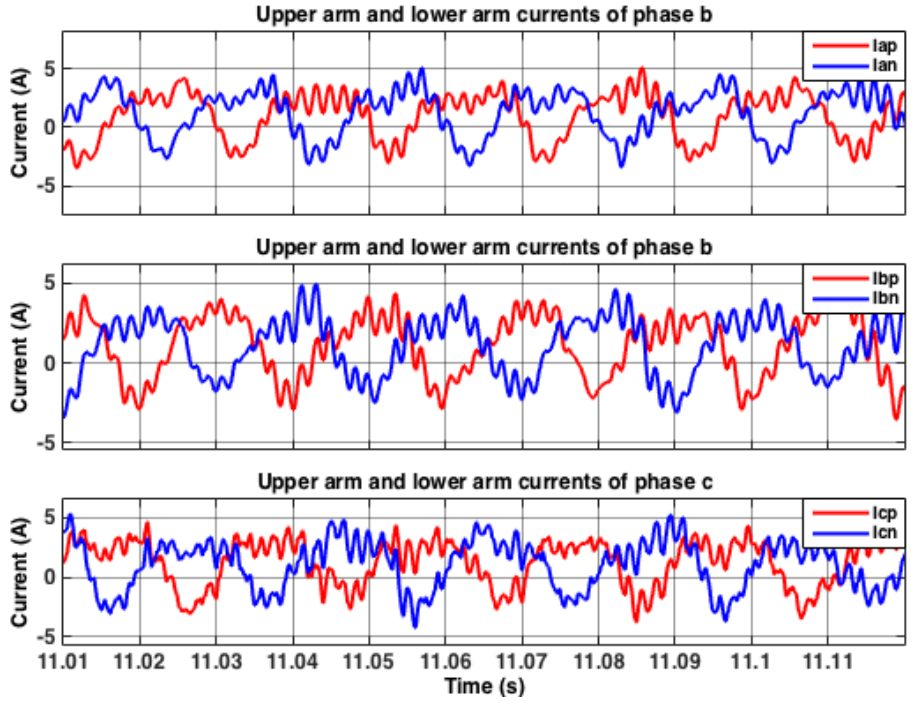

Figure 4.27: IMBC method: MMC upper arm and lower arm currents of the phases a, b, and c.

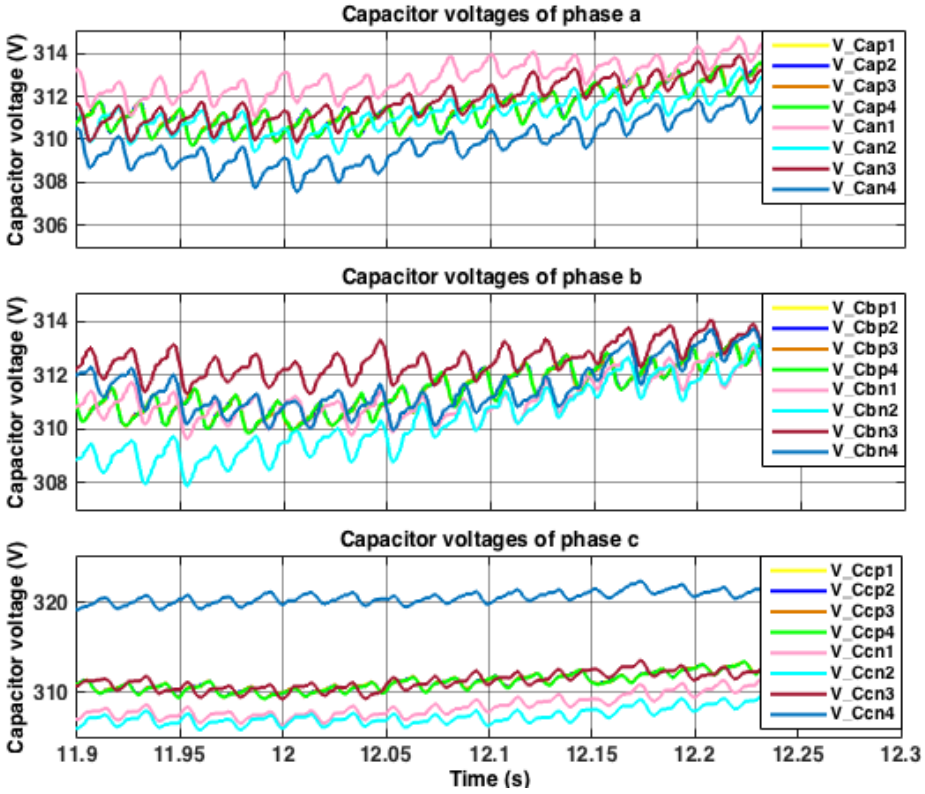

Figure 4.28: IMBC method: MMC upper arm and lower arm SM capacitor voltages of the phases a, b, and c.

To examine dynamic performance of the system under irradiance fluctuations, it is worth mentioning no matter how large irradiance variations are. Since the system is operating under P&O MPPT technique, it will converge to the new MPP with transients as large as step sizes within the defined transient time.

Chapter 5

5 Conclusions

There is no doubt in decisive role of the grid-connected PV power plants in global future energy network; besides, significance of MMCs as inverter and controller cannot be overlooked. The scope of this master thesis is to investigate and study the "Application of Modular Multilevel Inverter for Interfacing Grid-Connected Photovoltaic Conversion Plants."

5.1 Discussions

In chapter 2, after introducing PV system characteristics and mathematical model, a flexible and robust solar cell model appropriate for dynamic and transient studies especially in grid-connected applications is presented. Then, due to the intermittent nature of the solar cells under various irradiances and temperatures, two different MPPT methods are implemented to the PV system. The first one is the simple, flexible and robust method of P&O. Direct duty ratio perturbation is favored to reference voltage perturbation because of its higher system stability and better energy utilization. Besides, a practical technique for choosing P&O perturbation frequency and step size based on a selected MPPT transient time is introduced. However, one major drawback of P&O MPPT is the existence of an intrinsic tradeoff between the steady state error and convergence speed. The second MPPT technology, RCC MPPT, overcomes this deficiency by reducing the steady state error and accelerating the convergence time.

In chapter 3, MMC topology, operating principle and its mathematical model are introduced. Some of the remarkable characteristics of MMCs are high availability, modularity, redundancy, scalability, and fail safe operation. Besides, MMCs provide high energy efficiency and low losses due to relatively low switching frequency and low THD owing to multilevel features. Simulation results under P&O and RCC MPPT for a PV system composed of two PV arrays that is connected to the grid via a four-level MMC with PSPWM are presented. Moreover, SM capacitor voltage balancing is implemented in a five-level MMC via PDPWM based on SVLM. Not only this method has good dynamic performance under transients, but also it is suitable for MMCs with a large number of SMs since it only demands for min and max capacitor voltages instead of sorting algorithm that is really time consuming. Simulation results for upper arm capacitor voltages are quite satisfactory, and it can be seen that they are fully coincided.

In chapter 4, the main concentration is to implement a control strategy for MMC-based grid-connected PV system. The conventional control method based on modulus optimum technique

for tuning of inner current control loop, and symmetrical optimum technique for tuning of outer dc-voltage control loop is selected. According to the simulation results it is apparent that the three phase AC-current injected to the grid is well balanced and it is in phase with the grid voltage; furthermore, total harmonic distortion of the current is so low (less than 1%) that it is an indication of high quality current. The PV system is capable of operation at its maximum power point under dynamics and transients, and SM capacitor voltages are also able to follow these variations accordingly. SM capacitor voltage balancing operation has improved under AC-side balanced current, and not only upper arm capacitor voltages are balanced and coincided but also lower arm capacitor voltage ripple is reduced and is within the acceptable margin. System is capable of following dynamics imposed by the three level operation of the P&O MPPT. Finally, the nonlinear current control method of IMBC is presented which still requires further modifications to improve reference waveform quality.

5.2 Future Work

The MMC-based grid-connected PV model presented in this thesis can be further studied as follows:

- Designing a filter to suppress circulating current second harmonics that are responsible for switching losses.
- The possibility and impact of using wide-band-gap SiC-based devices instead of silicon IGBT/MOSFET switches to reduce losses and improve efficiency.
- Improvement of reference waveform quality in the IMBC method.
- Analyzing the proposed model under different balanced and unbalanced faults.
- Implementation of the proposed model in a small scale prototype.

References

[1] Renewables 2014, Global Status Report, REN21, Renewable Energy Policy Network for the 21st Century.

[2] A. Elahidoost, "Application of Modular Multilevel Inverter for Interfacing Grid-Connected Photovoltaic Conversion Plants," Specialization Project at Norwegian University of Science and Technology (NTNU), 2015.

[3] Energy - Euripean Commission, [Online]. Available: https://ec.europa.eu/energy/

[4] A. Keyhani, "Design of Smart Power Grid Renewable Energy Systems," Hoboken: Wiley, 2011. Ebook Library. Web. 04 Sep. 2015.

[5] S. Rajasekar, R. Gupta, "Solar Photovoltaic Power Conversion Using Modular Multilevel Converter," *in Engineering and Systems (SCES), 2012 Students Conference on,* vol., no., pp.1-6, 16-18 March 2012.

[6] [Online]. Available: http://www.pveducation.org/pvcdrom/solar-cell-operation

[7] M.A. Eltawil, Z. Zhao, "Grid-Connected Photovoltaic Power Systems: Technical and Potential Problems - A Review," *Renewable and Sustainable Energy Reviews* 14 (2010) 112–129.

[8] R.C. Campbell, "A Circuit-Based Photovoltaic Array Model for Power System Studies," *in Power Symposium, 2007. NAPS '07. 39th North American,* vol., no., pp.97-101, Sept. 30 2007-Oct. 2 2007.

[9] Canadian Solar, CS6P-240P Datasheet, [Online]. Available: www.canadiansolar.com

[10] A. Barchowsky, "Design and Testing of High Frequency Converters for Photovoltaic System Integration," M.Sc. Thesis at University of Pittsburgh, 2014.

[11] T. Esram, J.W. Kimball, P.T. Krein, P.L. Chapman, P. Midya, "Dynamic Maximum Power Point Tracking of Photovoltaic Arrays Using Ripple Correlation Control," *in Power Electronics, IEEE Transactions on,* vol.21, no.5, pp.1282-1291, Sept. 2006.

[12] S. Rajasekar, R. Gupta, "Solar Photovoltaic Power Conversion Using Modular Multilevel Converter," *in Engineering and Systems (SCES), 2012 Students Conference on,* vol., no., pp.1-

6, 16-18 March 2012.

[13] M.A. Elgendy, B. Zahawi, D.J. Atkinson, "Assessment of Perturb and Observe MPPT Algorithm Implementation Techniques for PV Pumping Applications," *in Sustainable Energy, IEEE Transactions on*, vol.3, no.1, pp.21-33, Jan. 2012.

[14] P.T. Krein, "Ripple Correlation Control, with Some Applications," *in Circuits and Systems, 1999. ISCAS '99. Proceedings of the 1999 IEEE International Symposium on*, vol.5, no., pp.283-286 vol.5, 1999.

[15] N. Mohan, T.M. Undeland, W.P. Robbins, "Power Electronics, Converters, Applications, and Design" Third Edition, 2003 John Wiley & Sons, Inc.

[16] A. Lesnicar, R. Marquardt, "An Innovative Modular Multilevel Converter Topology Suitable for a Wide Power Range," *Power Tech Conference Proceedings, 2003 IEEE Bologna*, vol.3, no.6, pp. 23-26, June 2003.

[17] S. Debnath, J. Qin, B. Bahrani, M. Saeedifard, and P. Barbosa, "Operation, Control, and Applications of the Modular Multilevel Converter: A Review," *Power Electronics, IEEE Transactions on*, vol.30, no.1, pp. 37-53, Jan. 2015.

[18] S. Allebrod, R. Hamerski, and R. Marquardt, "New Transformerless, Scalable Modular Multilevel Converters for HVDC-Transmission," *Power Electronics Specialists Conference, 2008. PESC 2008. IEEE*, pp. 174-179, June 2008.

[19] M.A. Perez, S. Bernet, J. Rodriguez, S. Kouro, and R. Lizana, "Circuit Topologies, Modeling, Control Schemes, and Applications of Modular Multilevel Converters," *Power Electronics, IEEE Transactions on*, vol.30, no.1, pp. 4-17, Jan. 2015.

[20] H. Nademi, "Advanced Control of Power Converters: Modular Multilevel Converter," Doctoral Thesis at NTNU, 2014.

[21] M. Alsadah, F. Mancilla-David, "Modeling and Control of Grid-Connected Photovoltaic Power Plants Utilizing a Simplified Model of the Modular Multilevel Converter," *in North American Power Symposium (NAPS), 2014*, vol., no., pp.1-6, 7-9 Sept. 2014.

[22] M.S. Rajan, R. Seyezhai, "Comparative Study of Multicarrier PWM Techniques for a Modular Multilevel Inverter," *International Journal of Engineering & Technology (0975-4024)*, Dec 2013/Jan 2014, Vol. 5, Issue 6, p4850.

[23] A. Das, H. Nademi, L. Norum, "A Method for Charging and Discharging Capacitors in Modular Multilevel Converter," *in IECON 2011 - 37th Annual Conference on IEEE Industrial Electronics Society*, vol., no., pp.1058-1062, 7-10 Nov. 2011.

[24] R. Nejati Fard, "Finite Control Set Model Predictive Control in Power Converters," M.Sc. Thesis at NTNU, 2013.

[25] J. Mei, B. Xiao, K. Shen, L.M. Tolbert, J.Y. Zheng, "Modular Multilevel Inverter with New Modulation Method and Its Application to Photovoltaic Grid-Connected Generator," *in Power Electronics, IEEE Transactions on,* vol.28, no.11, pp.5063-5073, Nov. 2013.

[26] M.Yazdanian, A.Mehrizi-Sani , "Internal Model-Based Current Control of the RL Filter-Based Voltage-Sourced Converter," *in Energy Conversion, IEEE Transactions on,* vol. 29, no. 4, pp. 873-881, Dec. 2014.

[27] J. Prasad, T. Bhavsar, R. Ghosh, G. Narayanan, "Vector Control of Three-Phase AC/DC Front-End Converter," Sadhana, October 2008, Volume 33, Issue 5, pp 591-613.

[28] C. Bajracharya, "Control of VSC-HVDC for Wind Power," M.Sc. Thesis at NTNU, 2008.

[29] A. Gamboa, "Control of MMC in HVDC Applications," M.Sc. Thesis at Aalborg University, 2013.

[30] A. Isidori, L. Marconi, A. Serrani, "Robust Autonomous Guidance an Internal Model Approach," 2003, XVI, 229 p., Hardcover, ISBN: 978-1-85233-695-0

Appendices

Appendix A: MMC with PSPWM

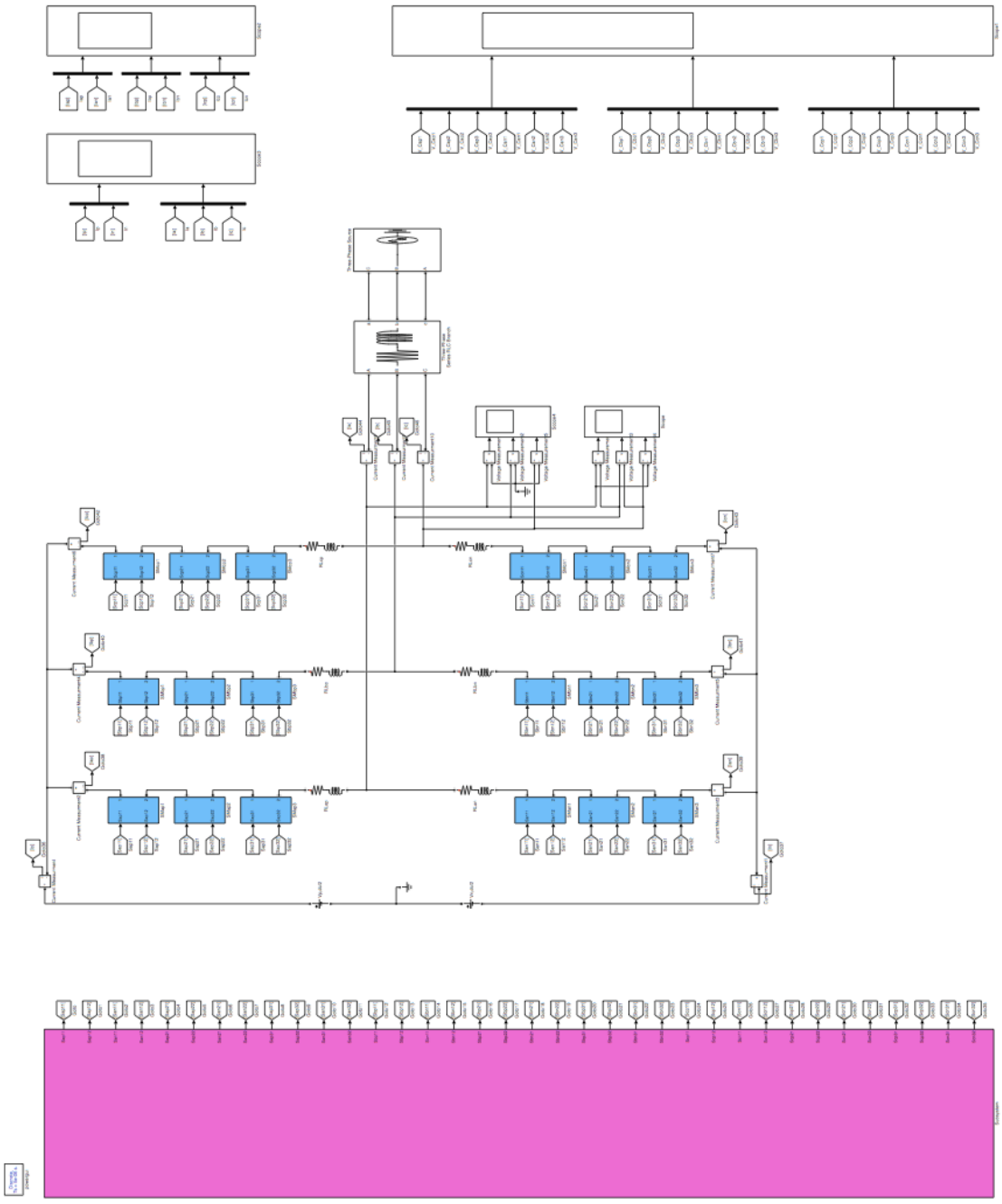

Fig. 1: Three-phase four level MMC

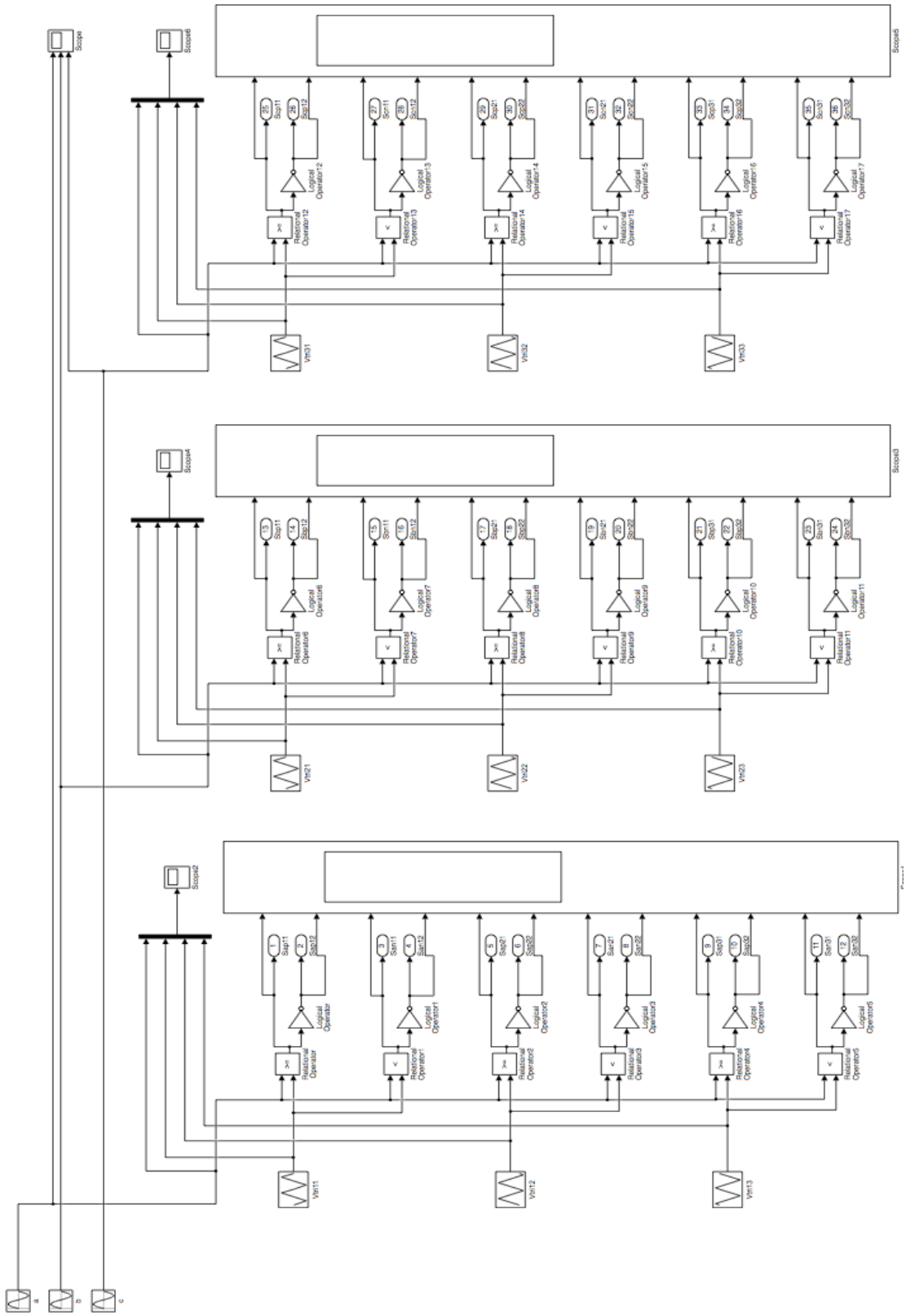

Fig. 2: PSPWM

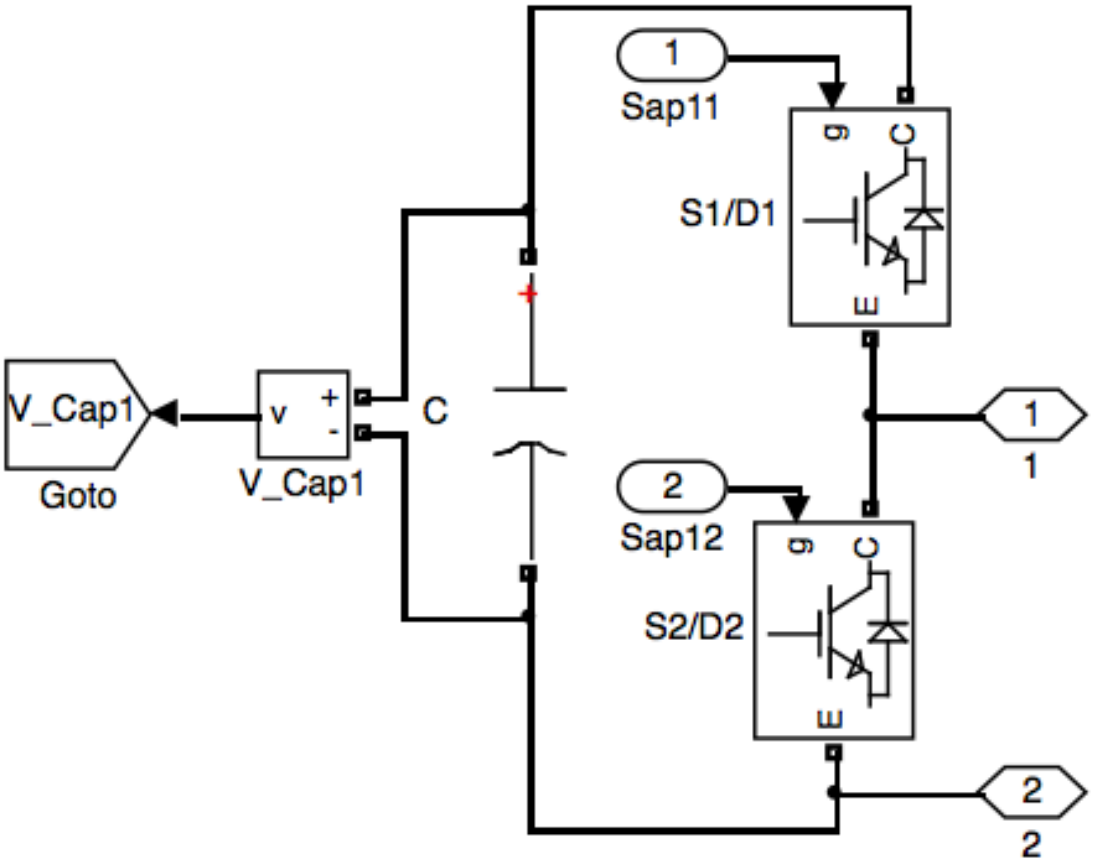

Fig. 3: SM